UNIVERSITY OF CALIFORNIA, SAN DIEGO

Arrays of Superconducting Quantum Interference Devices (SQUIDs) In Y-Ba-Cu-O Utilizing Ion Irradiation Patterning

A dissertation submitted in partial satisfaction of the requirements for the degree Doctor of Philosophy

in

Materials Science and Engineering

by

Travis Joseph Wong

Committee in charge:

Professor Robert Dynes, Chair
Professor Prabhakar R. Bandaru
Professor Eric Fullerton
Professor Brian Maple
Professor Vitali Nesterenko

2016

The Dissertation of Travis Joseph Wong is approved, and it is acceptable in quality and form for publication on microfilm and electronically:

_____

_____

_____

_____

_____
Chair

University of California, San Diego

2016

DEDICATION

Thank you to my lab for training me and giving me great opportunities, to my friends and family who have remained at my side through the worst, and to my late Mother and Father, both of whom gave me the courage and strength of character to be who I am today.

For the days when I was lost, the nights when I was cold, the overwhelming days when I lost hope, and for all the sacrifices and pain she endured, she remained constant for me, she was there, and that made all the difference. To Geetha

TABLE OF CONTENTS

LIST OF FIGURES

LIST OF TABLES

Acknowledgements

This thesis represents the collective effort of many people who have contributed to my work over the past 5 years. In particular I am grateful to the years of opportunities and guidance that Prof. Bob Dynes has given me. I have greatly benefitted from Bob's personal involvement in my thesis, especially in the realm of experimental detail and meticulous preparation in both life and work. It has been a distinct privilege to work with a person of such high caliber. I also acknowledge the mentoring and support of Prof. Shane Cybart, whose hands-on mentoring was vital to my success. Shane's dedication to pushing the standards always served as a great example and his insistence to perform the "quick-and-dirty" verification experiment before committing to a full effort especially rang home.

I acknowledge the amazing collaborative efforts of Dr. Ethan Cho and the many undergraduate researchers I have had to privilege to work with. Ethan's dedication and selflessness made many collaborations succeed even when no one else wanted to continue. The majority of this work was performed alongside Ethan, with significant contributions from Dr. Peter Roediger especially in the fabrication of trilayer masks.

Finally, I would like to thank my friends and family for their unconditional support during this thesis. My girlfriend Geetha deserves special recognition for enduring my weird hours, supporting me when I was lost, and sacrificing many personal ambitions on behalf of my professional aspirations. I also acknowledge my brother Casey, sister Rachael, and Grandmother Garth have remained at my side throughout my career, and have been a constant source of strength.

VITA

2008	Bachelor of Arts, Physics, with Honors, University of California, Berkeley
2009	Master of Science, Materials Science and Engineering, University of California, San Diego
2010-2011	Materials Scientist, Elintrix, Inc.
2011-2016	Doctor of Philosophy, University of California, San Diego

PUBLICATIONS

T. J. Wong, E. Y. Cho, S. A. Cybart, and R. C. Dynes. "**Mutual coupling effects in closepacked series-parallel SQUID arrays**" *Applied Physics Letters*, in preparation.

T. J. Wong, E. Y. Cho, S. A. Cybart, and R. C. Dynes. "**Performance of series SQUID arrays constructed from focused Helium ion beam Josephson junctions**" *Applied Physics Letters*, in preparation.

S. A. Cybart, E. Y. Cho, T. J. Wong, B. H. Wehlin, M. K. Ma, C. Huynh, and R. C. Dynes. "**Nano Josephson superconducting tunnel junctions in YBCO directly patterned with a focused Helium ion beam**" *Nature Nanotechnology*, **10**, pp. 598, April, 2015.

S. A. Cybart, E. Y. Cho, T. J. Wong, V. N. Glyantsev, J. U. Huh, C. S. Yung, B. H. Moeckly, J. W. Beeman, E. Ulin-Avila, S. M. Wu, and R. C. Dynes. "**Large voltage modulation in magnetic field sensors from two-dimensional arrays of Y-Ba-Cu-O nano Josephson junctions**" *Applied Physics Letters*, **104**, pp. 062601, February, 2014.

S. A. Cybart, P. Roediger, K. Chen, J. M. Parker, E. Y. Cho, T. J. Wong, and R. C. Dynes. "**Temporal stability of Y-Ba-Cu-O nano Josephson junctions from ion irradiation**" *IEEE Transactions on Applied Superconductivity*, **23**, pp. 1100103, June, 2013.

FIELDS OF STUDY

Major Field: Materials Science and Engineering

Studies in Solid State Physics
Professor Robert Dynes

Studies in Electronic and Photonic Properties of Materials
Professor Prabhakar Bandaru

Studies in Magnetic Materials: Principles and Applications
Professors Eric Fullerton and Sungho Jin

Studies in Nanomaterials and Properties
Professor Sungho Jin

Studies in Antennas and their System Applications
Professor Gabriel Rebeiz

Studies in Energy Materials and Applications
Professors Prabhakar Bandaru, George Tynan, and Sungho Jin

Studies in Thermodynamics
Professors Vitali Nesterenko, Jan Talbot, and Vlado Lubarda

Studies in Porous Silicon Photonic Chemical Sensors
Professor Michael Sailor

ABSTRACT OF THE DISSERTATION

Arrays of Superconducting Quantum Interference Devices (SQUIDs)

In Y-Ba-Cu-O Utilizing Ion Irradiation Patterning

By

Travis J. Wong

Doctor of Philosophy in Materials Science and Engineering

University of California, San Diego, 2016

Professor Robert C. Dynes, Chair

In recent years the demand for turnkey, easy to use superconducting sensors has created interest in Josephson junctions operating at temperatures far above the near zero temperatures required by the gold standard Nb-AlOx-Nb technology (<5 K). High temperature circuits are particularly favorable in applications such as biomagnetic clinical screening, as high circuit temperatures lower the cooling requirements and minimize the separation between the cold sensor and patient. One technology that fits the bill is the Superconducting Quantum Interference Device (SQUID) constructed from ion damage Josephson junctions in superconducting Y-Ba-Cu-O. SQUIDs are incredibly sensitive yet simple, thin film devices that are most often used as magnetic flux-to-voltage transducers for magnetometer applications. Ion damage junctions are

fabricated by selectively bombarding nanoscale regions of superconductor with energetic particles to introduce defects that controllably reduce the superconducting transition temperature. Ion damage Josephson junctions in superconducting Y-Ba-Cu-O are a strong candidate due to their high placement density (typically millions per square centimeter), intrinsically non-hysteretic current-voltage characteristics, and the advantage of no metallurgical interfaces.

In this thesis several different magnetometer architectures of Superconducting Quantum Interference Devices (SQUIDs) were characterized using two methods to construct the ion damage junctions: broad beam irradiation using ion masks and direct write irradiation with focused ion beams. Large-scale arrays of series-parallel SQUIDs behave as multislit interference gratings such that the device layout controls the degree of coherence and thus the device performance. We find that device performance is unaffected by neighboring SQUIDs within a series-parallel array until supercurrents from different devices begin to overlap in the shared electrodes. Parallel SQUIDs improve the robustness of the array performance in the presence of significant thermal fluctuations, junction parameter spread, and material imperfections. The importance of junction parameter spread was compared between a series array of novel three junction "BiSQUIDs" and standard two junction SQUIDs.

Overall we show that the highest voltage outputs and most uniform SQUID devices are constructed from ion damage Josephson junctions with the shortest junction length and in films thinner than the ion range.

1.Introduction

Background and Motivation

The discovery of the high temperature superconductors in 1986 inspired hope for an electronics revolution in much of the physics and engineering community. Low temperature superconducting (LTS) materials had been known for 75 years, with thin film circuits widely investigated for 30 years. Semiconductor integrated circuits had finally reached the personal computing level in the early 1980's after 40 years of concerted development with market projections growing as fast as computing hardware advancements [1]. Success in the semiconductor industry sparked many different research groups to investigate new architectures and materials to push the circuit performance that included superconducting circuits. Digital superconducting circuits are of interest due to their exceptionally low dissipation and the state switching energies are 1000x lower (Rapid Single Flux Quantum RSFQ ~10^{-18} J) than semiconductor Field Effect Transistors (FETs ~10^{-15} J) [2]. Integration density in semiconductors is limited by the cooling power available, hence lower energy dissipation enables higher integration density. Perhaps superconducting magnetometers are even more interesting than the digital circuits due to the variety of completely unique applications in biomagnetics and novel instrumentation [3]. However before 1986 few in the community had expectations of superconductors reaching critical temperatures (Tc) much above a "theoretical" limit of 30 K as predicted by the highly successful Bardeen-Cooper-Schrieffer (BCS) microscopic model

solved in 1957 [4]. Many in the community held that the difficult and expensive cooling techniques required to achieve these temperatures were the primary bottleneck to success in superconducting electronics [5]. The advent of high temperature superconducting (HTS) cuprate materials such as $YBa_2Cu_3O_{7-x}$ (YBCO "123" T_C= 92 K material) seemingly offered a new path to reach mass markets with the dramatically decreased cooling requirements [6].

As anyone can attest, 30 years later superconducting circuits have yet to reach mass markets. Progress in thin film deposition techniques to produce high quality materials on a variety of substrates has been enormous, in particular for cuprate materials such as YBCO [7]. Superconducting digital circuit architectures have matured to the point of the first functional quantum computers with 10's of bits (however operating below 1 K). Superconducting magnetometers have been successfully employed in many scientific instruments including magnetic materials characterization, clinical biomagnetics, nondestructive evaluation, and detectors for astronomical telescopes [3]. However, all of these applications are high cost in order to compensate for the low device yields, high input cost of engineering development, and the large run-to-run variation in growth and fabrication. In general the extreme chemical and physical complexity of the HTS materials have proven to be a significantly tougher impediment to widespread use than achieving a 4 K operating temperature. By far the most promising applications for HTS circuits are those that demand temperatures above 40K such as magnetometry of nearby room temperature objects [3].

A clear weakness of HTS materials lies in the intrinsic tendency for thin films to lose their superconducting properties through material disruptions on

atomic length scales. The ability to natively disrupt superconductivity on the atomic scale through disorder is convenient for tunneling. Typical quantum tunneling devices require at least two materials, one conductor and one insulator, with at least two atomic scale interfaces. Standard multilayer circuit design also requires serial growth and stacking of materials introducing interfaces between subsequent depositions. Technologically the difficulty in the realization of HTS electronics has been the lack of any highly scalable and robust processing techniques to produce clean atomic scale interfaces [8]. Disorder, contamination, nonepitaxial growth, process nonuniformity, and undesired deoxygenation are all contributing factors to unreliable interfaces. If localized disorder can be used to define a circuit element within an otherwise perfect thin film, then metallurgical interfaces would be avoided altogether. One of the most precise ways to locally induce disorder and drive Y-Ba-Cu-O from metal to insulator is to utilize energetic radiation to produce randomly distributed point defects. Technologically, tightly focused radiation sources such as electron beam and ion beam are commonly used in microscopy and lithography applications. Hence there is a clear opportunity to produce a highly scalable and reproducible tunneling barrier in HTS materials, if the technology was available to reproducibly induce disorder on the nanoscale.

In this thesis, thin films of HTS materials (YBCO 123) were bombarded with energetic ions to produce localized, nanoscale regions of disorder that behave as barriers for Josephson junctions (JJs). Due to the extreme sensitivity of the superconducting electronic state to disorder, regions of weakened superconductor can be produced from ion irradiations without the creation of material interfaces. When the length scale of a disordered region approaches

the nanoscale, weak Josephson coupling results through the "weak link" between undamaged superconductors. In particular, this thesis exploits two ion patterning techniques: high aspect ratio masking of broad-beam ion sources and focused ion beam sources. In both techniques the locality of the damage is a natural characteristic of a well-focused beam (electron lithography of implant mask or direct write ion beam). Ion damage Josephson junctions are inherently stable due to the lack of materials interfaces and can be patterned down to a length scale of a few atoms.

The engineering focus of this work is based on Superconducting Quantum Interference Devices (SQUIDs) constructed from ion damage Josephson junctions. SQUIDs are the exquisitely sensitive transducers of magnetic flux to voltage and operate from DC to many GHz (broad bandwidth). There is a need for SQUID detectors that operate significantly above 4 K for the detection of biomagnetic fields. There is a growing interest in the biomagnetic fields originating from the brain, heart, and liver in humans. In addition, SQUID detection of brain and heart signals of infants in utero are an active area of research to replace the existing invasive techniques [Tristan Tech]. Typical human anatomical magnetic field strengths are no larger than 1/1000 of Earth's field and are low frequency approaching DC [3]. These minute biomagnetic fields are primarily dipole in nature, and therefore the signal strength decreases as $\frac{1}{r^3}$ away from the source. There is a tradeoff between placing sensors as close as possible to the field source to maximize signals and thermally isolating detectors operating at very cold temperatures from test subjects. Historically, higher temperature SQUIDs have been constructed, however device performance has left much to be desired due to

significantly elevated noise levels coming from the materials in the devices. The signal-to-noise level limits the sensitivity and resolution of biomagnetic imaging applications. Hence devices with increased noise generally have lower spatial resolution. Hence there is a need to develop high performance SQUIDs for fundamental studies of human biomagnetism and for advancement of current clinical techniques.

SQUIDs are notoriously sensitive to environmental noise with microvolt level output signals and typically ~1 Ω source resistances. There is a need to develop SQUID instrumentation with high slew rates to operate in noisy environments, or at least reduce the shielding requirements of the sensor packaging. In general, increasing the SQUID transfer function (Volts/Tesla) and increasing the signal level (much larger than the typical preamplifier input noise) will increase the instrument slew rate and dynamic range [9]. Typical SQUIDs are intrinsically low noise devices, on the order of the Johnson noise of 1 Ω at the bath temperature. Even the best preamplifiers are typically noisier than SQUIDs, and are especially challenged at low frequencies due to 1/f noise. Generally preamplifiers will add the least amount of noise when 50-1000 Ohm sources are connected (the typical equivalent Johnson noise resistance of the preamp) [10]. In practice a cold transformer is used between the SQUID and the preamplifier to achieve operation limited by SQUID noise [3]. Higher resistance SQUID devices will enable lower noise operation without the need of bandwidth limiting cryogenic signal transformers.

One possible solution to improve SQUID performance in noisy environments is to use a series array of SQUIDs. The SQUID signal and source resistance scales with the number of SQUIDs in series. Furthermore, parallel

SQUID arrays have been shown to be more robust towards circuit parameter variations. There is also a general interest in the development of new SQUID architectures such as the BiSQUID (three junction, two loop SQUID). This thesis is a focused study on two different planar YBCO SQUID architectures constructed from ion damage Josephson junctions: series-parallel DC SQUID arrays, and series BiSQUID arrays.

Properties of Superconducting Thin FIlms

Kamerlingh Onnes observed in 1911 that below a critical temperature T_C, the electrical resistance of metals such as Hg, Sn, and Pb vanishes. The most sensitive example of this effect is demonstrated in supercurrents circulating in superconducting rings which have been observed to have zero measurable decrease. Estimates have suggested the current will persist for 10^{10} yrs.

In 1933 Meissner and Ochsenfeld observed that superconductors also exhibit perfect diamagnetism and more importantly complete magnetic flux expulsion from within a superconducting material. In other words, as a superconductor is cooled through T_C, any magnetic field that is initially normal to the material surface and penetrating the metal is completely expelled below T_C from the material interior. Magnetic flux expulsion distinguishes a superconductor from a perfect conductor, as perfect conductors would tend to trap magnetic fields in a closed geometry. Importantly, the flux expulsion is also reversible in that if a critical magnetic field H_C is exceeded, then the superconductor returns to the normal metallic state. If this magnetic field is

then subsequently reduced below H_C, then the superconducting state returns and magnetic flux is again expelled.

In general, as a superconductor is cooled further below T_C the critical magnetic field H_C increases indicating a more robust superconducting state at lower temperatures. When a current is passed through a superconductor, a self magnetic field is generated from the current. Hence it is possible to apply a high enough current through a superconductor to generate a magnetic field up to H_C at which point the superconducting state is destroyed. The current density required to destroy the superconducting state is called the critical current density J_C. Eddy currents formed on the surface of a superconductor to screen magnetic fields below H_C allow external fields to penetrate the surface for a finite length called the London magnetic penetration length λ_L. The superconducting penetration length generally decreases with decreasing temperature.

Conventional superconductors such as Pb, Nb, and Sn are well described by the microscopic theory of Bardeen-Copper-Schrieffer (BCS Theory). Most low temperature superconductors (LTS) are conventional superconducting materials. Just like in normal metals, superconductors conduct via almost-free electrons at the Fermi energy typically traveling at velocities near 10^8 cm/sec (100x slower than light). There is an attractive force between the negatively charged electrons and the positive ion cores of the crystal lattice. The ion cores respond to the electrons at their vibrational frequencies (phonon frequency) on the order of 10^{12} Hz; about a 1 picosecond time constant. In other words, a single ion core in the crystal lattice deforms or "vibrates" in response to electrons that fly past at high

velocity. In a 1 picosecond time frame, a ballistic electron will travel approximately 1 micron. Once the ion core has moved from its lattice site, electrons of the opposite momentum and spin to the original electron will be attracted to the ion core. The two electrons are effectively attracted to each other in a "Cooper Pair" over macroscopic distances on the order of microns and this length is defined as the superconducting coherence length ξ.

In superconductors the condensed electron pairs thus have an attractive potential on the order of 1 meV. This attraction results in the formation of an energy gap $\Delta \sim k_B T_C$ in Energy-Momentum characteristic at the Fermi energy. Once a superconductor has been cooled below its critical transition temperature, all the Cooper pairs in the material spontaneously "condense" into the bosonic superconducting ground state around the Fermi energy. These ground state pairs cannot be broken until the energy equaling the binding (2x energy gap) energy is reached. Once the gap energy has been exceeded, the Cooper pair is broken into "quasiparticles" which are the carriers of the excited states in superconductors. This binding via the electron phonon interaction was most convincingly confirmed experimentally by Rowell-McMillan in 1965 using Pb-PbOx-Pb tunnel junctions where they inverted the gap equation to obtain the phonon density of states and coupling constants from the electronic density of states [11].

In general the conventional superconducting energy gap is more or less isotropic in momentum space, increasing with decreasing temperature, and the gap magnitude can be used as the amplitude of the superconducting order parameter. In a conventional superconductor such as Sn or Pb there are on average 10^6 Cooper pairs within a volume bounded by

the coherence length of a single pair (Coherence volume). Hence the strength of the superconducting state is not based on microscopic single pairs, but on the macroscopic coherence of many overlapping pairs. It is the macroscopic phase locking in a superconductor that ensures a single energy gap in the energy-momentum dispersion.

The superconducting electronic state is a coherent quantum mechanical state and can be described by a complex wavefunction ψ. Ginzburg and Landau first introduced the ψ wavefunction in 1950 as an order parameter as defined in the framework of Landau's general theory of second-order phase transitions (GL theory). It has since been shown that the GL theory is a limiting form of the BCS microscopic theory and embodies in a simple way the macroscopic quantum mechanical nature of the superconducting state. Using GL theory it is simple to understand that the superconducting state has a position dependent amplitude $A(\vec{r})$ and a phase $\varphi(\vec{r})$:

$$\psi = A(\vec{r})e^{i\varphi(\vec{r})}$$

Superconducting electrodes exhibit global phase coherence on a macroscopic scale with wavepackets of superconducting charge carriers on the order of the coherence length ξ. The phase of the wavefunction cannot vary rapidly within a single coherence length ξ without increasing the energy of the state above the condensation energy.

There are two types of superconducting materials: Type I and Type II. The GL parameter κ is defined as the ratio of the penetration depth to the coherence length:

$$\kappa = \frac{\lambda}{\xi}$$

When $\kappa \ll 1$ a material is Type I, and a positive surface energy exists at the domain wall between the superconducting and normal regions of a material. This domain wall stabilizes the superconducting state from penetrating magnetic flux in length scales less than ξ. When $\kappa \gg 1$ a material is Type II, and a negative surface energy exists at the domain wall. Magnetic flux can enter Type II materials within ξ length scales and form Abriskov vortices. In other words, there are two critical fields in a Type II material: below the first critical field H_{C1} magnetic flux is completed excluded, above the second field $H_{C2} > H_{C1}$ the superconducting state is destroyed, and between the two fields a continuous increase in flux penetration in the form of quantized vortices (see following discussion) occurs scaling with the applied field. The flux within each Abriskov vortex is exactly equal to one flux quantum (h/2e), and the vortices order into a triangular lattice penetrating throughout the superconductor.

The high Tc superconducting materials studied in this thesis are all of the thin film and Type II material variety. Thin films of YBCO are epitaxially grown on lattice matched substrates, typically r-plane cut single crystal sapphire. When superconductors are patterned into planar thin films, currents in the material are only present on the edges of the film and not in the center. However, if a thin film thickness is equal to or less than the magnetic penetration length then the effective penetration length becomes very large and screening currents extend deeply into superconducting film. In general DC supercurrents (much less than J_C) in the presence of small magnetic fields (much less than H_C) follow the London electrodynamic equations

$$\Lambda \frac{\left(\partial \overrightarrow{J_S}\right)}{\partial t} = \vec{E}$$

$$\Lambda\left(\nabla \times \overrightarrow{J_S}\right) + \vec{B} = 0$$

$$\Lambda = \frac{m^*}{n_S^* e^{*2}} = \frac{\lambda_L^2}{\mu_0}$$

With the London Gauge commonly used for simply connected superconductors in static fields.

$$\Lambda \overrightarrow{J_S} = -\vec{A}$$

Here the m* denotes the effective mass of a pair (twice a single electron), n* the density of pairs, and e* the effective pair charge (twice single electron 2e). Subscript "S" is explicitly stated to imply supercurrents only. The first equation clearly states that for static supercurrents no electric fields are present internally. Magnetic fields clearly define the superconducting current density in the second equation. London's second equation can be rewritten without curl:

$$\hbar \nabla \varphi = e^* \Lambda \overrightarrow{J_S} + e^* \vec{A}$$

In this form, London's second equation clearly links the spatial dependence of the order parameter phase to the supercurrent density and applied magnetic field. The relation has important consequences for the movement of flux quanta into closed superconducting rings such as those used in Superconducting Quantum Interference Devices (SQUIDs). Suppose a hole is created within a superconductor effectively creating a superconducting ring. Circulating currents will flow on the surface of the ring to screen external magnetic fields. The phase of the order parameter is 2π periodic and must be unique at each point in space in the superconductor. Hence the wavefunction can experience phase jumps of 2π at any point

inside a superconductor and is a multiple valued scalar function. Generally the phase is assumed ad hoc to be $2\pi n$ step-wise discontinuous at specific cross sections leaving the majority of the superconductor single valued in phase. If the step-wise jumps were to be "peppered" throughout a superconductor as points, the phase gradient (like in the finite current case) will contain derivatives of the Dirac delta function (at each jump) which is unphysical. Hence all step-wise jumps in phase must lie on a surface geometry or "jump surfaces" rather than single points. A Josephson junction is considered to be the jump surface in an otherwise perfect superconducting electrode since it is the "weak link".

The magnetic field enclosed within superconducting rings is quantized as a result of the 2π periodic phase. Consider a path integral of the order parameter phase (London's second equation) taken around the hole of a superconducting ring, where the path is deep inside the superconductor so as to include magnetically induced currents ($\overrightarrow{J_S} = 0$):

$$\hbar \oint \nabla \varphi \cdot \overrightarrow{dl} = e^* \oint (\Lambda \overrightarrow{J_S} + \vec{A}) \cdot \overrightarrow{dl} = e^* \oint \vec{A} \cdot \overrightarrow{dl} = e^* \int_S (\nabla \times \vec{A}) dS = e^* \int_S \vec{B} \cdot \overrightarrow{dS}$$

by the use of Stokes theorem in the third equality. Then:

$$\hbar \oint \nabla \varphi \cdot \overrightarrow{dl} = e^* \int_S \vec{B} \cdot \overrightarrow{dS} = e^* \Phi_0$$

Additionally, due to phase coherence of the order parameter around the hole the left side of the equality is simply equal to $\hbar(n2\pi) = hn$ where n is an integer. Hence we have a condition of flux quantization around any normal hole penetrating a superconductor or for magnetic flux threading a superconducting ring:

$$\Phi_0 = \frac{nh}{e^*} = 2.067 * 10^{-15}\ Wb = 2.067\ V * sec$$

where n= 0,1,2,3,…. In general all closed paths within a multiply connected superconductor must pass through at least one jump surface. Additionally, each closed path or superconducting loop must have at least one jump surface with its own quantization number "n". In the case of two loops sharing a common electrode (such as series-parallel SQUID arrays), each loop must have its own quantization number and at least one jump surface to the "outside" of the superconducting loop. In other words, it is unphysical to define a closed circulating path of superconducting material with only internal jump surfaces i.e. the flux must enter and exit the loop.

Flux quantization in superconductors is one of the most profound concepts of both the macroscopic phase coherence of the order parameter and of the effective charge of the carriers (equaling twice a single electron). Direct measurements of the flux trapped in each normal vortex in the Abrikosov vortex lattice confirm the two electron pairing nature of the superconducting carriers in unconventional superconductors. Superconducting quantum interference devices (SQUIDs) are devices that take advantage of this flux quantization to produce the most sensitive detectors of magnetic flux known. The units of the last equality on the right are suggestive that flux quanta are related to voltage peaks on picosecond time scales (more in the following sections).

Superconducting Properties of Cuprate Materials

Many materials that can be grown in thin film form with a high uniformity and crystallinity can be processed using standard planar

semiconductor processing techniques. The most desirable materials systems are those that can be deposited at moderately low temperature, are chemically stable, and can be deposited on many different substrates while maintaining their useful properties. For superconducting thin films, high quality is often associated with a high transition temperature, low normal-state resistivity, high critical current density, and polycrystalline films that are strongly aligned to the orientation of the (presumably single-crystal) substrate. The thin film materials investigated in this thesis were grown with the highest quality that can be commercially obtained.

The material of choice in this thesis was discovered in 1987 by Wu et. al.: YBa2Cu3O7-x with a T_C = 92K. At that time YBCO123 was the only known material to superconduct above the boiling point of liquid nitrogen (77 K) and so after its discovery it was heavily researched. Since then many rare earth compounds have been found in the cuprate $RBa_2Cu_3O_{7-x}$ family: Y, Nd, Sm, Gd, Dy, Ho, Er, Tm, Yb, and Lu.

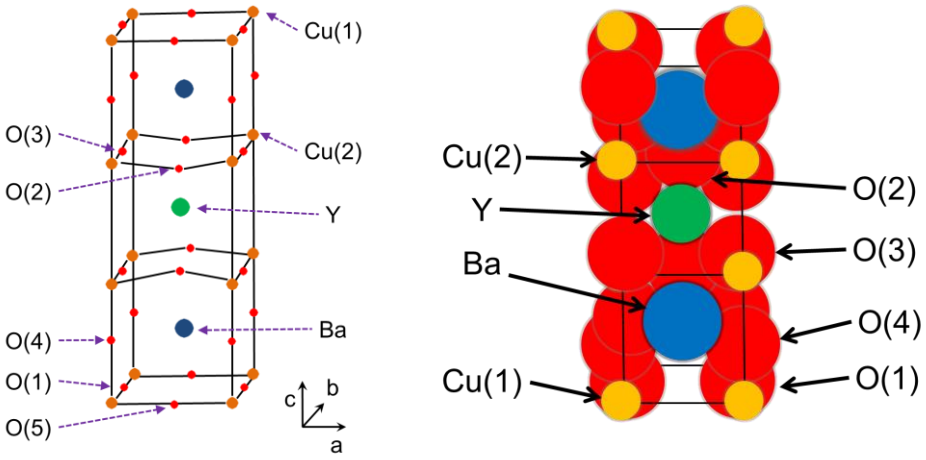

Figure 1: (Left) $YBa_2Cu_3O_7$ unit cell showing all possible oxygen sites. Superconducting YBCO typically has vacancies in O(1) sites. (right) Ionic Radii of atoms in YBCO unit cell, the oxygen sites are noticeably more active.

Cuprate materials are perovskite structures with either orthorhombic (x=0) or tetragonal (x=1) symmetry, with tetragonal crystals generally insulating and orthorhombic crystals exhibiting superconducting properties. Tetragonal crystals have vacant O(5) and O(1) "chain oxygen" sites, which are believed to function as charge reservoirs. The O(3) and O(2) sites are referred to as the oxygen plane sites. Oxygen can be "loaded" into the structure via oxygen annealing of cuprate materials at elevated temperatures. The complex $RBa_2Cu_3O_{7-x}$ cuprate crystal is most easily understood as approximately 3 stacked cells of a Barium Titanate crystal structure (Perovskite).

Conduction in the cuprate crystal is anisotropic and typically 10x higher in the a-b planes compared to the c-axis. Typical superconducting coherence lengths in optimally oxygenated $YBa_2Cu_3O_7$ are 2 nm (5 unit cells) in the a-b plane and 0.4 nm (1/3 unit cell) in the c-axis. As the YBCO oxygen content is decreased, the superconducting Tc lowers until x~0.5 where the material transitions from a superconductor to an insulating antiferromagnet. Coherence lengths this short typically only contain a few electron pairs (less than one pair per unit cell), and make defining macroscopic phase coherence nearly unphysical. Since the coherence lengths are on the order of the unit cell, a single atomic site displacement is sufficient to locally depress the superconducting order parameter. Unconventional superconductors thus are delicately sensitive to any stoichiometric variations and disorder, particularly in to O(1) sites. Annealing of point vacancies created by medium energy (<60 keV) electron damage is possible even at room temperature further demonstrating that very low displacement energies configurations exist within YBCO[5]. Even high quality YBCO materials typically have a "high"

density of oxygen vacancies that are nearly randomly distributed within crystallites and congregated near grain boundaries. Even high quality films typically contain a few percent variation in stoichiometry. Thus the electrical properties of YBCO will be directly affected by structural changes, where film uniformity must be considered down to atomic length scales.

Unlike conventional metal superconductors, measurements indicate the cuprate Fermi energy (E_F ~ 0.1 eV instead of 5-10 eV) is very close to the superconducting gap energy (Δ~20 meV). Therefore a large fraction of the cuprate charge carriers engage in pairing below T_C. At optimal oxygen doping the cuprate resistivity is metallic in both the a-b and c axes. When oxygen is "unloaded" from a cuprate superconductor the T_C drops and the resistivity rapidly becomes insulating at low temperatures. The Superconductor-Insulator transition occurs when the residual resistance per square is on the order of the quantum of resistance ($R_Q = \frac{h}{e^{*2}} \sim 6.5\ k\Omega$ in superconductors). An analogy between oxygen "loading" in cuprates and "doping" in semiconductors exists, where metallic conductivity behavior occurs in cuprates with high oxygenation (aka higher carrier density).

Josephson Junction Phenomena

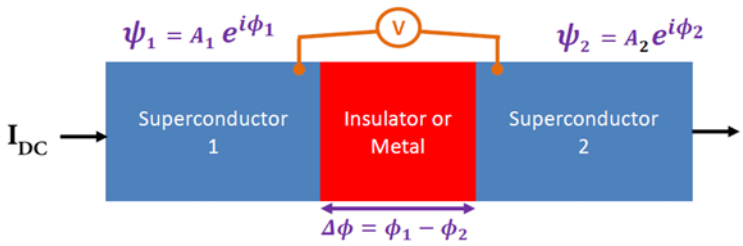

Figure 2: Basic geometry of a Josephson Junction where the phase slip $\Delta\phi$ between the superconducting banks occurs within the barrier region (not drawn to scale)

One of the most interesting manifestations of quantum mechanical effects in solids occurs when two superconducting materials are connected via a metallic or insulating link. A zero voltage supercurrent will pass through the "normal metal" or insulating barrier if the link is made sufficiently short. Typically an insulating barrier is on the order of 1 nm thick and a metallic barrier is on the order of 10 nm in order to allow for sufficiently strong coupling between the superconducting order parameters in the two electrodes. The maximum supercurrent that the junction can sustain before "going normal" is called the Josephson critical current. Josephson critical currents are typically on the order of 1 uA to 10 mA. Supercurrents through the Josephson junction are carried by Cooper pairs that quantum mechanically tunnel through the link. This effect was predicted by Josephson in 1962. Josephson's great intuitive insight was that the Cooper pair behaves as a single particle tunneling across a potential barrier (10^{-10} probability) rather than 2 independent electrons ($10^{-10}*10^{-10}$ probability). As the Cooper pairs tunnel through the junction, a "slip" in the superconducting phase difference between the two superconductors occurs inside the barrier that slides further with increased current bias. Hence Josephson junctions act as "phase slip centers" or "jump surfaces" between the two superconducting electrodes. There are two Josephson equations that describe this effect, the first Josephson equation describes the static behavior and relates the dc supercurrent to the static phase difference $\Delta\phi$:

$$I_{BIAS}(t) = I_C \sin(\Delta\phi(t))$$

As the bias current through the Josephson junction is increased above the junction's I_C a voltage appears, and the phase of the order parameter

takes on an alternating character with a distinct frequency for each voltage as described by the "dynamic" or AC Josephson Equation:

$$\frac{d\Delta\phi(t)}{dt} = \frac{2eV(t)}{\hbar} = \frac{2\pi V(t)}{\Phi_0}$$

The phase difference across a Josephson junction continually evolves when biased above I_C. A Josephson binding energy can be defined $E_J = \frac{\hbar I_C}{2e}$ and is the magnitude of the energy stored within the junction by the order parameter coupling between the superconducting banks. Once the Josephson binding energy is exceeded the phase "slips" within the barrier creating a finite voltage. The second Josephson equation states that the average rate of the phase oscillations within the barrier is proportional to the voltage across the junction.

The second Josephson equation is an exact relation between frequency and voltage. When a Josephson junction is biased with a high frequency current, the oscillations will phase lock to the high frequency bias producing exact voltage steps over current ranges comparable to the junction critical current. Due to the extremely precise nature of frequency measurements, the Josephson effect is now routinely used to calibrate the voltage standard. The Josephson constant is one of the most precise observed physical quantities known:

$$K_J = \frac{2e}{h} = 4.835979\,\frac{GHz}{10\ \mu V}$$

Josephson effects are quite general to any weak link between superconductors, and have been observed in junctions containing tunnel barriers, normal metals, weakened superconductors, and narrow constrictions.

RCSJ Circuit Model of Josephson Junctions

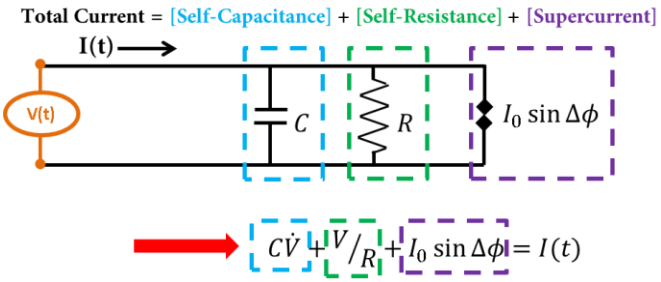

Figure 3: Resistively-Capacitively-Shunted Junction (RCSJ) effective circuit model for Josephson Junctions

Josephson junction (JJ) circuit elements are accurately modeled as a resistor, capacitor, and a Josephson supercurrent in a parallel circuit. This equivalent circuit is known as the Resistively-Capacitively-Shunted Junction (RCSJ) model first computed independently by Stewart [12] and McCumber [13]. In general a JJ can be accurately described by 3 circuit parameters: Josephson critical current (I_C), normal state Resistance (R_N), and junction capacitance (C). Superconducting circuits are typically current biased, and describing the currents of all three elements yields

$$I(t) = \frac{V(t)}{R_N} + C\frac{\partial V(t)}{\partial t} + I_C \sin\varphi(t)$$

The first term on the right describes the quasiparticle currents, the second term the effective capacitance between the electrodes, and the third term is the first Josephson equation. To solve the differential equation we substitute all voltage variables for junction phase using the second Josephson relation:

$$I(t) = \frac{\hbar C}{2e}\frac{\partial^2\varphi(t)}{\partial t^2} + \frac{\hbar}{2eR_N}\frac{\partial\varphi(t)}{\partial t} + I_C \sin\varphi(t)$$

Normalizing the bias current by I_C and introducing a normalized time variable, a nice simplification is possible:

$$\tau = I_C R_N \frac{2e}{\hbar}\ t = \omega_J R_N C$$

$$\frac{I}{I_C} = \beta_C \frac{\partial^2 \varphi}{\partial \tau^2} + \frac{\partial \varphi}{\partial \tau} + \sin\varphi$$

Where ω_J is the Josephson plasma frequency and β_C is known as the Stewart-McCumber damping parameter

$$\beta_C = I_C R_N^2 C \frac{2e}{\hbar} = \omega_J R_N C$$

In general, a Josephson junction I-V characteristic will be hysteretic for weak damping and large β_C. Multilayer tunnel junctions with insulating barriers and a large capacitance are commonly hysteretic in the I-V characteristics and intrinsically underdamped ($\beta_C \gg 1$). Practical devices add a resistor in parallel to each junction to effectively decrease R_N, increase the damping and remove the hysteresis. The coplanar junctions investigated within this work are strongly over-damped ($\beta_C \ll 1$) and non-hysteretic due to both an intrinsically small junction capacitance in addition to the intrinsic low resistance internal shunts within the junction barrier. Strongly overdamped junctions with a $\beta_C \ll 1$ are referred to as resistively shunted junctions (RSJ), effectively minimizing the contribution from the capacitance term in the differential equation

$$\frac{I}{I_C} = \frac{\partial \varphi}{\partial \tau} + \sin\varphi$$

The RSJ model is then more simply rewritten

$$\frac{\partial \varphi}{\partial t} = \frac{2e}{\hbar}\ I_C R_N\ \left[\frac{I}{I_C} - \sin\varphi\right]$$

Now the equation closely resembles the second Josephson relation with the term in square brackets defining the voltage as a function of bias. The voltage term $I_C R_N$ is the figure of merit for Josephson junctions and sets the

scaling for the Josephson binding energy ($\hbar\omega_J = I_C R_N * 2e$). For $I > I_C$ a voltage is developed across the junction, which drives an oscillating current. As the current I is increased, the frequency increases ($\frac{\partial\varphi}{\partial t}$) demonstrating how the junction phase is "cranked" faster with increased current bias. For very high current bias ($\frac{I}{I_C} \gg 1$), the junction voltage asymptotically approaches the voltage expected for a classical resistor of magnitude R_N (Ohms law).

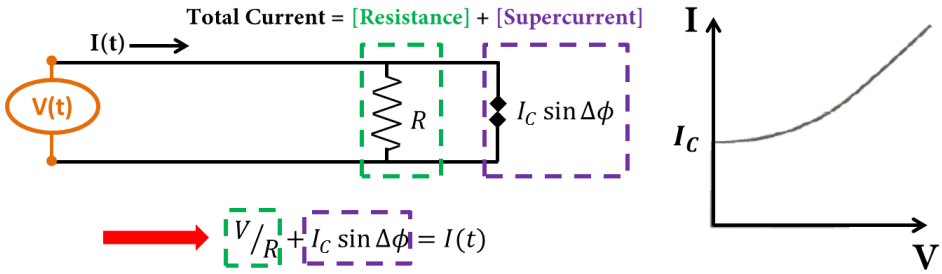

Figure 4: (left) Resistively-Shunted Junction (RSJ) effective circuit model. (right) IV characteristic of the RSJ model

Unlike the RCSJ model, the RSJ model has an exact analytical solution

$$V = 0 \qquad \text{for} \quad I < I_C$$

$$V = I_C R_N \sqrt{\left(\frac{I}{I_C}\right)^2 - 1} \qquad \text{for} \quad I \geq I_C$$

Just above the junction critical current, the Josephson IV characteristic is very nonlinear with a large dynamic resistance. Hence for small changes in current, a large voltage develops across the junction.

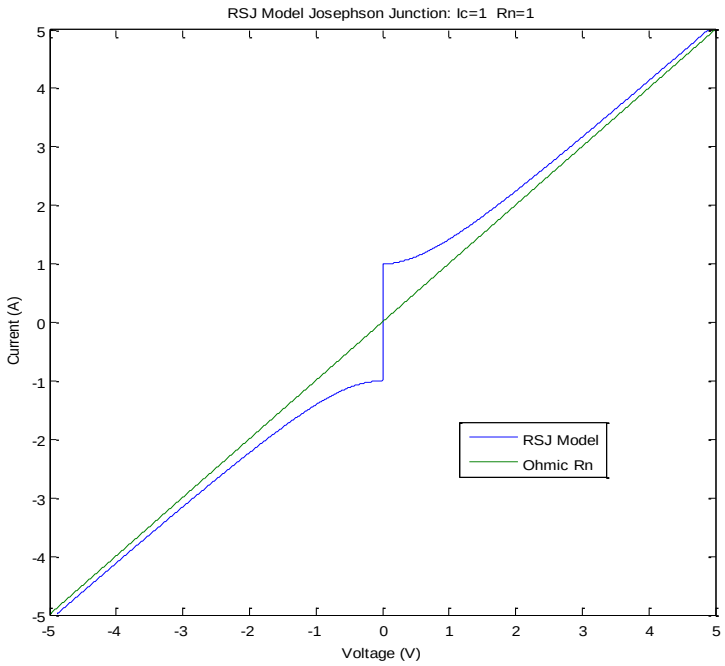

Figure 5: Numerical calculation of the junction IV characteristic using the ideal RSJ model.

The solution to the RSJ differential equation is a series of pulses in time, which when integrated produce an average voltage as a function of bias current (Figure Above). Taking the time average of these pulses generates the dc junction voltage at a particular current bias. The pulses have a peak-to-peak voltage of $(2I_C R_N)$, a DC offset corresponding to the current bias, and a time integral over one Josephson period exactly equal to one flux quantum

$$\int V\, dt = \frac{h}{2e} = \Phi_0$$

In other words, exactly one flux quantum passes through junction for each voltage oscillation.

Effect of Magnetic Field in Josephson Junctions

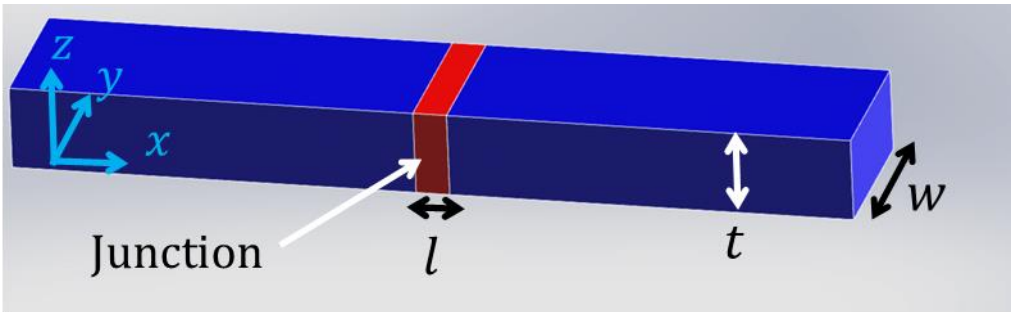

Figure 6: Basic construction of in-line, planar Josephson junction with current in the x-direction. YBCO materials in this work are oriented with the c-axis parallel to the z-axis, and therefore the a-b plane coplanar with the x-y plane.

There is a standard nomenclature in the description of planar Josephson junction size. Junction length '*l*' is parallel to the current direction and is a measure of the barrier thickness (x-axis). Junction width '*w*' is perpendicular to the current direction but in plane with the substrate (y-axis). And junction thickness '*t*' is perpendicular to both the current and normal to the substrate (z-axis).

The effect of external magnetic field is often small for Nb-AlOx-Nb trilayer Josephson junctions in LTS SQUIDs since the junctions are out-of-plane and perpendicular to the applied field. However, for all planar junction technologies such as ion damage Josephson Junctions magnetic fields have a significant effect on SQUID performance. In general the phase of the order parameter can differ between any two spatial points within the Josephson barrier. The first Josephson equation can be written to incorporate the phase difference between the electrodes as a function of spatial coordinates in the plane:

$$J(x,y) = J_c(x,y)\,sin\left(\varphi(x,y)\right)$$

Now consider a planar Josephson junction placed in the middle of a magnetically thick ($width * thickness > \lambda_L^2$) superconducting wire. Intuitively this is a similar situation to the superconductor-normal interface, but with a second interface in very close proximity. There are two limits to consider: wide bridges and narrow bridges. In a narrow or "short" junction, the currents initially on the edge of the electrodes will redistribute throughout the junction barrier (see Below Figure B). For a "wide" junction, the currents will not redistribute completely to the center of the electrode and will only "circulate" on a length scale called the Josephson penetration depth λ_J (see Below Figure A). The magnetic field is diamagnetically screened from the interior of wide junctions. Since the currents are confined to the edges of the junction, increasing the width of a "wide" junction will not increase the critical current further.

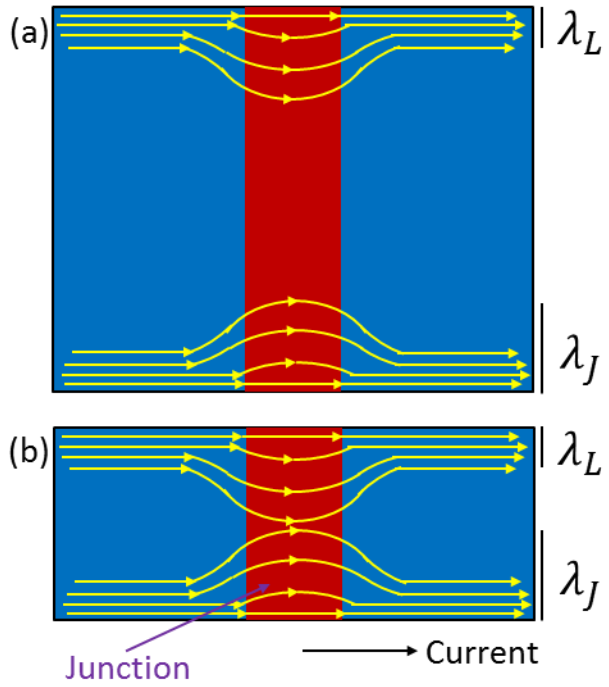

Figure 7: Top down view of the current distribution through a "wide" junction (A) and a "short" junction (B).

The Josephson penetration length is a much more general concept easily understood as the penetration length of a weakened superconductor (junction region). Josephson junctions effectively behave as type II superconductors where the Josephson penetration length is much longer than the superconducting coherence length within the junction. In the presence of an external magnetic field perpendicular to the plane (z-axis oriented) the junction will screen the magnetic field with a circulating current around the barrier region called a Josephson vortex. These Meissner circulating currents through the junction are spatially anisotropic and enlongated in the direction parallel to the barrier. These screening currents superimpose a non-uniform spatial current density J(x,y) onto the bias current passing through the Josephson junction. The penetration length of these currents into the bulk electrodes is called the Josephson penetration length λ_J (see Figure below). The energy stored in a Josephson vortex is equal to $E_J = \left(\frac{1}{\pi}\right)\Phi_0(4\lambda_J J_C)$, where the vortex is centered at the point of lowest potential energy i.e. the point of smallest Jc in the junction barrier.

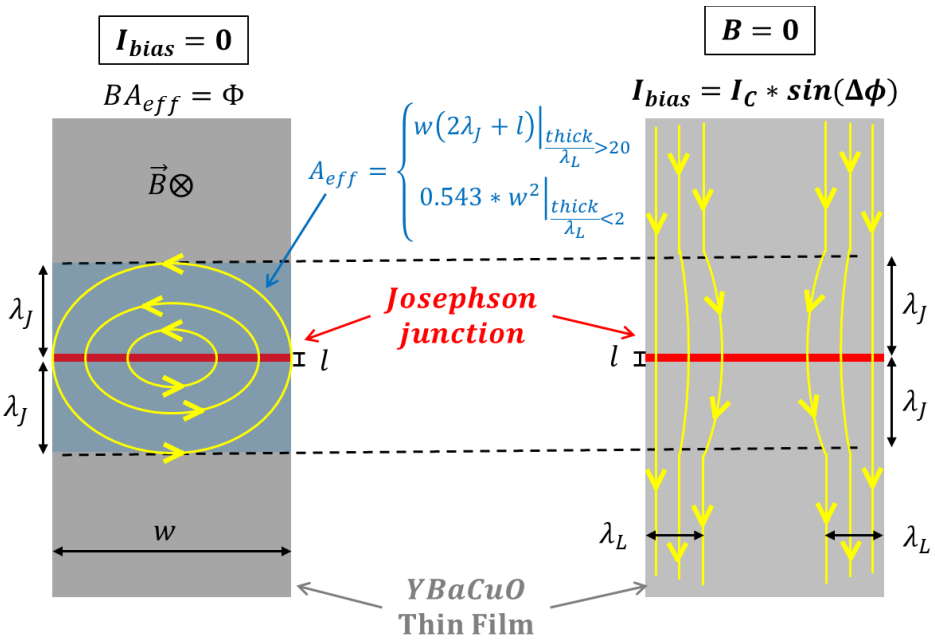

Figure 8: Sketch of the spatial currents for a short junction with applied field only (left) and with applied current only (right).

Without proof, the Josephson penetration depth for planar junctions [14]:

$$\lambda_J = \sqrt{\left(\frac{\Phi_0 w}{4\pi^2 \mu_0 J_C \lambda_L^2}\right)}$$

The Josephson penetration length is dependent on the critical current, junction geometry, and the London penetration length of the surrounding electrodes. In general λ_J is large relative to the bulk λ_L, hence magnetically the barrier behaves like a Type II superconductor even in a Type I material systems. In magnetically thin materials the film thickness less than the magnetic penetration depth, resulting in screening currents penetrating all parts of the junction and the electrodes [15]. A planar Josephson junction will behave like a magnetically thin superconductor, thus the Josephson penetration length for planar junctions can be much longer than out-of-plane junctions (see Figure above).

The zero field critical current is the largest supercurrent the junction will carry. As a magnetic field is increased from zero the critical current initially decreases until a minimum is reached when the flux through the area encompassed by the Josephson penetration length and the bridge width is equal to the flux quantum. The magnetic field required to minimize the Josephson critical current is known as the junction field period. With higher magnetic fields the critical current modulates with the same period but with decreasing maximum currents less than the zero field maximum.

This effect is due to magnetically generated interference of the spatially dependent phase within the Josephson junction. Josephson magnetic interference patterns are analogous to the Fraunhofer diffraction patterns observed from single slits in optics with interference occurring in the phase of the superconducting wavefunction. In direct analog to optics, the Fourier transform of the Josephson current density through the single "Josephson slit" will result in a periodic critical current as a function of magnetic field. For uniform currents flowing through the junction at all points along the barrier, the transform of the current density is simply a "Sinc" function. Junction magnetic interference patterns are generated independent of the detailed nature of the Josephson coupling. Additionally, a zero voltage current is not proof of pair tunneling across a barrier as a superconducting short has the same properties. However the variation of the maximum zero-voltage current with applied magnetic is conclusive of pair tunneling effects if the period is equal to $\frac{h}{2e}$.

In practice, the observed magnetic interference within a junction is dependent on the uniformity of the barrier. Only highly uniform barriers with

sinusoidal Josephson phase relations will have complete critical current modulation to zero with a regular Sinc periodicity. As field is increased each period of the interference pattern is the result of adding an additional magnetic flux quantum to the barrier, where each flux quantum creates an additional Josephson vortex in the barrier region.

The previous discussion of junction magnetic interference ignored magnetic fields generated from the Josephson currents themselves or "self-field" effects. Symptoms of self-field effects include the lack of zero current minima in the Fraunhofer pattern and when the zero field supercurrent saturates despite increased junction conduction width. Junctions that are wider than the twice the Josephson penetration depth are called "long" junctions and demonstrate self-field effects due to the nonuniformity of the currents flowing through the barrier. The diamagnetic region in the center of the junction will have a net current flow from the magnetic fields generated by the edge currents. In effect, the presence of a self-field enables multiple current state solutions to a single junction phase. In other words the currents in each Josephson vortex trapped within the barrier are skewed by the self-fields resulting in a non-integral number of Josephson vortices. Any junction with a nonintegral number of vortices will have a finite critical current, and hence the Fraunhofer pattern of long junctions will not have zero current minima until higher magnetic fields are applied. Additionally, since many solutions to a single junction phase are possible the long junction Fraunhofer pattern is "tilted" or asymmetric with magnetic field since multiple solutions exist to maximize the current for fields up to a few flux quanta [16].

It is worth noting that the intrinsic order parameter phase in unconventional superconductors is not isotropic. For instance in d-wave superconductors there is a "built-in" inversion of the intrinsic order parameter phase upon every 90 degree rotation of the current within a single crystal [17]. In general there may be a nonzero phase difference in the YBCO order parameter between two points which will manifest as a magnetic field dependent phase in the Josephson junction Fraunhofer pattern.

Thermal Fluctuations in Josephson Junctions

At finite temperatures (T>0) thermal fluctuations will be present throughout a superconducting material. In the presence of random thermal noise, the zero field critical current will fluctuate about a mean value with fluctuation magnitudes equal at all frequencies. This current noise originates in the shunt resistors *R* throughout the superconducting circuit and assumes the classical Nyquist-Johnson noise form:

$$S_{current}(f) = \frac{4k_B T}{R}$$

Where S_I is the current noise spectral density ($\frac{A}{\sqrt{Hz}}$) and is the same at all frequencies (white noise). In the framework of the RCSJ model, this white noise current can be superimposed using the Langevin approach:

$$\frac{\hbar C}{2e}\ddot{\varphi} + \frac{\hbar}{2eR}\dot{\varphi} + I_C sin\varphi = I_{Bias} + I_{Noise}(t)$$

Noise currents are assumed to be normally distributed with the mean defined as $\langle I_{Noise}(t+\tau) I_{Noise}(t)\rangle = \frac{2T_N \delta(\tau)}{R_N}$ where $\delta(\tau)$ is the delta function, T_N the noise temperature, and R_N the normal state shunt resistance.

The presence of current fluctuations intuitively results in a "smearing" of the dc IV characteristics. When thermal fluctuation currents are in the opposite direction to the bias current the zero voltage critical current increases on average. However this current increase is dominated by thermal fluctuations in the same direction as the bias current in the sense that an "early voltage" appears. The noise current adds to the bias current resulting in a net current large enough to enter the voltage state. In general thermal fluctuations are proportional to temperature and tend to "round" the RSJ IV characteristic near Ic into a fundamentally different shape [18].

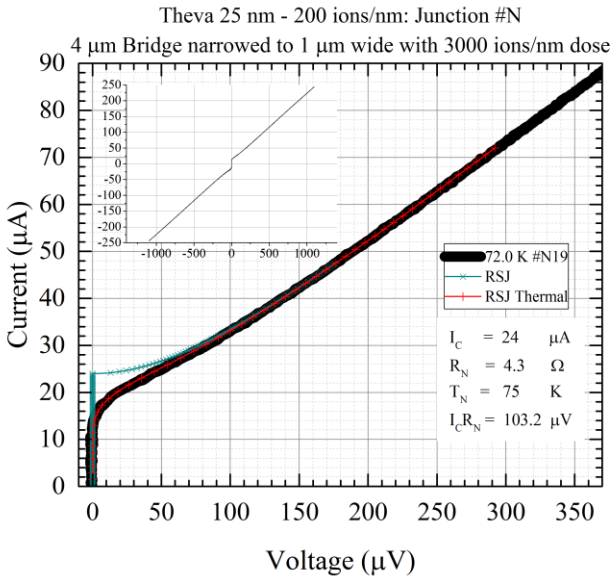

Figure 9: Current-Voltage characteristic of a single junction in the presence of thermal fluctuations. Sample fabricated using focused Helium ion damage courtesy of E. Cho [19].

Ambegaokar and Halperin quantified the effect of thermal fluctuations through the noise parameter γ [18]:

$$\gamma = \frac{I_C \hbar}{e^* k_B T_N} = \frac{E_J}{k_B T_N} = \frac{I_C}{I_{thermal}}$$

Where $E_J = \frac{I_C \Phi_0}{2\pi} = I_C R_N * 2e$ is the Josephson binding energy and $I_{thermal} = \frac{2\pi}{\Phi_0} k_B T_N$ is the magnitude of the thermal noise current. The perfect RSJ IV characteristic occurs as γ approaches infinity (i.e. $E_J \gg k_B T_N$). Clearly thermal effects can destabilize Josephson coupling if temperature is large enough or the Josephson critical current is small enough ($\gamma \leq 1$). In the case of LTS materials operating at 4 K, $I_{thermal} = 176\ nA$ compared to HTS materials operating at 77 K where $I_{thermal} = 3.23\ \mu A$. Practical device design requires the Josephson critical current to be much larger than the thermal current at operating temperature. For any room temperature Josephson junction to function (if such a material can be found), both junction and crystallite intergrain I_C must be much larger than $I_{thermal} = 12.6\ \mu A$.

A useful mechanical analog exists to qualitatively understand thermal effects in Josephson junctions and is known as the "washboard" model. Rearranging the RCSJ differential equation we can define a "tilted washboard potential" U_J:

$$\left(\frac{\Phi_0}{2\pi}\right) C\,\ddot{\varphi} + \frac{\Phi_0}{2\pi}\frac{1}{R}\dot{\varphi} = I_{Bias} - I_C sin\varphi = -\frac{2\pi}{\Phi_0}\frac{\partial U_J}{\partial \varphi}$$

$$U_J = \frac{\Phi_0}{2\pi}\{I_C(1 - cos\varphi) - I_{Bias}\varphi\} = E_J\{1 - cos\varphi - i\varphi\}$$

Using the washboard potential, the capacitive and resistive terms of the RCSJ model become analogous to the motion of a particle with mass $(\frac{\Phi_0}{2\pi} C)$ and friction coefficient $(\frac{\Phi_0}{2\pi}\frac{1}{R})$ rolling on a washboard. The applied bias current is analogous to the external force on the particle, where increasing the bias current increases the washboard tilt. At zero current bias the washboard is horizontal with the depth of the washboard corrugations or "wells" representing the strength of the quantum-tunneling barrier (well depth equal

to E_J). The horizontal position of the particle is analogous to the junction phase. As the bias current is slowly increased from zero the washboard is tilted and the particle remains confined within a single potential well oscillating at the Josephson plasma frequency.

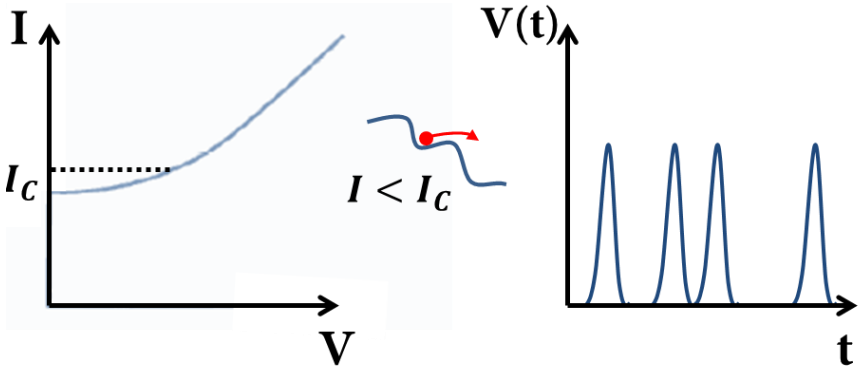

Figure 10: (left) Thermally rounded RSJ characteristics. (middle) Thermal fluctuations of sufficient magnitude can induce an "early voltage" by "activating" the particle over the top of the barrier for bias currents just under I_C. (right) Each time a particle rolls over the top of the barrier a voltage spike is produced. The time average of these voltage spikes results in the DC Current-Voltage characteristic with thermal rounding for current bias near I_C

When the bias current exceeds the critical current, the washboard is tilted far enough to allow the particle to roll over the top of the well. The critical current corresponds to the tilt where the slope is zero or negative everywhere on the washboard. The particle will continue to roll down the washboard at a rate proportional to the tilt (current bias) and the dissipation (Rn). Each time the particle rolls over a well, the time average phase position changes by exactly the distance between wells. Hence each time the particle escapes a well a spike in time averaged phase occurs on the time scale of the particle oscillation frequency (Josephson frequency proportional to I_CR_N). Each spike in time averaged phase will be the same across the washboard. Hence voltage spikes of equal magnitude and duration occur for each time the particle rolls over a well. The time average of these voltage spikes is equal to

the voltage observed in the Josephson IV characteristic at a particular current bias. Voltage spikes are spaced farther apart at low current bias and very close at high currents. For current bias much larger than the critical current the particle is virtually free rolling and rolls at a terminal velocity defined by the friction coefficient (proportional to $1/R_N$). The Stewart-McCumber parameter β_c corresponds to the damping of the particle motion in subsequent wells after each well jump. In the strongly overdamped limit ($\beta_c \ll 1$), the particle has small inertia and is immediately trapped at the bottom of a subsequent well if the tilt is reduced below I_C. In the strongly underdamped limit ($\beta_c \gg 1$) the particle has a large inertia and will continue rolling for many wells as the tilt is reduced even below the initial I_C. Underdamped particles with high inertia are both hard to start and hard to stop, hence the IV characteristic is hysteretic.

In the presence of thermal fluctuations the particle oscillations inside a particular well are larger with an amplitude equal to the thermal energy. For sufficiently deep corrugations and small thermal fluctuations, the particle oscillates back and forth in the well and cannot escape the well and the junction remains in the zero voltage state (time averaged phase is zero). However, in the presence of larger fluctuations the particle can escape the well at much lower tilt. Hence strong thermal fluctuations will cause the ball to continuously roll down the washboard thereby "washing" out the junction critical current.

RSCJ SQUID Model

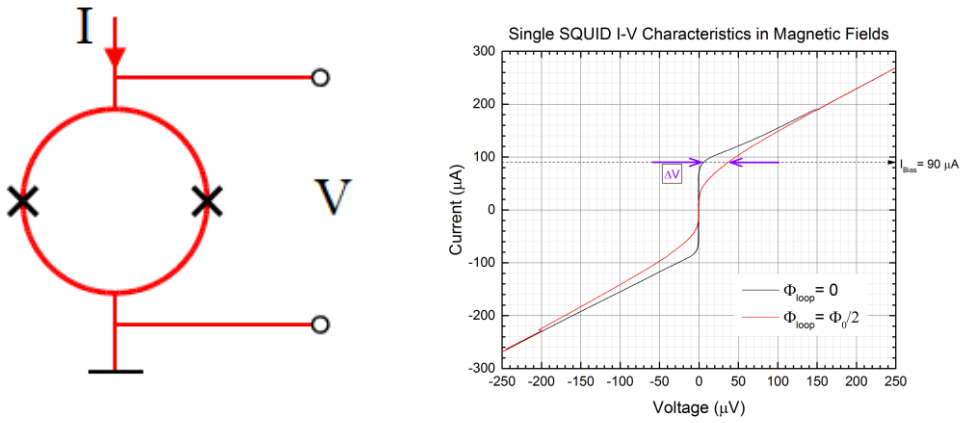

Figure 11: (Left) Schematic of a 2 junction "DC" SQUID, where the "X's" denote the Josephson junctions, the red lines denote superconducting wires, and "I" indicates the direction of the bias current. (Right) SQUID IV modulation in response to a single flux quanta.

A DC Superconducting Quantum Interference Device (DC SQUID) consists of 2 Josephson junctions connected in parallel forming a superconducting loop (Figure Above). The 2 junctions create quantum interference effects in the coherent order parameter around the superconducting loop when a magnetic field is applied. The 2 junction SQUID is analogous to the Young's double slit in optics, where the SQUID critical current will sinusoidally oscillate with applied magnetic field.

Closely following the model formulated by Tesche and Clarke [20], a DC SQUID with two identical resistively shunted Josephson junctions in parallel, interrupting a single superconducting loop, can be modeled by solving the simultaneous differential equations for each junction. The first Josephson equation for each junction

$$I_{1,2} = I_C sin\delta_{1,2} + \frac{V_{1,2}}{R_N}$$

can be combined with the second Josephson equation for each junction

$$\frac{d\delta_{1,2}}{dt} = \left(\frac{2e}{\hbar}\right) V_{1,2}$$

to write an analytical form of the simultaneous differential equations to solve for the SQUID voltage V_{SQUID}

$$V_{SQUID} = V_1 + L_1 \frac{dI_1}{dt} + M \frac{dI_2}{dt}$$

$$V_{SQUID} = V_2 + L_2 \frac{dI_1}{dt} + M \frac{dI_1}{dt}$$

Where $L_{SQUID} = L_1 + L_2$ such that L_i is the effective inductance of each SQUID arm, and M is the mutual inductance between the SQUID arms. The two junction currents are defined with the bias current $I_{bias} = I_1 + I_2$ where the phase differences across each junction δ_1 and δ_2 are related through the flux threading the SQUID loop $\Phi_T = \frac{\Phi_0}{2\pi}(\delta_1 - \delta_2)$. We have assumed both junctions are identical. The total flux threading the SQUID loop is equal to the sum of the applied flux and the Meissner currents circulating the SQUID (in the absence of inductance mismatch between the two SQUID arms). Using substitution and rearranging all terms, the time derivative ($dt \rightarrow d\theta$) of the two junction phases can be written in dimensionless form (lower case letters)

$$\frac{d\delta_1}{d\theta} = {}^{i}/_{2} - j - sin\delta_1$$

$$\frac{d\delta_2}{d\theta} = {}^{i}/_{2} - j - sin\delta_2$$

such that the dimensionless circulating current $j = \frac{1}{\pi\beta_L}(\delta_1 - \delta_2 - 2\pi\Phi_{applied})$, where the dimensionless SQUID modulation parameter $\beta_L = \frac{2LI_C}{\Phi_0}$. The dimensionless SQUID voltage is then equal to the normalized sum of the time derivative of the two junction phases

$$v = \frac{1}{2}\frac{d\delta_1}{d\theta} + \frac{1}{2}\frac{d\delta_2}{d\theta}$$

Using the same process as the RSJ model to integrate the junction phase to obtain an average voltage for each current bias, the SQUID voltage as a function of flux threading the SQUID loop can be numerically solved for by fixing the bias current and varying the applied flux. The effect of the SQUID modulation parameter β_L can also be modeled by fixing the SQUID critical current and varying the loop inductance (Figure below).

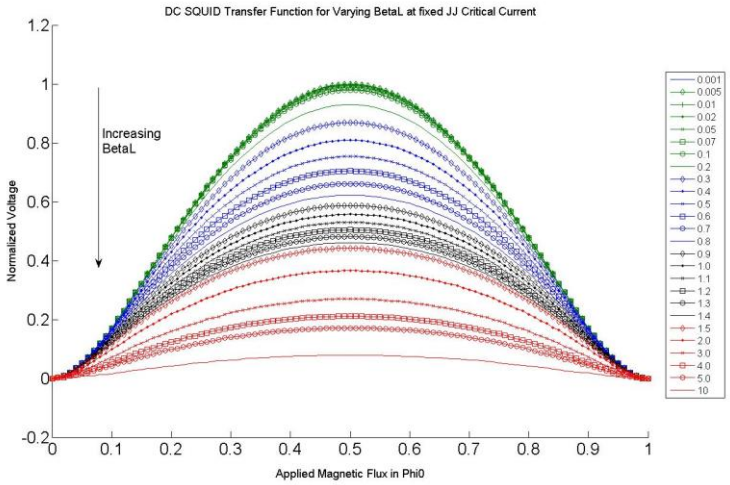

Figure 12: Numerical simulation of the DC SQUID using the RSJ model for many modulation parameters assuming a fixed SQUID critical current and a bias current $I_{bias} = I_C^{JJ} * 2.1$

As noted by Tesche and Clarke, the SQUID critical current modulates by at least 50% for $\beta_L \leq 1$. The normalized SQUID voltage also reflects this behavior, with 50% of the maximum voltage modulation ($I_C R_N = 1$) for $\beta_L = 1$. The SQUID voltage is maximized and virtually independent of β_L for modulation parameters less than 0.01. For $\beta_L \gtrsim 40$, the SQUID critical current modulation $\Delta I_C \sim \frac{\Phi_0}{L}$. These numerical solutions are only representative of a symmetric SQUID with identical junctions, where all curves in the Figure above are identical to

within a scaling factor. Asymmetric SQUIDs and dissimilar junctions will distort and/or horizontally shift the solutions presented here.

2. Simulations of Ion Damage in Nanoscale Barrier Regions

Motivation

There is great value to develop a simulation method to model ion damage Josephson junction parameters (I_C and R_N) as a tool to aid in circuit optimization. The optimization of complex circuits, such as digital logic gates, requires both detailed analysis of the device layout and predictive device models (Figure below) [21]. Layout analysis tools are key to extract device parameters for overall circuit simulations. Accurate device models are needed to refine the device layout in response to circuit simulations to achieve the desired specifications. The development of circuits containing many Josephson junctions, particularly design with many different junction parameters, necessitates a junction analysis tool that accurately simulates the physics within the barrier region. The electrical properties of the ion damaged barrier region ultimately giving rise to Josephson behavior are intricately sensitive to all aspects of the junction layout including: barrier dimensions, ion energy and dose, starting materials properties (T_C, J_C, microstructure), and the placement of nearby components. In general the electrical properties of a new junction layout cannot be accurately predicted from the simple scaling of a dissimilar, but empirically characterized layout. Hence the design and optimization of complex Josephson circuits demands the development of

device models that utilize physics based simulations of the ion damaged barrier to predict Josephson junction parameters.

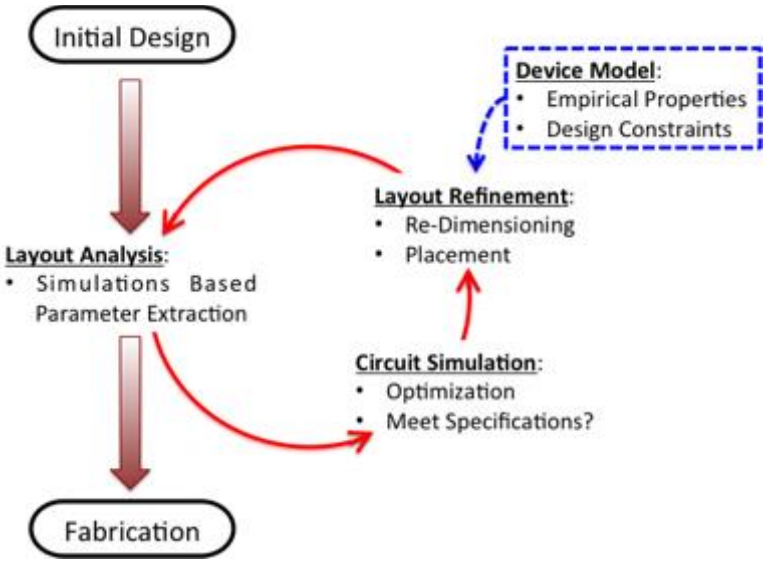

Figure 13: Process flow for the design of small scale Josephson circuits (adapted from [21]).

In this chapter we will construct a model of ion damaged Josephson junctions relying on the empirical properties of bulk films to generate 2D simulations of the T_C reduction in ion damage junction barriers. We employ Monte Carlo based simulations of ion induced structural damage to create the 2D seed data that is converted into the 2D simulation of T_C reduction. This model does not include the physics specific to superconducting weak links (e.g. proximity effect), however we do discuss how the model can be incorporated into ion damaged Josephson junction simulations using a phenomenological model of inhomogenous conduction through filaments of superconductivity in an ion damaged barrier. We show that this model can be used to describe the relative empirical properties of several different junction layouts including: T_C drop with increased barrier length, transition from bottom to top conduction with increased barrier length, and the correspondence of

ion range with barrier homogeneity. The model developed here is most useful as a tool to generalize the ion energy and dose required to produce ion damaged barriers with similar properties, in addition to minimizing the number of design and fabrication steps required for circuit optimization.

Numerical Simulations of Ion Damage

Ionized radiation is well known to cause damage and disorder into the surfaces of solid materials. The depth and severity of the damage is primarily a function of the ion energy, ion mass, and target density. There are generally two regions of ion damage: the transit region and the stopping region. Ions will be buried deep within the target material if they are sufficiently light (low Z) and high energy. These deeply transmitted ions will gradually lose energy to screening electrons (ionizing energy loss) and the atomic lattice (nonionizing energy loss) until they ultimately stop. It is possible to make films of material thin enough such that the majority of impinging ions pass through the film and become stopped in the substrate underlying the film (such as in all the datasets above). Films thinner than the ion stopping range are described as "ion damaged" while films thicker than the stopping range are "ion implanted". Structural damage is created throughout the beam path by: production of vacancy-interstitial defect pairs as atoms are knocked-out of their lattice sites (recoil creation), macroscopic lattice disorder when a sufficient density of defects are created, and heat "spikes" on atomic length scales occur when any energetic ion (radiation or recoil) ultimately stops. The complete set of energetic collisions between atoms in a "target" induced by radiation is known as a collision cascade. The microscopic effects of ion

irradiation are difficult to experimentally observe, often requiring techniques that are destructive to the sample. However numerical simulations of atomic collision cascades using Monte Carlo techniques are well established.

Numerical simulations of the ion damage were performed in this work using the Transport of Ions in Matter (TRIM ver2011.08, stopping power ver2008) simulation package developed by Ziegler [22]. TRIM uses the Binary Collision Approximation (BCA) with quantum mechanical treatment of the atomic scattering cross sections assuming an amorphous target [22]. TRIM uses Monte Carlo techniques to calculate full collision cascades of both the incident ions and the recoiled atoms within the film. The Binary Collision Approximation or "linear" cascade approximation assumes that collisions between recoils and target atoms occur rarely. A linear collision cascade predominately consists of "primary knock-on" collisions that are independent of one another. In other words TRIM is most accurate when the target material has a low stopping power or the incident ion has a high effective energy.

The physical models of TRIM will breakdown when the collisions between incident ions, recoils, and target atoms cannot be considered independent. Many-body interactions and significant heating effects are particularly dominant when the primary knock-on recoils are energetic enough to create secondary or higher order recoils; a commonly encountered scenario in ion damage junctions. Ion damage decreases T_c primarily by electron scattering and reduced carrier density originating from ion induced atomic defects [23]. TRIM offers two different outputs to parameterize the structural damage: energy losses and atomic displacements. In light of the limited range of validity of TRIM, we choose to

use the energy loss rather than atomic displacement number since the energy loss will be less affected by the detailed nature of the collision cascade.

In this work superconducting YBCO was modeled using 5 different displacement energies in the form of $Y_1Ba_2Cu_3O_6+O_1$. Two different Oxygen displacements were used to explicitly account for the different plane and chain oxygen sites. $Y_1Ba_2Cu_3O_6+O_1$ was modeled in Monolayer Collision Steps using the following parameters:

Density: 6.54 gram/cm^3

1 part Y: Displacement energy 30 eV [24]

2 part Ba: Displacement energy 30 eV [24]

3 part Cu: Displacement energy 15 eV [25]

6 part O (O planes): Displacement energy 8 eV [26]

1 part O (O chains): Displacement energy 1 eV [27]

Lattice Energy for all atoms: 3 eV (TRIM Default)

Film Thickness: 300 nm

The film thickness was chosen to be thicker than the 100-200 nm thick films used in this chapter in order to avoid errors associated with layer interfaces in TRIM. Additionally, we assume the first few nanometers of material near the surface are nonconducting (processing degradation) do not contribute to conduction. All TRIM outputs are normalized to the case without an ion dose, where the outputs are linearly scaled by the ion dose to calculate the dose dependent parameters.

Properties of Ion Damage Bulk Films

To calibrate the numerical simulations of the ion damaged barrier regions, we hypothesize that the ion irradiated film properties are the same for bulk YBCO films and within single nanoscale YBCO grains. In particular, we assume the reduction in critical temperature (T_C) and increase in residual resistivity (R_0) is the same for bulk films and nanoscale grains. Both T_C and R_0 can be extracted from the resistance-temperature (RT) curve (Figure below). Ion damage increases the film resistance, often quantified by extrapolating the linear portion of the RT (above T_C) to zero temperature, where the y-intercept is equal to the residual resistance. In general ion irradiation can both reduce T_C [28] and broaden the superconducting transition width [23]; both effects observed in the Figure below. T_C suppression in the absence of broadening indicates a decrease the amplitude A of the superconducting order parameter $\psi = Ae^{i\phi}$ [29]. Radiation induced degradation of intergrain coupling increases the isolation between individual grains resulting in weakened phase coherence between grains. Each grain will retain a well defined T_C, but the diminished grain to grain coupling results in phase decoherence of the wavefunction which increases the superconducting transition width [30]. To account for transition broadening, a generalized T_C extraction is often used where T_C is defined at the midpoint of the superconducting transition. Using a series of irradiations, an empirical relation of the reduction of T_C and increase in R_0 is generated specific to the combination of film, ion, and ion energy.

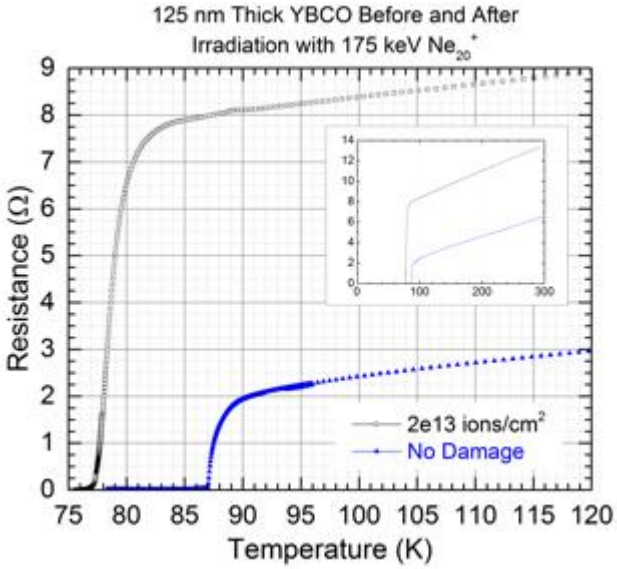

Figure 14: Resistance-Temperature curves of a 125 nm thick YBCO film before and after irradiation with 2.0e13 ions/cm2 of 175 keV Ne ions. Data taken from a 5mm x 5mm sample implanted in parallel with implantation masked junction circuits. Sample uniformly irradiated using broad beam with 0 degree tilt angle.

We choose to calibrate our ion damage simulations using the results of 4 different studies of irradiated YBCO bulk films (Figure below). The 4 different studies where chosen to compare the effects of heavy (Ne) and light (He) ions. All irradiations were performed on films of at least 50 microns in width, ensuring many grains are sampled in the conduction path. Neon and Helium are also chemically inert ensuring that damage is mediated through structural defects rather than chemical interactions. The first dataset was reported by White and Dynes [31] using 1 MeV Ne_{20}^{+} aka "1000Ne" incident onto 200nm thick YBCO ($T_C = 92\ K$). The second study used 175 keV Ne_{20}^{+} aka "175Ne" to irradiate 150 nm thick YBCO ($T_C = 89\ K$)[32], where this combination of ion and film thickness is often used in masked ion damage junction fabrication [33]. Two different Helium datasets are used to contrast the Neon data, as the lower mass Helium ions can penetrate deeper and more uniformly than Neon. The

highest energy Helium that can be used with ion masked Josephson junctions (see Fabrication Chapter) is approximately 90 keV He_4^+ aka "90He", in this case bombarding 150 nm thick YBCO ($T_C = 89\ K$)[32]. For comparison 75 keV He_4^+ "75He" in 100 nm thick YBCO ($T_C = 90\ K$) is also included [34]. Amongst all 4 experiments, T_C was extracted using the midpoint of the superconducting transition. However the exact method used to determine the midpoint was different between the 3 studies, thus the accuracy of the 175Ne and 90He results should be the similar with small differences compared to 1000Ne and 75He.

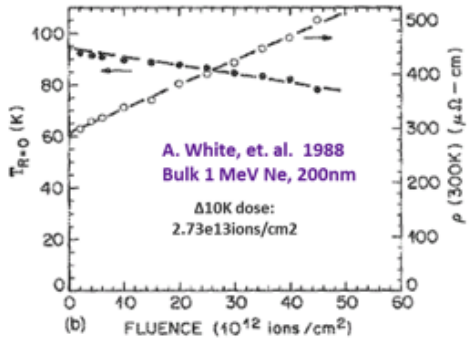

$$\frac{T_C}{\Phi_{1000Ne}} = -3.66 * 10^{-12} \frac{K}{ion * cm^2}$$

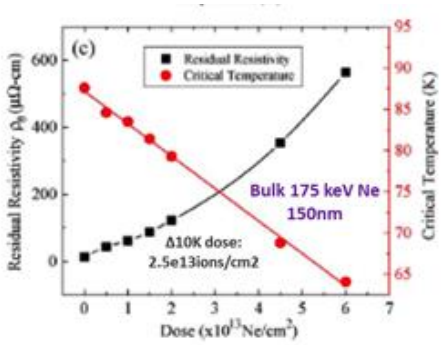

$$\frac{T_C}{\Phi_{175Ne}} = -4.0 * 10^{-13} \frac{K}{ion * cm^2}$$

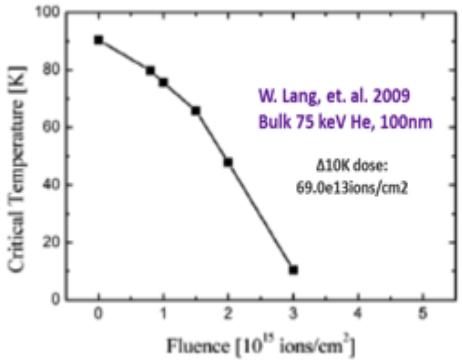

$$\frac{T_C}{\Phi_{75He}} = -1.45 * 10^{-14} \frac{K}{ion * cm^2}$$

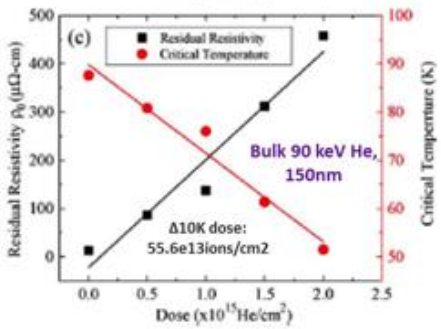

$$\frac{T_C}{\Phi_{90He}} = -1.8 * 10^{-14} \frac{K}{ion * cm^2}$$

Figure 15: Four different irradiation datasets for TRIM analysis for a Tc reduction. We choose the region ΔT_C =10K because of the approximately linear dependence on dose. (Top Left) 200 nm thick YBCO patterned into 50 μm wide bridges. (Top Right) 150 nm thick YBCO patterned into 5 mm x 5 mm. (Bottom Left) 100nm thick YBCO. (Bottom Right) 150 nm thick YBCO patterned into 5 mm x 5 mm.

YBCO is a covalently bonded material, where the structural damage created by ion irradiation is commonly correlated to the electrical damage [35]. In YBCO T_C is reduced by point defects such as vacancy-interstitial pairs creating electron and hole scattering, increased scattering between nanoscale grains, and decreasing the carrier density (superconductor-insulator transition). The reduction in bulk T_C is generally linear with ion fluence Φ_{ion} for at least the first 20-30 K reduction corresponding approximately to $\frac{T}{T_C} \geq 0.7$. The rate of T_C reduction versus fluence ($\frac{T_C}{\Phi_{ion}}$) in each case is shown in

the Figure above. Low energy ions interact strongly and create more damage than high-energy ions, thus lower doses are required to reduce T_C for low energy ions compared to high energy ions. The Ne datasets exhibit this trend, however the opposite is true for the He datasets. Since the experimental techniques were the same for 175Ne and 90He, we believe that the 75He study reports an anomalously low T_C reduction with fluence. Nevertheless, at high enough ion fluences all YBCO films undergo a superconductor-to-insulator transition [23], the onset of which will rapidly decrease T_C beyond the linear function observed at lower fluences. The superconductor-to-insulator transition is outside the scope of this work, in so doing we restrict our analysis to the first 10 K of T_C reduction. We remark that the bulk film critical current is more sensitive to ion damage than T_C, where the critical current exponentially decreases with increased fluence [28]. Hence in this work we restrict our analysis to T_C and R_0 i.e. parameters with a linear dependence on ion fluence. We now turn towards numerical simulations of the radiation induced structural damage to construct a model to describe the ion induced changes in the electrical properties of bulk YBCO thin films.

Simulations of Ion Damage in Bulk Films

To quantify the structural damage introduced into bulk YBCO films, we used the one-dimensional distributions of energy loss calculated by TRIM. The 1D distributions from TRIM are calculated in the bulk film limit. Energetic ions and recoils lose energy with each atomic collision until the ion or recoil ultimately stops. The energy lost can be broken down into at least two parts: ionization losses to the screening electrons and non-ionizing losses to the

atomic recoils and crystal lattice. In the language used by TRIM, the "Energy to Recoils" output is equal to energy transferred from a energetic ion to a recoiling atom. If the energy transferred to a recoil is larger than the energy required to create a stable vacancy-interstitial pair (aka displacement energy), then the recoil will become a moving atom within the collision cascade. All moving atoms experience "Ionization" losses to electronic "screening" excitations until a collision occurs where the kinetic energy is reduced below the local displacement energy i.e. the atom stops. Once the ion stops, TRIM captures the remaining kinetic energy in its "Phonon" loss output. Thus the total energy lost by a bombarding ion is equal to the sum of ionization and phonon losses in the language of TRIM.

Structural damage occurs through recoil creation, where energetic ions lose energy to atomic recoils via inelastic collisions. One way to measure these losses is to measure the total amount of energy deposited into the lattice by stopped ions and recoils i.e. Phonon losses in TRIM. Phonon loss is a misnomer, as the energy dissipated from a stopped ion is more accurately described as the sum of the energy of the new atomic configuration and the heat energy deposited into the lattice through "heat spikes" . Heat spikes are created when an energetic ion stops. Heat spikes are transient, non-equilibrium events that cool down on time scales much faster than lattice phonons [35]. For the remainder of the chapter we relabel TRIM's "Phonon" output to Nonlonizing Energy Loss to recoils (NIEL to recoils). The NIEL to recoils are strongly depth dependent, where the spatial distribution of NEIL to recoils is proportional to the number of ion induced atomic displacements.

We now attempt to build an empirical model to predict the shift in bulk T_C using the non-ionizing energy loss in an empirical method developed by Summers [36]. Similar calculations have also been performed by Tinchev with 100 keV Oxygen in 200 nm thick YBCO [37]. Non-ionizing energy loss is a measure of the average number of atoms displaced by ion irradiation [38]. These displacements, in turn, cause increasing electrical resistivity. In general non-ionizing energy losses are calculated from the product of the atomic cross section for interaction and the average recoil energy where the recoil energy must be corrected for ionization losses (Lindhard partitioning) [36]. Both the "Energy to Recoils" and "Phonon" outputs from TRIM can be used to estimate the NEIL to recoils. It is important to recognize that the "Phonon" output from TRIM is less than the total energy transferred to recoils as it excludes the ionization losses experienced by the moving recoils. We remark that very high energy ions can activate additional non-ionizing energy losses through the evaporation of the atomic nuclei i.e. nuclear inelastic collisions not just atomic inelastic collisions. However nucleus evaporation i.e. disintegration of the nucleus is unlikely for medium energy ions [36] and is not considered in this work (or in TRIM). To summarize TRIM's "Phonon" output is most analogous to the generalized non-ionizing energy loss, however the "Energy to Recoils" output should also produce similar results.

If TRIM's are accurate for all 4 ions considered here (1MeV Ne, 175keV Ne, 90keV He, and 75keV He), then TRIM should predict the same damage level for each ion if the experimental $\Delta T_C = 10$ K dose is used. In other words different ions and energies will create dissimilar damage levels, however the damage to reduce T_C by 10 K should be intrinsic to YBCO regardless of the ion

or energy. To compare the damage amongst the 4 ions, the simulations are scaled by the dose required to reduce T_C by the same amount (Figure Below Left). Note that the arrows denote the film thickness used in each experiment. Here we choose the dose required to decrease T_C by 10 K (see previous section): 2.73e13 ions/cm^2 for 1MeV Ne$^+$, 2.5e13 ions/cm^2 for 175keV Ne$^+$, 55.6e13 ions/cm^2 for 90keV He$^+$, and 69.0e13 ions/cm^2 for 75keV He$^+$. In the range of film thickness used in the 4 ion experiments, the energy loss is lowest at the top of the film and highest at the bottom of the bulk films. The energy loss near the top of the film is very similar for all ions except 1000Ne. The suppression of bulk film T_C can be derived from the non-ionizing energy loss (over 8 orders of magnitude) using the following empirical fit from Summers [36]:

$$\Delta T_C(K) = \left[0.8 * 10^{-5} * \left(Energy\ loss\ \left({}^{eV * cm^2}/_{gram}\right)\right)^{0.95}\right] * \frac{fluence\ \left({}^{ions}/_{cm^2}\right)}{10^{15}\, ions}$$

Such that

$$Energy\ loss\left(eV * \frac{cm^2}{gram}\right) = Nonionizing\ Energy\ Loss\ \left(\frac{eV}{cm * ion}\right) * \frac{1}{Density}\left(\frac{cm^3}{gram}\right)$$

We use this relation to convert TRIM's "Phonon" (NEIL) energy loss into T_C reduction as a function of depth (Figure Below Right). The material with the highest T_C will carry the supercurrent and dominate conduction. Therefore we assume the material with the lowest ΔT_C corresponds most closely to the bulk T_C after irradiation. The lowest ΔT_C in all 4 cases occurs at the surface, where the average ΔT_C reduction is 10K as expected from each ion dose. Thus TRIM's nonionizing energy loss to recoils loss combined with the Summers relation can accurately describe the irradiation induced T_C reduction in bulk films over a range of ions and energies.

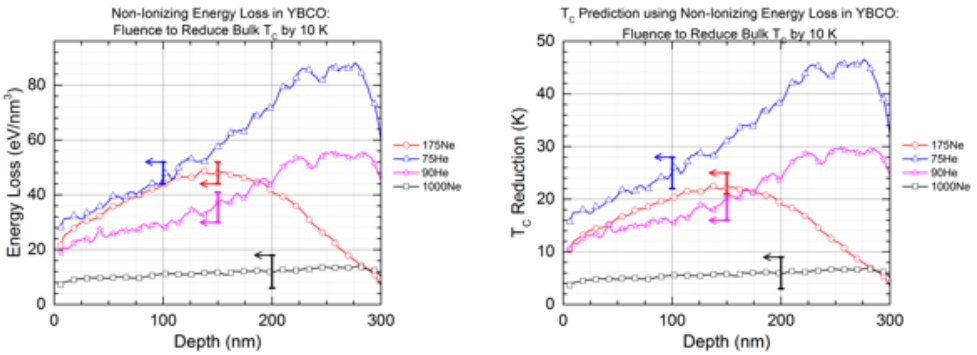

Figure 16: (Left) Non-ionizing "Phonon" energy loss as a function of depth for 4 different ions, the arrows indicate the film thickness used in each study. (Right) T_C reduction as a function of depth using the Summers empirical relation. Here 175Ne is 175keV Ne^+, 75He is 75kev He^+, 90He is 90keV He^+, and 1000Ne is 1000keV Ne^+.

To further examine the accuracy of the simulation model, we compare the T_C reduction for all three energy losses calculated from TRIM: "Energy to Recoils", "Ionization", and "Phonons" (NIEL) (Table below). The goal is to predict a ΔT_C =10 K reduction from TRIM to match the empirical $\frac{\Delta T_C}{fluence}$. An additional goal is to determine which TRIM energy loss output most closely represents the nonionizing energy loss to recoils (NIEL to recoils) defined in the Summers relation. We assume the supercurrent is carried near the surface and choose to compare energy losses at the single depth of 10 nm. TRIM's "Phonon" output does predict the expected 10K reduction for all cases except 1000keV Ne^+. Conversely, TRIM's "Energy to Recoils" output accurately predicts the T_C reduction for 1000keV Ne^+ and overestimates the T_C reduction for all other ions. TRIMs calculation of "Energy to Recoils" is equal to the sum of the "Phonon" and "Ionization" losses of the recoils. As noted by Summers, the NIEL to recoils must be compensated to exclude the ionization losses of the recoils. Therefore any prediction of T_C reduction that requires the addition of recoil ionization losses, in this case "Energy to Recoils" for 1000keV Ne^+, should

be outside the range of validity for the Summers relation. Either the ionization losses of the recoils produced from high energy Ne are incorrectly calculated in TRIM, or TRIM fails to capture all the nonionizing energy transferred to recoils in the "Phonon" output of 1000keV Ne^{+}. Thus our simulation model can describe the empirical bulk T_C reduction for moderate energy ions with limited accuracy for higher energies. Above all, our model contains sufficient detail and experimental calibration to enable a direct conversion of TRIM simulations into T_C loss for an arbitrarily sized ion source.

Table 1: Prediction of bulk film T_c reduction at 10nm depth.

Ion Type	Dose for ΔT_c=10K $\left(\frac{ions}{cm^2}\right)$	"Energy to Recoils" $\left(\frac{eV}{nm * ion}\right)$	Predicted ΔT_c Drop (K)	"Ionization" Loss $\left(\frac{eV}{nm * ion}\right)$	Predicted ΔT_c Drop (K)	"Phonon" Loss $\left(\frac{eV}{nm * ion}\right)$	Predicted ΔT_c Drop (K)
1000 keV Neon	2.73e13	80	10.5	1250	143.4	30	4.15
175 keV Neon	2.5e13	210	24.1	490	53.9	80	9.64
90 keV Helium	55.6e13	5	15.4	240	608.9	3	9.48
75 keV Helium	69.0e13	6	22.7	225	710.7	3.3	12.87

To solidify the physical basis for using nonionizing energy loss to recoils (NIEL to recoils) as a measure of ion damage in YBCO, we compare TRIM's calculation of NIEL to recoils to TRIM's calculation of total number of ion induced atomic displacements (Figure Below Right). Evidently, the nonionizing energy loss to recoils is a measure of the average number of displacements. Thus both TRIM's nonionizing energy "Phonon" loss and displacements density outputs equally describe the structural damage for a 10 K T_C reduction (Figure Below Left). Both the defect density and the nonionizing energy loss to recoils increase with film thickness up to the effective ion range. We estimate the effective ion range using the Stopping Range of Ions in Matter (SRIM) simulation, where the effective ion range is the mean ion range less the longitudinal straggle. The number of defect sites is proportional to the total number of displacements, where defects cause electron scattering at the Fermi surface and are directly related to T_C reduction [30]. Direct conversion of displacement number to T_C reduction is not trivial as the Cu and O defects will reduce T_C more strongly than Y and Ba defects [38][26]. The number of defects generated in each atomic site changes with ion species and energy, with over 50 percent of the total displacements occurring in the oxygen sites for 175 keV Ne^+ (not shown). Hence the T_C reductions calculated from atomic displacements require detailed knowledge of the specific T_C change from each lattice site. In general it is difficult to determine the distribution of vacancies among the various sublattices due anisotropic displacement energies and other factors, complicating estimations of the T_C change from each lattice site. Thus the nonionizing energy loss to recoils is the more useful

metric in this case, as the T_C suppression can be easily computed using the model described above without making assumptions of the damage sensitivity for different lattice sites.

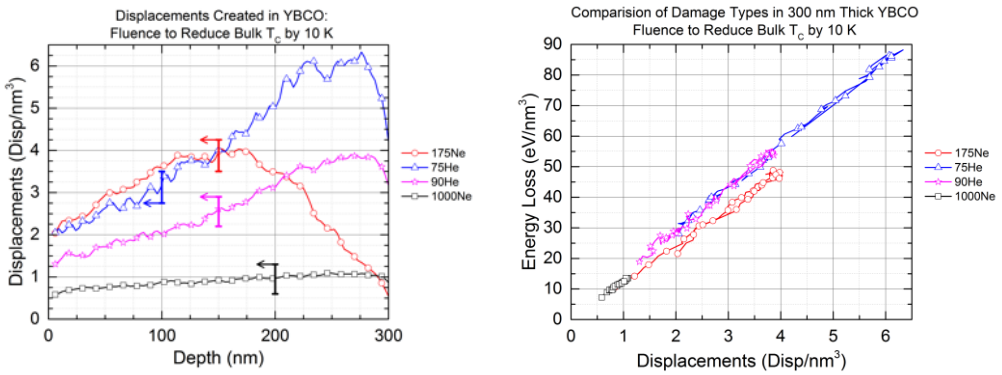

Figure 17: TRIM simulations of the number of displacements generated for 4 ions scaled by the ion dose to reduce T_C by 10 K. Note the arrows indicate the film thickness used in each study.

Simulations of Tc Reduction in Nanoscale Ion Damaged Barriers

Using the assumption that the bulk film properties apply to single YBCO grains, we can apply the model developed in the previous section to simulate the properties of nanoscale ion damaged barriers. In this section we construct a percolation model of transport through ion damaged barriers using 2D TRIM simulations of non-ionizing energy loss. In particular, we are interested in studying ion damaged barriers that form superconducting weak links which exhibit Josephson junction properties. Theoretically it is well understood that the temperature dependence of the critical current I_C traversing a weak link is complex, but easily parameterized with the barrier T_C in the general form $I_C \propto (T_C - T)^{\alpha}$ such that $1 \leq \alpha \leq 3$ depending on the barrier properties [39]. Thus the first step in simulating the electrical properties of a weak link is to construct a method to predict the barrier T_C. In principle both the T_C and resistance of ion damaged barriers can be estimated using the energy loss model

constructed in the previous section. In general the radiation induced T_C reduction in bulk films is proportional to the residual resistivity increase. However the physics of the proximity effect must be accounted for in nanoscale barriers, which is outside the scope of this chapter. Detailed models of the proximity effect are difficult to formulate in ion damage Josephson junctions due to the ill-understood role played by material inhomogeneities and the complex symmetry of the YBCO order parameter [39] [40] [41]. Consequently we restrict our analysis to the prediction of barrier T_C as a function of ion, barrier length, and film thickness.

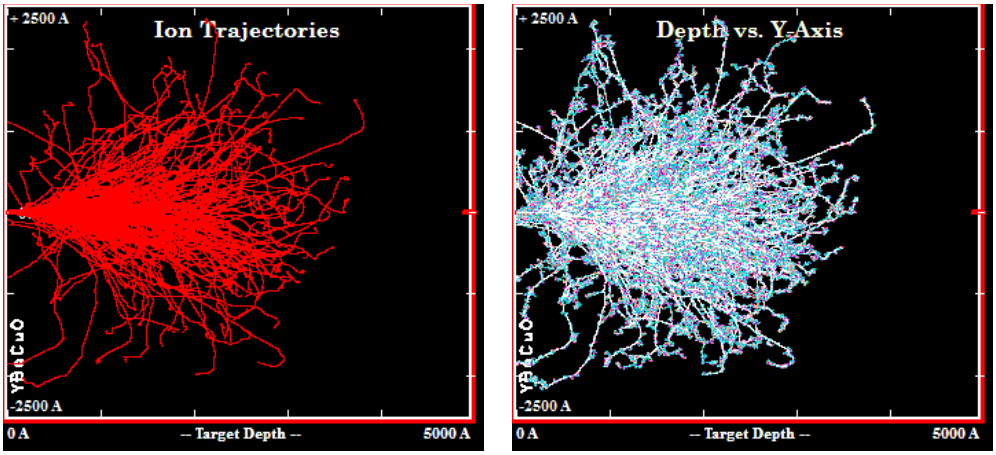

Figure 18: TRIM simulation of a point source of 175 keV Ne^+ entering from the left into 500 nm thick YBCO (See text below). (Left) Ne ion trajectories (Right) Both ion and recoil trajectories.

We construct a numerical model of ion damaged barriers using the 2D TRIM outputs. By default TRIM's 2D simulations calculate damage in a cross sectional form using a point source of ions (Figures Above). In this TRIM example, the paths of 200 ions of 175 keV Ne^+ (entering from the left) from a point source into YBCO are shown with and without recoils. The effects from both the ion and recoil tracks are recorded in a matrix consisting of 100x100 pixels where a 300 nm thick film will have a 3 nm x 3 nm pixel size. If the

damage from all the pixels within each depth are summed together, then the result is a 100x1 vector that is equivalent to the 1D bulk film results reported in the previous section. The point source enters the film between column pixels 49 and 50 (Top Middle of Figures Below). The 2D "Phonon" (NIEL) energy losses (name of TRIM output) from a point source of 175 keV Ne^{+} are displayed below (Left). We choose to analyze only the "Phonon" loss output from TRIM because the "Energy to Recoils" was unavailable in the 2D format. The highest energy loss per pixel occurs near the surface where the damaged region is narrowest, however the largest number of pixels damaged per depth (all pixels in each row) occurs about half-way through the 300 nm film. Using the method developed in the previous section, the Summers relation combined with the dose to reduce T_C by 10 K is applied to each pixel to generate a 100x100 pixel plot of the T_C reduction (Figure Below Right). The T_C reduction is lowest per pixel at the backside of the film where T_C is reduced the least, however a large concentration of implanted Neon will be present below 150 nm depth most likely degrading conduction in the otherwise low damage regions. Now that the 2D energy loss is calculated for a point source, the energy loss for longer barriers can be calculated by superimposing the energy loss from an array of these point sources.

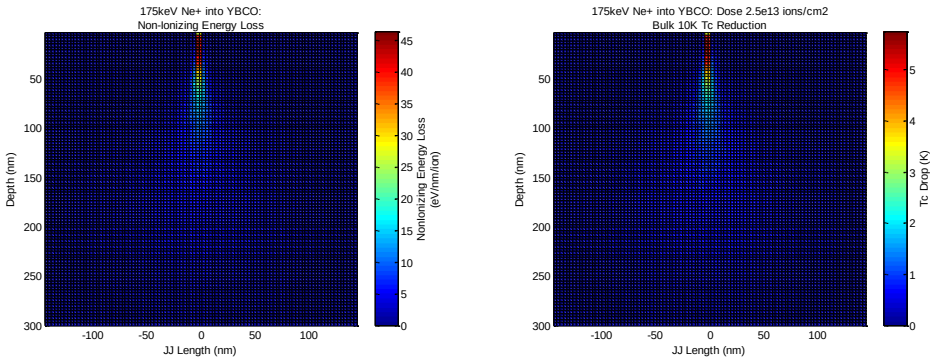

Figure 19: TRIM simulations of a point source of 175 keV Ne^+ ions into YBCO, note "JJ Length" is centered on the ion beam. (Left) TRIM 2D output of "Phonon" energy losses in a 300nm thick by 300nm wide film spilt into 100x100 pixels, data is not scaled for dose. (Right) Prediction of the T_C reduction calculated from the "Phonon" energy losses using the dose to reduce bulk T_C by 10 K (2.5e13 ions/cm^2).

We define the 2D "Phonon" (NIEL) energy loss from a point source as a matrix $[E_{Phonon}(0)]_{i,j}$, where each matrix element of the array (i=100 by j=100 pixels) is the average energy loss within the volume enclosed by the pixel (i,j). The 2D NIEL energy loss from a point source is shown in the Figure Above Left. Each row corresponds to a depth, where the depth at the i'th row is equal to: $[depth]_{i=1}^{i=100} = i * \Delta i$, with pixel size $\Delta i = 3$ nm. A similar vector of horizontal position from the junction center can be defined to label each column: $[JJ\ Length]_{j=1}^{j=100} = -149\ nm + j * \Delta j$, with pixel size $\Delta j = 3$ nm. Note that the outermost columns 1 and 100 are equal to the average damage at position (i,j) plus any damage generated outside of the simulation range (± 148.5 nm) but within the depth "j". To create a column vector representing the bulk damage as a function of depth, we integrate all the horizontal damage in each depth "i":

$$[E_{Phonon}(Bulk)]_i = \sum_{j=-148.5\ nm}^{j=148.5\ nm} [E_{Phonon}(0)]_{i,j}$$

To convert the any "Phonon" energy loss element $[E_{Phonon}]_{i,j}$ with units $(\frac{eV}{nm*ion})$, to a "T_C reduction" element $[\Delta T_C]_{i,j}$ in units of Kelvin (Figure Above Right), we use the Summers relation [36]:

$$[\Delta T_C]_{i,j} = \frac{\delta T_C}{\delta E} * \Phi_{ion} * \left([E_{Phonon}]_{i,j} * \rho_{YBCO}\right)^{0.95}$$

Where $\frac{\delta T_C}{\delta E} = 8 * 10^{-21} \frac{Kelvin*gram}{eV*particle}$, Φ_{ion} is the ion dose (ion/cm^2), and $\rho_{YBCO} = 6.54 \frac{gram}{cm^3}$ is the density of YBCO. Thus $[\Delta T_C]_{i,j}$ is calculated by assuming that the intrinsic bulk properties of the Summers model directly apply to single YBCO grains.

In order to simulate the induced damage from a finite length ion source $[E_{Phonon}(L)]_{i,j}$, the 2D energy loss from many point sources superimposed. For a barrier of length $L = (N-1) * \Delta j$, "N" is the required number of superimposed point sources. Since the 2D point source simulation in TRIM places the point source between pixels, the superposition to simulate a finite length barrier is performed with a for loop incrementing one pixel at a time:

$$[E_{Phonon}(L)]_{i,k} = \sum_{m=0}^{N} \sum_{r=1+m}^{100+m} [E_{Phonon}(L)]_{i,r} + [E_{Phonon}(0)]_{i,r-m}$$

Note that the size of $[E_{Phonon}(L)]_{i,k}$ is 100x(100+N) pixels. If a sufficiently large number of sources are superimposed, then the resultant damage approaches the bulk film limit. Since the simulation window is only 300 nm wide, the bulk limit onsets in the center of the simulation starting with barriers of length 300 nm. Once $[E_{Phonon}(L)]_{i,j}$ is calculated for a finite length barrier, the Summers relation can be used to convert the energy loss into T_C reduction: $[E_{Phonon}(L)]_{i,j} \rightarrow [\Delta T_C(L)]_{i,j}$. Using the superposition of point source method, it is

now possible to quantitatively compare the spatially inhomogeneous damage created between barriers of arbitrary length.

Both the magnitude and extent of the ion damaged region increase with junction length (Figures Below). In these simulations, 2.5e13 ions/cm^2 of 175 keV Ne^+ ions are normally incident on 300 nm thick YBCO in four different "barrier" lengths: 24 nm, 48 nm, 78 nm, and 300 nm. The dose applied to all barriers was chosen to equal the bulk simulations in the first section i.e. bulk T_C reduction of 10 K in a 150 nm thick film. Here barrier length is defined as the length of the irradiated region. The effective size of a 24 nm barrier is 24 nm in the plot plane by 3 nm perpendicular to the plot plane. The damage as a function of depth in the center of the 300 nm long barrier is equal to the sum to the damage of a uniformly irradiated bulk film. Note that the colorbar range is different for each simulation, indicative of the increased damage level in longer barriers.

The region of maximum T_C reduction (dark red) is nearest to the surface for narrow barriers and smoothly transitions deeper into the film for wider barriers. The spatial extent of the damaged region increases much faster than the barrier length up to the bulk film limit. The increased extent of the damaged region is due to lateral ion straggle outside of the direct beam path, creating a "straggle region" of inhomogeneous damage. The existence of the straggle region is experimentally well known [42], as straggle increases the barrier inhomogeneity and is undesirable for ion damaged Josephson junctions. Thus these 2D simulations are qualitatively accurate and are detailed enough to qualitatively compare a range of different layouts for nanoscale ion damaged barriers. Using this 2D construction of an ion damage

barrier, we can now analyze the barrier uniformity using a microscopic model such as the percolation model of transport.

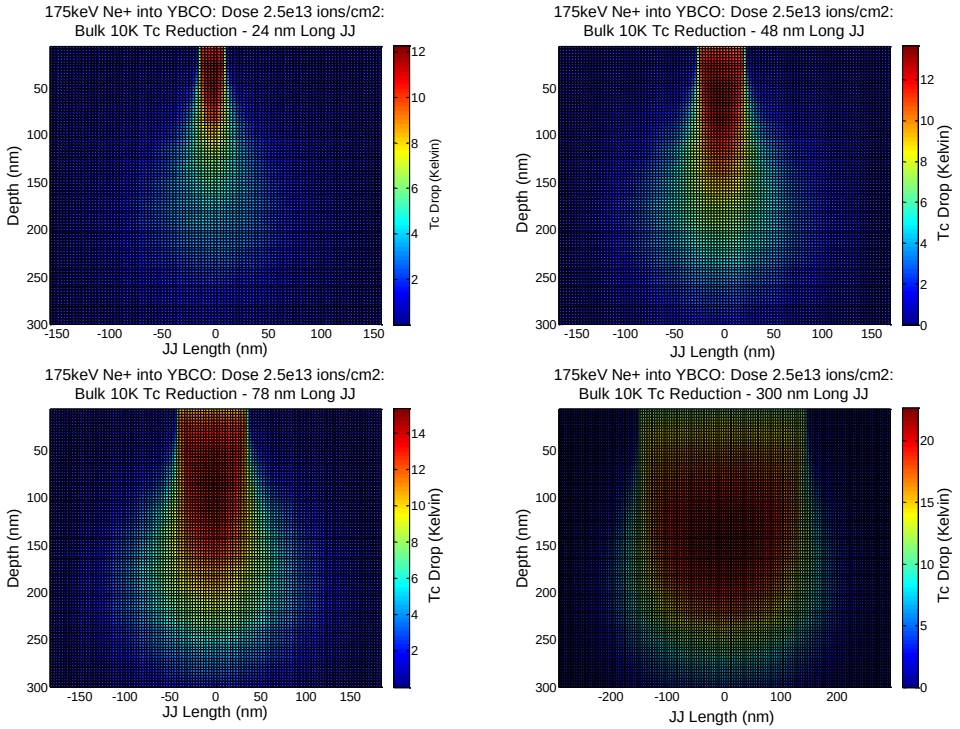

Figure 20: 2D TRIM simulations of the "Phonon" non-ionizing energy loss converted into T_C reduction using the Summers relation for 4 different barrier lengths: (Top Left) 24 nm long barrier, (Top Right) 48 nm long barrier, (Bottom Left) 78 nm long barrier, (Bottom Right) 300 nm long barrier.

Before performing a statistical analysis of the barrier inhomogeneity, a simple analysis of the depth dependent damage is possible. For each of the 100 rows or "depths" in the four $[\Delta T_C(L)]_{i,j}$ plotted in the Figure Above, we can extract the maximum ΔT_C at each depth i.e. the ΔT_C at the center of the barrier (Figure Below). Here we use the same assumption as the previous section, where the lowest ΔT_C pathway will carry the supercurrent and dominate the conduction such that $T_C(depth) = T_{Bulk} - \Delta T_C(depth)$. Hence we assume that supercurrents will first flow at the depth with the smallest overall T_C reduction. Inherent in this assumption is the acknowledgement that

conduction in YBCO is highly anisotropic, with weak transport between Cu-O planes/chains normal to the surface (c-axis direction). Thus for this simple model we assume that each row or "depth" of the TRIM simulation behaves as an independent transport channel in parallel with the other depths. Additionally, it is well known that narrow barriers require lower fluences than wide barriers to achieve the same T_C. By fixing the film geometry between 0-150 nm (red arrow Figure Below), the smallest T_C drop moves from the backside of the film to the front-side as the barrier length is increased from 15 nm to a "Bulk" 300 nm long barrier. Thus these simple simulations predict a crossover from front to back conduction as barrier length is increased. The crossover from back to front conduction is predicted to occur in 150 nm thick films in barriers approximately 76 nm in length for 175 keV Ne^+. Importantly, the T_C reduction predicted here is very close to the experimental values observed by Katz [43]:

Table 2: Comparison of the T_C reduction between experimental devices and TRIM based numerical predictions for nanoscale ion damaged barriers for a 200 nm thick YBCO film.

Barrier Length (nm)	Fluence (10^{13} ions*cm^{-2}) 200 keV Ne^+	Experimental ΔT_C (K) Katz, et. al. [43]	Simulation ΔT_C (K): 2.5e13 ions*cm^{-2} 175 keV Ne^+
24	1.0	1.8 - 3.2	3.5
26	1.5	10.8 - 15.4	
45 - 48	1.0	8.2 - 10.5	6.5
49 - 56	1.5	14.4 - 16.3	
74 - 77	1.0	9.3 - 14.3	9.5
76 - 82	1.5	16.3 - 21.8	

The accuracy of the simulation's T_C prediction is reassuring, as the Katz's ion energy (200 keV) and film thickness (200 nm) are significantly different than the bulk film calibration data used in the simulations (175 keV

and 150 nm respectively). We can conclude that the TRIM based simulations can describe the decreased damage and increased T_C observed in narrow barriers compared to wide barriers. In principle this result suggests that TRIM simulations can describe the structural damage observed in ion damage barriers of any length, thereby enabling direct estimate of barrier T_C for an arbitrary choice of ion dose and film thickness.

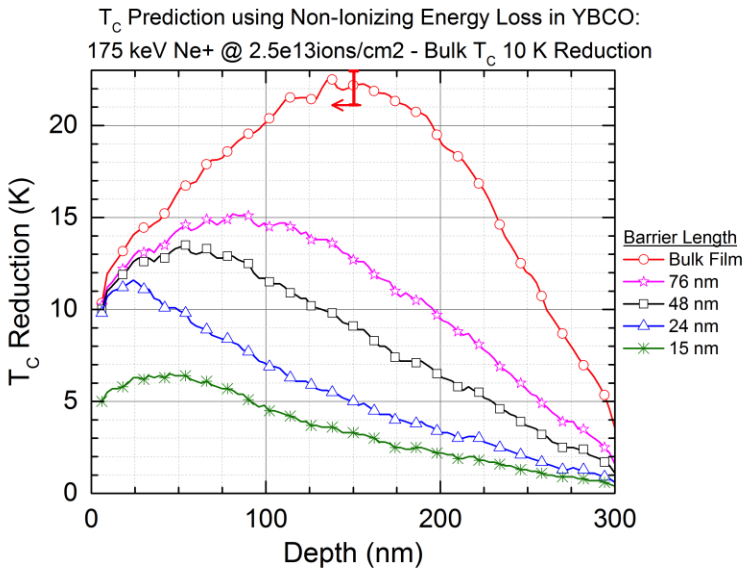

Figure 21: Plot of maximum T_C reduction as a function of depth for five different barrier lengths using 2.5e13 ions/cm^2 of 175 keV Ne$^+$. Red arrow demarks the range of film thickness for which an experimental 10 K drop is observed in bulk films at this dose.

Analysis Using Percolation Model of Ion Damaged Weak Links

The transport in ion damaged barriers is directly dependent on electron scattering from point defects created by ion damage, however a percolation model is used here purely for numerical convenience. In a percolation model of transport, supercurrents conduct through microscopically inhomogeneous regions of damaged superconductor and is assumed to be of a filamentary nature [40]. The aggregate of superconducting filaments traversing the barrier

will carry the supercurrent through the ion damaged region. The percolation model is phenomenological in that the model does not explicitly account for the physics of intergrain coupling, Josephson tunneling, or the proximity effect. Quantitative analysis of the mean T_C reduction produced by different ions is performed using TRIM (Figures Below). In the Figures below an equivalent dose for four different ions is applied to a 48 nm long region, thus the damage magnitude and homogeneity for different ions can be directly compared. Here we define each pixel of the simulation to represent an individual superconducting "grain", where a chain of adjacent grains must become superconducting together to form a continuous superconducting filament to traverse the damaged region. The critical current through the barrier is dependent on the distribution of superconducting grains contained within the barrier at any given temperature (less than T_C). The physical form of the grains within the damaged region is not well understood and is an active area of research [44], however we can assume that the number of isolated point defects rather than the number of series grains limit filamentary conduction. Once the distribution of granular T_C is known for a specific junction geometry and ion exposure, the percolation model can be applied to quantify the barrier uniformity and estimate the weak link properties.

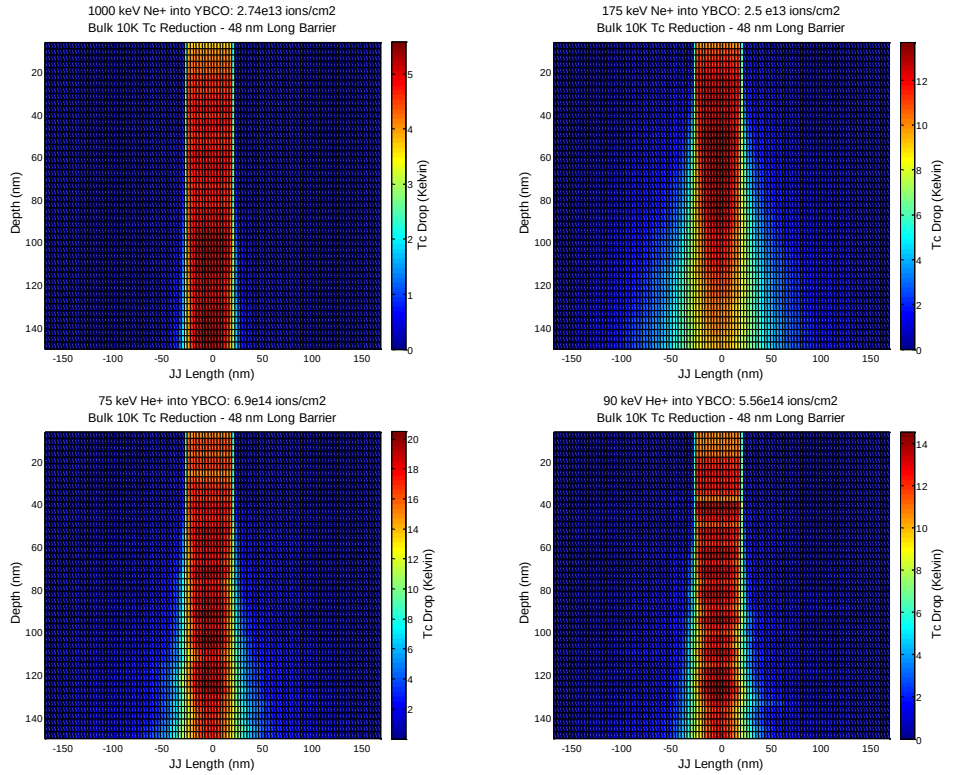

Figure 22: TRIM simulations of "Phonon" energy loss converted into T_C reduction for a 48 nm long source of four different ions into 150 nm thick YBCO: (Top Left) 1 MeV Ne^+, (Top Right) 175 keV Ne^+ ions, (Bottom Left) 75 keV He^+, and (Bottom Right) 90 keV He^+. The dose is different for each ion and is set such that an equivalent bulk film with have a 10 K T_C reduction.

To perform percolation analysis, we first collect all pixels within a 2D simulation $[\Delta T_C]_{i,j}$ into a single distribution $\mathcal{D}(T)$ of grain T_C's (Figures Below). We assume that the grain size identical to the barrier length for $n = 1$, half the barrier length for $n = 2$, etc. We closely follow the method described by [40]. All distributions have been normalized with the condition $1 = \int_{T_{\min}}^{T_{\max}} \mathcal{D}(T')\, dT'$. To exclude the "undamaged" regions and isolate the barrier properties, only pixels with greater than 1K T_C reduction are included in the analysis i.e. the highest grain $T_C = T_{\max} = T_{bulk} - 1\,K$. Additionally, the geometry has been fixed for all 4 ions with a 150 nm thick YBCO film and a 48 nm long irradiated region. The distribution for all barriers has a bimodal nature. (Figures Below), with

grouping at high and low damage as measured by T_C drop, respectively. The 1 MeV Ne^+ or "1000Ne" ion source produces the most homogeneous damaged region, evident from the narrow T_C distribution around $\Delta T_C = 5\ K$. The distribution of damage is significantly broadened for the other three ion sources (75 keV He^+, 90 keV He^+, and 175 keV Ne^+), with a small collection of "high damage" grains (ΔT_C large) and a dominant distribution of "low damage" grains (ΔT_C small). The T_C distribution is nearly flat from ΔT_C = 4-14 K for 175 keV Ne^+, indicating the worst barrier homogeneity amongst the four different simulations. Now that the homogeneity of the entire barrier region has been quantified, we can calculate the percentage of superconducting grains activated at a given temperature T by integrating the ΔT_C distribution $\mathcal{D}(T)$ between T_C^{bulk} and T.

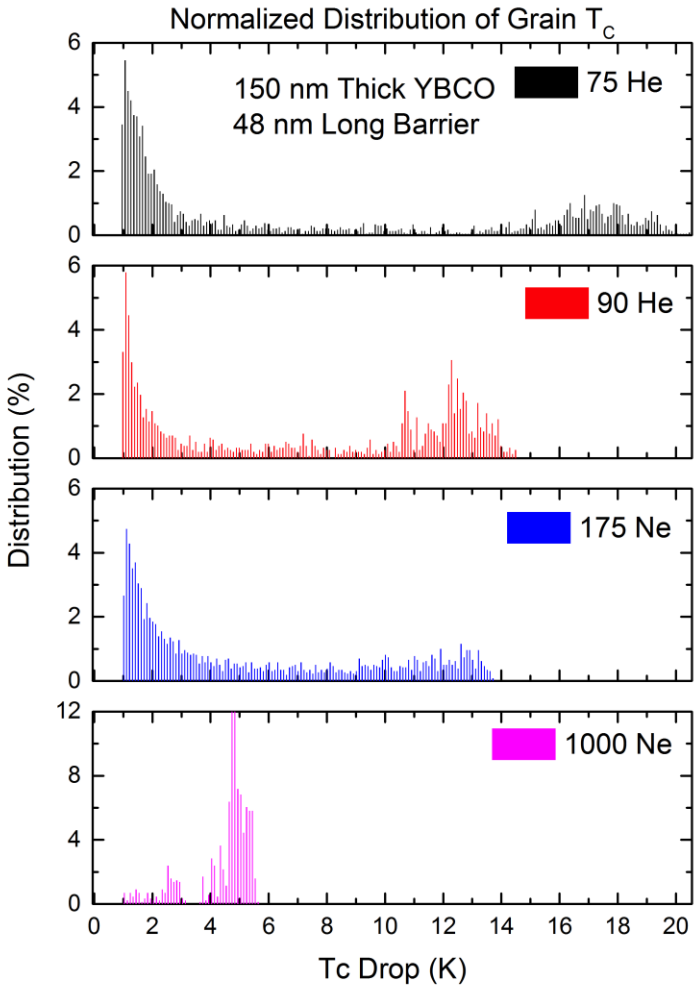

Figure 23: Distribution of T_C for all pixels or "grains" within a 150 nm thick ion damaged region created by 48 nm long ion sources. Note that the grains with a T_C reduction of less than 1 K are neglected in this analysis.

Each value in the granular T_C distribution $\mathcal{D}(T)$ represents the probability of finding a grain with $T_C = T'$. Then we can construct a probability distribution $\mathcal{P}(T)$ from $\mathcal{D}(T)$ that represents the percent of superconducting grains at a temperature T', with the highest grain $T_C = T_{\max}$, lowest grain $T_C = T'$, and T_C drop $\Delta T_C(T') = T_{bulk} - T'$. Then the percentage of superconducting grains within the barrier region operating between T' and T_{max} is $\mathcal{P}(T)$:

$$\mathcal{P}(T) = \int_{T}^{T_{\max}} \mathcal{D}(T')\,dT'$$

Once the percentage of superconducting grains $\mathcal{P}(T)$ is calculated, the last remaining variable is the number of grains "n" that must be aligned to form a superconducting filament through the barrier. In general if the grain diameter D_{grain} is known, then the number of aligned grains through a barrier of length "L" is: $n = \frac{L}{D_{grain}}$. However the microscopic morphology of the ion damaged barrier is poorly understood, however intuitively grain size is must be larger than the simulation pixel size (3nm x 3nm). Once the number of aligned grains is known, then the probability to have n grains aligned is $P^n(T)$ (Figure Below). The longer the superconducting filament, the less likely the path will be formed. Thus the probability distribution $\mathcal{P}(T)$ is not only equal to the percentage of the barrier region that is superconducting, but $P^n(T)$ represents the probability of creating a superconducting filament consisting of n aligned grains.

In the Figure Below, we plot the probability of superconducting grains for 1, 2, and 3 aligned grains (grain size equal to barrier length for $n = 1$, half barrier length for $n = 2$, etc.) with a shaded region to signify the most likely operating range of the barrier. The number of adjacent grains required to traverse the barrier defines the number of "aligned" grains. Note that the simulations assume an undamaged film $T_C = 90$ K, and neglect pixels with less than 1 K of T_C reduction. To aid in interpretation the percolation analysis is performed on a "Bulk" ion damaged barrier (300 nm long), where the measured of bulk films T_C^{Bulk} is marked for clarity. The required percentage of superconducting grains to produce a finite critical current threading a barrier

is equally as unknown as the typical grain size. Experimentally bulk films irradiated with 2.5e13 ions/cm^2 of 175 keV Ne$^+$ superconduct at $T_C = 80$ K, which corresponds to only 30% of the barrier region in the 300 nm long simulations. The onset of superconductivity for 30% of the barrier agrees well with theory, as the critical volume fraction for percolation conduction in a 3D continuum model is approximately 20-30% [45]. At temperatures much lower than T_C, nanoscale barriers with a high percentage of superconducting grains will eventually become strong links that typically exhibit undesirable flux-flow behavior [40]. Thus the superconducting grain probability for "bulk" ion damaged films using a TRIM simulation of the inhomogeneous damage qualitatively makes sense.

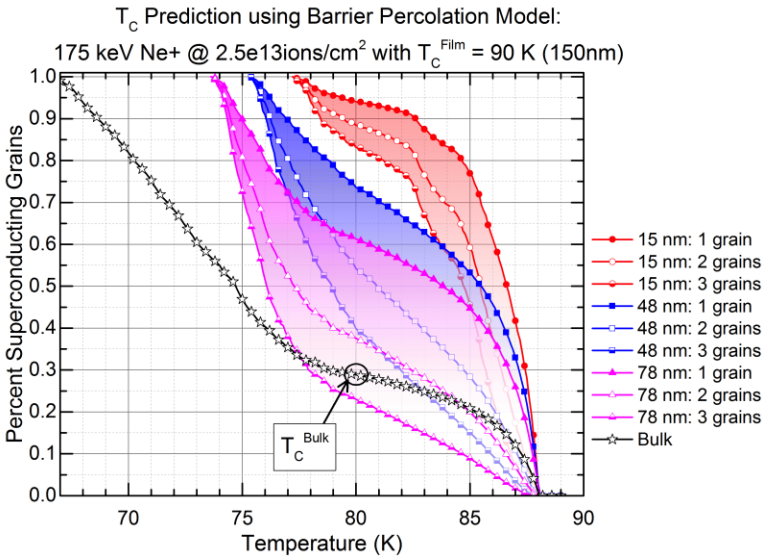

Figure 24: Simulations of the probability or percent of a 150 nm thick ion damaged barrier region that is superconducting between temperature T and the undamaged film $T_C^{Bulk} = 90$ K for 3 different barrier lengths. The number of grains that must be aligned to create a superconducting filament traversing the barrier is also plotted.

Using the shape of the bulk damage $P(T)$ as a guide, we can analyze the properties of nanoscale barriers. The temperature dependent probability

of creating a superconducting filament $P^n(T)$ (Figure Above) is an average measure of the filament density, as it assumes conduction throughout the barrier region without consideration of the spatial distribution of the damage or anisotropic conduction in YBCO. The shape of the temperature dependent probability will reflect upon the temperature dependence of the barrier I_C [40]. For instance in the bulk film simulation, the experimental T_C corresponds to a positive inflection point when only 30% of the film is superconducting. Similar inflection points are present at ~83 K for the 15 nm barrier, ~80 K in the 48 nm barrier, and ~77 K for the 78 nm long barrier. The temperature of all three inflection points fall within the operating range of the 175 keV Ne^+ junction data presented in Table 2 (Previous Section). The $P^n(T)$ systematically shifts towards colder temperatures with increased barrier length further describing the junction data in Table 2. The barrier inhomogeneity also appears to increase with barrier length, as evidenced by the diminished probability to create a superconducting filament. A homogeneous barrier is expected to have sharp probability increase at the temperature corresponding the average damage level. Thus the percolation model constructed with the nonionizing energy loss or "Phonon" output from TRIM appears to qualitatively describe the decrease in barrier T_C with increased barrier length (constant dose), quantify barrier uniformity, and qualitatively describe the systematic transition in damage from narrow barriers to bulk films.

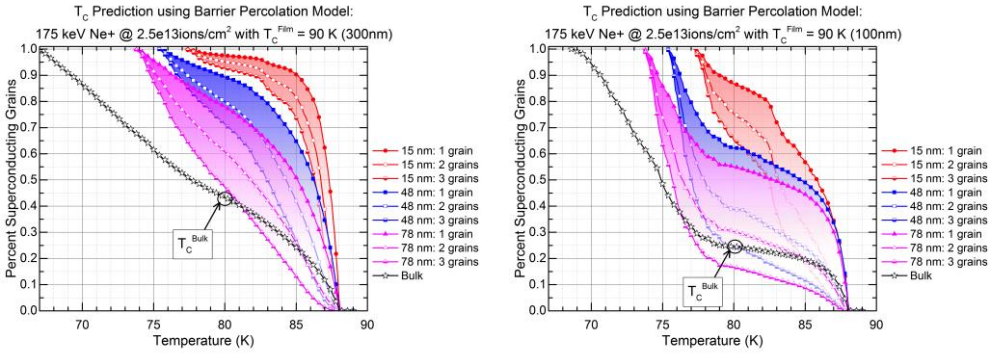

Figure 25: Simulations of the superconducting filament probability for percolation transport through an ion damaged region at a given temperature T (undamaged film $T_C^{Bulk} = 90$ K) for 3 different barrier lengths in two different film thicknesses. (Left) 300 nm thick film, very inhomogeneous limit. (Right) 100 nm thick film, homogeneous limit. The empirical T_C of a 150 nm thick film irradiated with 2.5e13 ions/cm^2 of 175 keV Ne$^+$ ions is marked on the bulk simulation for reference.

The general shape of the filament probability curve for ion damaged barriers changes with film thickness, especially when the film thickness is on the order of the ion range. The T_C reduction in bulk films will decrease with film thickness, until the film is thicker than the ion range resulting in zero T_C reduction as the undamaged backside carries the supercurrent. Qualitatively a slow increase in the probability of creating superconducting filaments suggests a high level of damage inhomogeneity. Inhomogeneous barriers will have a continuous gradient of damage from low to high T_C reduction. A continuous gradient of damage, such as in the bulk 300 nm film, creates a flat distribution of granular T_C, which results in a slow, monotonic increase in $P^n(T)$ (Figure Above Left). A 300 nm thick film is thicker than the 190 nm range of 175 keV Ne$^+$ ions (Stopping Range of Ions in Matter "SRIM" calculation). Thus the backside of the film is weakly damaged creating the slow increase in filament probability as temperature is reduced for the 48 nm and 78 nm long barriers (Figure Above Left). For the 300 nm thick, 15 nm long barrier 90% of grains

superconduct within 5 K of the T_C^{Bulk} $(n = 1)$, but the remaining 10% of grains require an additional 7 K reduction to fully superconduct (T_C^{min} ~77 K).

It is easy to understand the behavior of the 15 nm long barrier in 300 nm films, by examining the 15 nm long barrier in 100-150 nm films. In the 100-150 nm thick, 15 nm long barriers the filament probability is diminished compared to the 300 nm film simulations and exhibits two inflection points at 83 K and 78 K. We interpret the differences between thick and thin 15 nm barriers to inhomogenous damage where the majority of damage occurs within the first 100-150 nm of from the top surface. The thick 300 nm films must then contain a low damage region ($\sim 5\ K\ T_C$ reduction) shorting conduction on the film backside, such that the overall barrier strength is greatly diminished compared to the thinner 100-150 nm films. Ultimately a very thick film, much greater than the ion range, will make the probability distribution independent of film thickness i.e. the deeper portion of the film will not be damaged.

Intuitively the barrier uniformity can be improved by choosing a sufficiently small film thickness so that straggle region damage is minimized i.e. high uniformity occurs in thin films. Homogeneous barriers will have a sharp, nearly discontinuous transition in the conduction direction from undamaged to uniformly damaged regions. The homogeneous barrier will then possess a strongly bimodal distribution of undamaged and damaged grains, which will create a pronounced turning point in the filament probability at the T_C corresponding to the uniformly damage region. In other words the grains with "high" damage are significantly more damaged than the "low" damage grains such as in the distribution for 1 MeV Ne^+ (Figure previous section).

The 100 nm thick "bulk" film exemplifies the bimodal effect (i.e. sudden transition from undamaged to uniform damage region), where the probability remains constant between 20-30% for a 7 K range before the last 70% monotonically transition into the superconducting state over a 9 K range (Figure Above Right). The bimodal effect is also clear for the 48 nm and 78 nm long barriers (100 nm thick), where the probability is stabilized between 78-86 K (Figure Above Right). Thus a strongly separated bimodal distribution of granular T_C is desirable for SS'S junctions, where the S' material is operated above its T_C creating SNS junction behavior [46]. The barrier of a SS'S junction with a strongly bimodal distribution of damage will either exhibit stable Josephson properties over a broadened range of temperature or the barrier will be too long behave as a Josephson junction. In either case, the our percolation model is sufficiently detailed and calibrated with experimental data to estimate the uniformity of an arbitrary length ion damaged barrier within a specific temperature range as a function of film thickness.

Conclusion:

In this chapter we used the Transport of Ions in Matter (TRIM) simulation package to build a simulation of the electronic properties of ion damaged barriers in superconducting $YBa_2Cu_3O_7$ (YBCO) in the context of ion damage Josephson junctions. When a sufficiently narrow region of thin film YBCO is bombarded with energetic ions, a weak link is formed which can behave as a Josephson junction. The construction of a predictive device model for ion damage Josephson junctions is an active goal for research [47]. It is well understood that multiple mechanisms are involved, including the proximity effect [48] [39], the Josephson effect, and the physics of transport across interfaces [49]. In lieu of a precise device model, we have constructed an empirical device simulation incorporating a phenomenological model of transport via a percolative network of superconducting filaments with a distribution of T_C's traversing the ion damaged barrier [46] [40].

The spatially dependent non-ionizing energy transferred to recoiling atoms from bombarding ions was simulated by TRIM and converted into an estimate of the distribution of T_C in the ion damaged region [38]. Using this simulation we were able to model the T_C reduction in bulk films, the T_C dependence of SS'S junctions as a function of barrier length and thickness (superconducting barrier S' with reduced T_C), as well as analyze the effect of barrier non-uniformity on the temperature dependence of the barrier strength. We demonstrated that the movement of the maximum damage region from the film backside to the topside describes the decrease in barrier T_C observed in very narrow barriers. Similar numerical results have been previously reported for ion damage junctions [46], but this work differs in the use of 2D simulations

to generate a detailed and ion specific distribution of granular T_C. Our goal was to create a framework for a simulation tool that can be used to predict the properties of ion damage barriers for a specific junction layout (barrier length, film thickness, ion energy, and ion fluence). Predictive models of arbitrary junction layouts are technologically necessary to perform circuit simulations of sufficient accuracy to optimize the design of complex Josephson circuits.

Modeling percolative transport through ion damaged barriers is most valid when the distribution of grain T_C in the damaged region is experimentally constrained. The percolation model assumes that the ion damaged barrier region consists of unconnected but superconducting grains with a reduced T_C. As the temperature is reduced from the T_C of the undamaged material, a fraction of the grains will become superconducting in the barrier region. The barrier resistance drops with an increased fraction of superconducting grains, and a zero voltage current will onset once at least one filament of adjoining superconducting grains is formed through the damaged region. Thus an estimate of the critical current $I_C(T)$ through a barrier of cross sectional area "A" can be calculated using a percolation model:

$$I_C(T) = J_C(T) * A * P^n(T)$$

Where $J_C(T)$ is the critical current density roughly proportional to $(T_C - T)^\alpha$, where $1 \leq \alpha \leq 3$ depending on the nature of the barrier i.e. SIS, SNS, SS'S, etc [39]. In this work we have not attempted to calculate the $I_C(T)$ for each simulation, as we do not have a model that can predict the exact form of $J_C(T)$ based on TRIM simulations alone.

The model developed here can generally describe the layout dependence of the T_C in YBCO ion damaged weak links, however more work and a better understanding of structural damage in YBCO is necessary to predict the temperature dependent I_C and R_N parameters most relevant to ion damage Josephson junctions. Future work to validate the simulation accuracy should include direct comparison of the predicted T_C with a comprehensive collection of junction data over a range of film thicknesses and barrier lengths. The bulk film data used here suffers from an ambiguity in the method of T_C extraction between different studies in addition to probable film morphology differences. Additionally, the Summers model explicitly requires the total energy transferred to recoils (less electronic screening effects) for maximum validity, which is not directly available in 2D form from TRIM. Thus we have restricted our analysis to TRIM's 2D "Phonon" output to calculate the non-ionizing energy loss to recoils for the analysis of nanoscale barriers. Consequently the accuracy of the results presented here can easily be improved upon by developing a model that incorporates the all the energy transferred to recoils.

The largest ambiguity in the use of the percolation model is the grain size within the barrier and the functional form of $J_C(T)$. TRIM is unable to predict a precise morphology in the ion damaged region, and in general it is difficult to quantify grain size in an ion damaged barrier that is itself the size of a typical grain boundary. Furthermore, the predictive power of our simulations is limited to barrier lengths greater than TRIM's pixel size; 3 nm in this case. Intuitively, the most probable filament construction for percolative transport in narrow barriers will occur for the least number of series grains ($n = 1$). The results presented

here also suggest that the shape of the T_C distribution can be used to estimate the quality of the weak link, where the quality is tied to the functional form of $J_C(T)$ [50]. In general future models should account for proximity coupling as it is well-understood that the proximity effect is important in Josephson junctions with barriers much longer than the effective coherence length in the barrier region [50]. Thus numerical simulations using the percolation model are well constrained and adaptable to a variety of situations when general design requirements such high barrier uniformity and minimized barrier length are considered.

We have demonstrated a model that is capable of describing the T_C reduction in ion damaged bulk films. By assuming that the properties of bulk ion damaged films are the same as the properties of single YBCO grains, we used TRIM's 2D "Phonon" energy loss calculation to construct an empirical distribution of granular T_C to describe distribution of damage in an ion damaged barrier. However it is well known that defects cause electron scattering at the Fermi surface resulting in T_C reduction. Thus the granular conduction model is purely a mathematical construction to describe percolation in the presence of defects. This model is only valid for barriers with a finite T_C (S' barriers) and for damage levels where the bulk T_C reduction is linearly dependent on the ion dose. Ion damaged barriers of this nature are technologically important for devices that must operate near the film T_C. The model assumes the film is initially homogenous and undamaged (i.e. good starting material), thus the model does not account for the effect of film morphology. Inhomogeneous films such as those containing flux pinning sites will increase the barrier inhomogeneity and alter the rate of T_C reduction with

ion fluence [44]. The model is also most valid for barriers constructed in films thinner than the effective ion range, where the effective ion range can be used as a design curve equal to the mean ion range less the longitudinal straggle length. Thus we have proposed a simulation based device model to analyze the layout of ion damage weak links that can be used to predict junction parameters of SS'S Josephson junctions where the S' barrier is a superconductor with T_c less than the S electrodes.

3. Device Fabrication and Measurements

Introduction

In this chapter we describe the construction and measurement of Superconducting Quantum Interference Devices (SQUIDs) in $YBa_2Cu_3O_7$ using ion damage Josephson junctions. The fabrication of superconducting integrated electronics from $YBa_2Cu_3O_7$ thin films is a uniquely challenging task. Significant advancements in YBCO materials science have been made since the 1980's, and in this thesis we discuss the current state of the art in single layer materials utilizing ion damage Josephson junctions. First we will discuss the high level process flow to construct a device. Then we will consider an average design scenario for a YBCO SQUID constructed from ion damage Josephson junctions. Next we will describe each fabrication process in detail followed by a description of the measurement techniques used to characterize the devices.

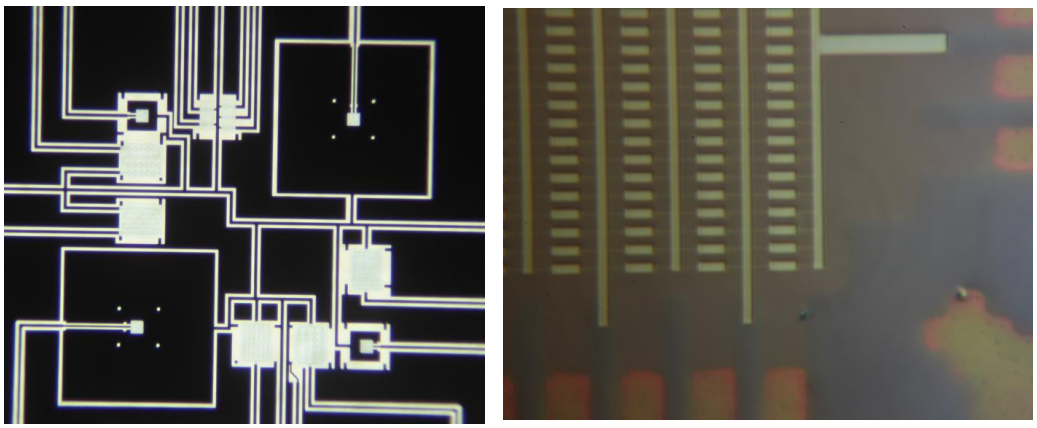

Figure 26: (left) Backlit optical photo of a completed single layer YBCO superconducting integrated circuit. Scale: 10 micron wires (right) Top-down optical photo of a YBCO integrated circuit covered with the trilayer implant mask after electron beam lithography exposure and development. Scale: 4 micron wide electrodes entering from the image bottom.

All devices studied in this dissertation were fabricated from c-axis oriented, polycrystalline thin films of $YBa_2Cu_3O_7$ grown on R-plane cut sapphire substrates (~0.5 mm thick). The R-plane sapphire lattice closely matches the $YBa_2Cu_3O_7$ a-b plane crystal latice and thermal expansion coefficient. Even with the close lattice match, the majority of YBCO films are deposited on sapphire using a Ce-O interfacial layer to minimize the thickness of sub-optimal YBCO near the sapphire interface. Materials were commercially sourced on 51, 76, and 100 mm wafers from two companies: Theva GmbH and Superconducting Technologies Inc. Materials were purchased with either a Ag or Au *in situ* capping layer to minimize the contact resistance and protect the underling $YBa_2Cu_3O_7$ from environmental degradation. Noble metal capping layers also enable more aggressive processing and lithography techniques that would otherwise damage YBCO. Wafer materials were diced into 5 mm x 5 mm and 10 mm x 10 mm "chips" using a Disco dicing saw.

First we will discuss the typical fabrication process flow and design scenarios, followed by a brief description of each processing step. Secondly

we will discuss the equipment and methods used to characterize these devices. Fundamentally two different material systems were patterned with nanofabrication techniques in this thesis:

1. Patterning, metallization, and etching of Au/Ag capped YBCO grown on sapphire
2. Electron beam patterning, reactive ion etching, and ion irradiation of PMMA-Ge-Shipley photoresist trilayer ion masks

Process Flow:

Fabrication of single layer YBCO integrated circuits is done in three general "layers": electrodes, contacts, and Josephson junctions. First the "electrode" layer pattern defines of all the wires, contacts, devices, and alignment marks using photolithography and etching processes. Next the "contact" layer pattern removes the *in situ* metal in all the Josephson junction and device regions of the electrode layer. Finally the "junction" layer defines the nanoscale barrier regions throughout the electrode layer that will be irradiated to create ion damage Josephson junctions. Two different junction fabrication techniques were used in this thesis:

1. High aspect ratio implant "canyon" masks that protect all but the junction regions from broad beam irradiation
2. Direct write of nanoscale junctions using focused ion beams

One method of patterning the ion damage Josephson junctions is to cover all parts of the YBCO electrodes with thick layer of photoresist except for the nanoscale barrier regions that will be ion damaged. High-aspect ratio, nanoscale "canyons" cut into the thick photoresist layer allows energetic

particles to reach the YBCO film only in the junction regions. Ions are stopped within the thick photoresist layer in all other regions. The canyons are patterned using electron beam "ebeam" lithography, which readily achieves the <80nm canyon widths required for the junction barriers. The figure below describes the process flow used for circuits with high-aspect ratio implant mask fabrication of Josephson junctions. The first four steps to fabricate a device are identical no matter the junction patterning technique. Photolithographic patterning of single layer YBCO circuits is done in a single step for subtractive (etch) patterning. Additive (deposition) patterning is not typically used due to the very high YBCO growth temperatures creating severe oxygenation constraints to grow high quality multilayer superconducting thin films [51]. All photolithography processes must be performed with bake temperatures less than 150 C also in order to avoid YBCO deoxygenation. Once the film is grown both wet and dry YBCO etching techniques exist, however the anisotropic dry etching techniques are more desirable when patterning narrow wires i.e. patterning high density circuits. At the time of this thesis, no dry chemical etch is known that offers a sufficiently high etch selectivity between YBCO and photoresist. Argon ion milling is a physical, low specificity, moderate aspect-ratio dry etch process used instead to cut through both the metal capping layer and YBCO layer in a single step. Photoresist masks for Argon ion milling processes must be approximately 0.5 um thicker than the thickness to be removed in the etching process to preserve solvent based removal (see following Argon ion milling section).

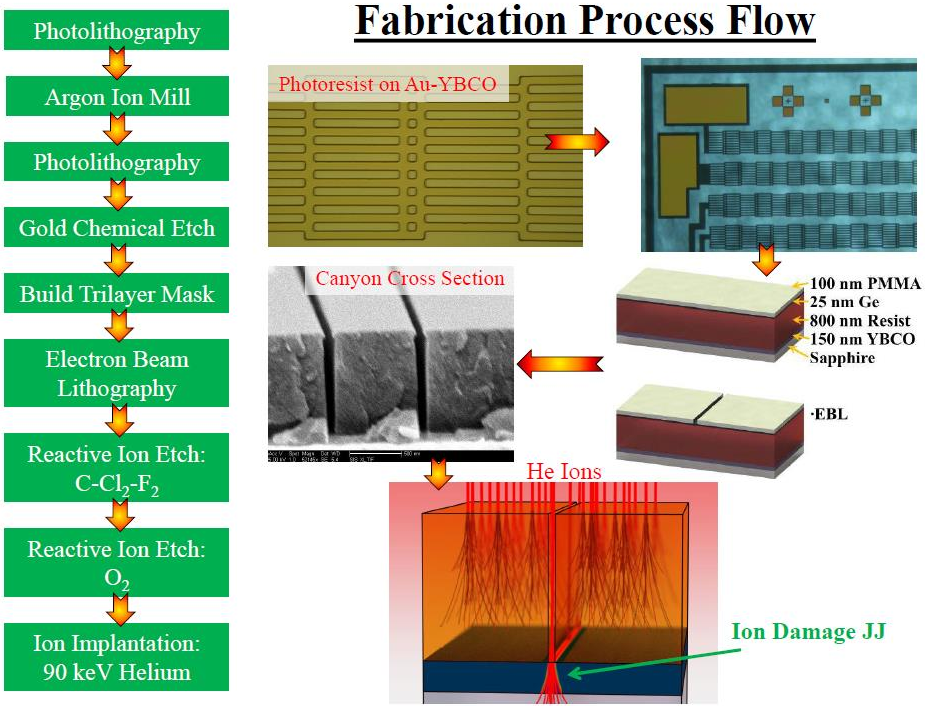

Figure 27: Process flow for single layer YBCO circuits using ion damage Josephson junctions constructed from the ion masking technique.

The complex trilayer resist system needed to create the "canyon" mask was first developed by Katz et. al. [46] (Figure Above). The trilayer consists of a bottom layer of thick photoresist "ion mask", a middle layer of Ge "etch stop", and top layer of 950k PMMA "ebeam resist". SRIM simulations of the desired ion species and energy are performed to estimate the ion range and hence minimum resist thickness required to protect the underlying YBCO layer. Electron beam lithography is used to pattern the junction layer into the top PMMA layer. The PMMA pattern is then transferred into the Ge middle layer using a $C\,Cl_2F_2$ (Freon-12) Reactive Ion Etch (RIE) process. Finally a low pressure, highly anisotropic oxygen etch is performed to cut the canyons into the photoresist through the holes formed in the Ge etch stop. Once the canyons have been cut into the ion mask, the sample is sent out to a commercial broad beam ion implantation facility where is precise ion dose is uniformly

irradiated over the complete sample area. Ion damage junctions can be stable for years at ambient conditions, however damage annealing begins at temperatures as low as 80-100 C. Hence all processing performed after junction fabrication such as ion mask removal and wire bonding must be performed near room temperature else the junction properties will be affected.

The intricate process of fabricating the trilayer implant mask requires careful attention to calibration and "spot checking" for each process step to verify the measure of the feature size and the completeness of the step (see Figure below). Calibration of the canyons formed in the implant mask after electron beam lithography and reactive ion etching (RIE) requires simultaneous processing of an additional YBCO and Si sample in parallel with the real samples. A YBCO sample is required to verify the electron exposure (dose) to use on the real samples, and a Si sample is required to cleave the trilayer mask after RIE to inspect the canyon cross section to verify the etch process. In electron beam lithography the feature size can vary by a factor of 10 for the same pattern depending on the electron dose. In general, the optimized electron beam dose will be different for each material under the resist: in this case YBCO, Au, and Si. For instance the dose to clear isolated 50nm wide lines in PMMA on YBCO is always larger than the dose to create the same feature in PMMA on Si. The smaller atomic mass of Si produces less secondary electrons than YBCO causing higher exposures for the same electron dose. In the case of a trilayer mask, the ion mask resist thickness also changes the required electron dose due to the separation from the high Z films by the low Z photoresist. In practice each dose test sample pattern consists of

many repeats of the desired pattern written at 5-10 different doses centered on the expected dose. Many repeats of the desired pattern are written for each dose to obtain reasonable measurement statistics. In this way, top down imaging of the YBCO calibrator sample after both electron beam lithography (EBL) and RIE etching can be performed to choose the optimal dose for the particular sample run. As well, cross sectional imaging of the Si sample (Figure Above Middle) after both EBL and RIE will capture the steepness of the canyon walls and the average width of each canyon to verify the etch parameters and etch rate (canyon depth) before running real samples. After mask processing is complete on the real circuits, at least 2 duplicates are made where multiple ion implant doses are used to further guarantee at least one sample contains junctions? with the required critical current at the desired temperature.

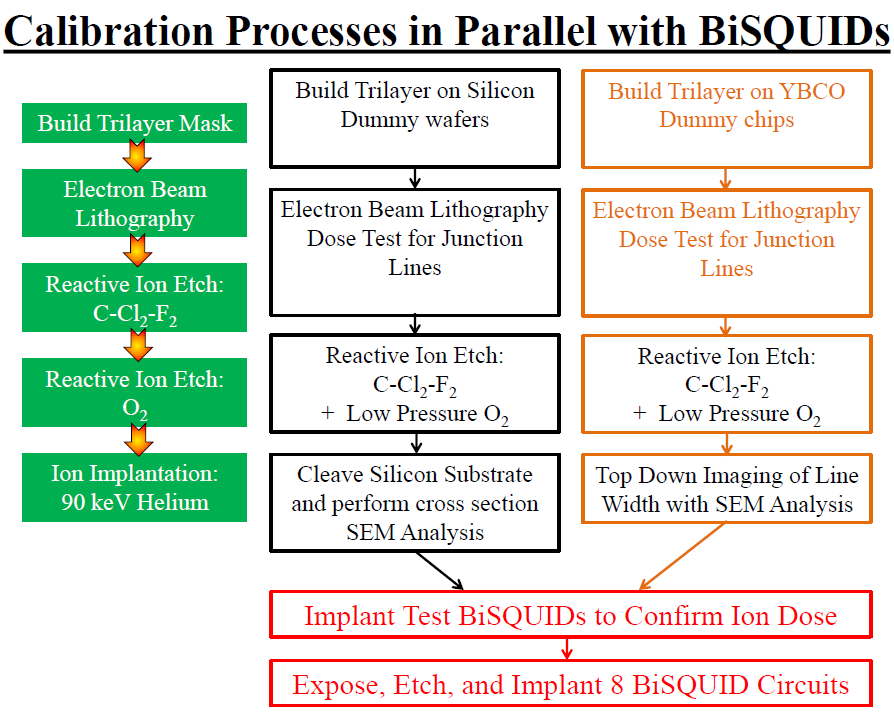

Figure 28: Multiple process calibration samples must be run in parallel with the real samples in order to verify the completeness of each process step and to spot-check throughout the complex process.

The second method of fabricating Josephson junctions included in this thesis is the direct write of a focused Helium ion beam to scribe the junction barriers. Focused Helium ion beams have only become commercially available in the last 5 years and are a continuously evolving technology. E. Cho and S. Cybart wrote all focused Helium beam junctions in collaboration with FEI and Qualcomm [19]. Direct write junction fabrication is much simpler than ion masking, since the direct write process is performed in one step. The direct write process will not be described here, as it is the primary subject of E. Cho's thesis where the interested reader will find complete details [19].

Typical Design Scenario: Ion Damage Josephson Junction

Effective circuit design requires not only accurate modeling of the circuit components, but also definition of the design constraints based on limitations in the fabrication process. A typical design scenario for Josephson junction circuits is to define a junction critical current (Ic) at a specific operating temperature range. In general there are at least four variables in the layout of a Josephson junction barrier for a specific Ic: barrier length, barrier width, film thickness, and ion dose. Josephson critical current is exponentially dependent on the barrier length, hence using a variable barrier length to construct multiple critical currents within a single circuit demands precision (<1 nm reproducibility). Additionally, ion damage Josephson junctions are almost always longer than the patterned barrier length due to incident ion straggle which is a strong function of reduced ion energy (see chap 2), ion direction, and film thickness. Perhaps the most undesirable effect of increasing barrier length is the diminishment of the junction IcRn product, which is not a strict constant for most YBCO junctions [8]. In fact increasing the length of a proximity junction with traditional superconductors will also result in low IcRn. Ic decreases exponentially with increasing barrier length, but Rn increases only linearly so IcRn decreases with increasing barrier length. Thus the barrier length is often fixed in circuits demanding high junction uniformity.

A wide range of ion species and energy is readily available using commercial broad beam ion implantation technology. In any ion damage junction process, energetic ions have a finite penetration depth where uniform damage is only created in films thinner than the ion range. Films that exceed the ion range will not be damaged near the substrate thereby leaving a

superconducting "short" in parallel with the damaged region that will dominate conduction. Therefore a maximum YBCO film thickness for high quality junctions exists for any particular choice of ion species and energy. In general higher energy and lighter ions are most desirable to fabricate uniform junctions. Both ion species and energy can be expressed in a single parameter: the ion "reduced energy" (see chapter 2). Ion range and straggle were estimated using the numerical simulation package SRIM (also see chapter 2). Focused ion beam tools are much less flexible than broad beam systems in both ion and energy, often configured for a single ion species, and converted microscope tools are typically limited to energies 30 keV or less. A 30 keV Helium source allows up to a maximum film thickness for Josephson junctions of approximately 40 nm. Thus the first choice in ion damage junction design is to pick the ion species and energy which defines an upper bound on the YBCO film thickness that can be used in circuit design.

By far the most accurate and reproducible layout variables to engineer the Josephson critical current are the barrier width and film thickness. Josephson junction critical current is proportional to the cross sectional area of the barrier i.e. is linearly dependent on the barrier width and film thickness (short junction limit). Barrier width is the easiest layout variable to lithographically control, where film thickness is initially uniform throughout the circuit at the as grown thickness. Accuracy in the barrier width is determined by the lithography choice and etching technique. Ion milling was the etch of choice in this thesis where typical minimum features achieved in our lab are as follows: photolithography~2000 nm, electron beam lithography ~15 nm, and focused helium ion beam ~1 nm. For a typical 150nm thick "electronics grade"

YBCO film, the average current density is ~100 kA/cm^2 and long junction effects are avoided for barrier widths $\leq 10\,\mu m$. Junction width also determines the Fraunhofer period of the magnetic interference pattern which in general must be much larger than the SQUID period [3][4].

Once the ion species, energy, film thickness, and bridge width have been chosen, the last remaining design parameter is the ion dose. Ion dose is typically chosen based on the dose required to reduce the Tc of a bulk film to the desired temperature. Due to the proximity effect, the dose to operate at a specific temperature must be higher for shorter length junctions compared to longer junctions. Junction Ic is exponentially dependent on the ion dose [31], hence variations in the ion dose and barrier length are typically the dominant source of critical current spread. Junction Tc is linearly dependent on ion dose for $\frac{T_C^{junction}}{T_C^{film}} \geq 0.7$ i.e. above the superconductor-to-insulator transition [31]. For doses just below the threshold dose to onset the superconductor-to-insulator transition, junction Tc is exponentially dependent on ion fluence. Due to the complex dependence of the junction Tc with ion dose, the typical design procedure involves extracting the best dose from a calibration chip containing a range of junction designs.

Additional Josephson junction design rules include placement considerations. In junction fabrication using ion masks, junctions cannot be placed closer than ~200nm from each other else they will behave as a single junction element [53]. Junctions can probably be placed closer if the damaged regions can be decoupled i.e. thinner films and shorter junctions. In general it is best practice to design junctions orientated parallel to either the YBCO a- or b-axis, where arbitrary orientations may introduce phase offsets

between junctions at different angles related to the symmetry of the order parameter. Finally, in either direct write or ion masked junctions electrode layout must be designed to dissipate charge at a suitably fast rate (on the order of the ion current) during the irradiation process else the effective junction dose will vary over the device area.

Now we will discuss the detailed fabrication processes developed for this thesis.

Wire Bonding Contact Deposition

Wafers consisting of YBCO thin films grown on sapphire substrates with an *in situ* 10nm thick Ag or Au capping layer were loaded into either a argon sputtering or thermal evaporation system. *In situ* silver is well known to create the lowest contact resistances to YBCO, where bromine conditioning etches may be required to make *ex situ* contact [54][55]. Additionally, a noble metal contact covering the superconductor throughout processing of the electrode layer patterning protects the superconducting film from contact with water, process chemicals, extraneous heat build-up, and limits deoxygenation from oxygen outgassing. A typical wire bond contact was constructed from 200-300nm thick Au or Ag films deposited on top of the in situ capping layer. Contact metal adhesion was promoted using Cr or Ti "sticking" layers between depositions i.e. at each material interface. Gold wire bond contacts are preferred due to their inert nature in oxygen plasma, thereby enabling oxygen plasma "descum" cleaning of devices after photolithographic processing. The contact metal must be deposited with high adhesion and density in order to avoid wire bond "popping".

To deposit the contact metal, DC Magnetron sputtering was performed in a Denton Discovery 18 system. The chamber was configured with 2 downward facing DC targets spaced 4 inches from the sample stage, pure Argon working gas, and rotating sample stage. Samples were loaded onto the sample stage off-center using kapton tape to ensure uniform deposition using a rotation rate of 0.5 Hz. For a typical contact deposition on Ag capped YBCO (untarnished), both Ti and Au targets were installed and sputter cleaned after a system base pressure of 2e-6 Torr was achieved. Target cleaning consists of sparking the Argon plasma for 1-2 minutes using the process settings but leaving the shutters closed. A typical DC sputter process used 200 Watts and 2.4 mTorr of Argon working gas, resulting in a rate of 0.195 nm/sec of Ti, 0.47 nm/sec Cr, 1.0 nm/sec Ag, or 0.71 nm/sec Au. Deposition rates were determined by sputtering on glass slides with a piece of kapton tape adhered, which left 2 edges after deposition and kapton peeling. The height of both edges was measured using a Dektak profilometer. To minimize contamination between the Ti and Au sputter processes, the time between depositions was made as short as possible. An average process run consisted of depositing 7 nm of Ti, and within 60 seconds initiating the subsequent deposition of 200nm of Au.

Figure 29: The custom-built thermal evaporator system constructed in collaboration with Cho and Cybart, note the high current cables for two centralized evaporation sources coming through the left and right side of the chamber. The sample is mounted onto the flange capping the top of the chamber.

Thermal evaporation was also used to deposit contact metal in a custom-built thermal evaporation system. The system was configured with 2 upward facing sources spaced 12 inches from the sample stage and a AT-cut quartz crystal microbalance sensor. Samples were attached to the sample stage using two different mechanical methods (See figure below). A combination of mechanical clips and vacuum grease were necessary, else heat from the evaporation process builds up in the center of the sample. Kapton tape was also attempted however the tape tended to sag during evaporations and thermally decoupled the samples from the stage exacerbating heat build-up. Excess heat results in film crazing (figure below right) and undesirable photoresist hard baking. For silver, a tungsten wire boat was loaded with pure silver wire wound into a ball after wiping the wire with a

tekwipe soaked in isopropol alcohol and acetone. For Ti, a solid Ti rod was loaded in place of an evaporation boat. For Au, a tungsten wire boat loaded with Au shot was installed without cleaning the shot. Before deposition, the chamber was allowed to reach a 9e-7 Torr base pressure followed by a premelting process for all boat sources. Premelting the sources enabled fast change over for serial depositions and increased reproducibility of the heating current required to reach achieve deposition rate. The deposition rate was controlled by observing the frequency change of the quartz crystal sensor (6.5 MHz) as a function of current passed through the evaporation boat, where a minimum rate of 50 Hz/sec was used to ensure a smooth morphology of the deposited films.

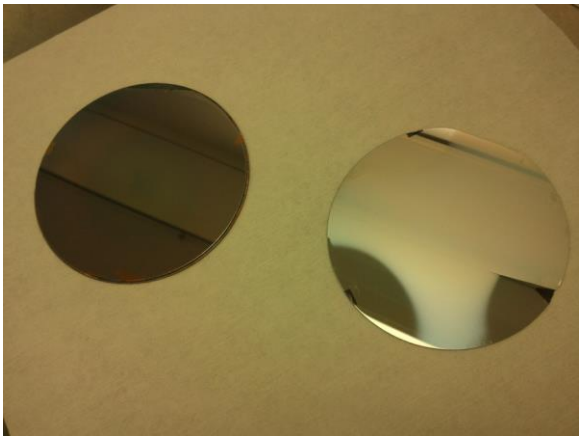

Figure 30: Two Si wafers after identical thermal evaporations of Ge on top of 1.6 microns of photoresist using an uncooled solid copper sample stage (left) Si wafer adhered with vacuum grease and 3 copper clips (right) Si wafer with attached with only 3 copper clips, clip shadows are present as dark marks on the edges centered in the shiny zones. The matte regions of the deposited metal consist of crazed and cracked Ge. Note the crack in the right side of the Si wafer, where the thermally sunk clip is on the shiny side. Clearly the crack impedes cooling confirming the crazing is the result of excess heat.

Electrode Layer Patterning with Photolithography

After deposition of the wire bonding contact layer, wafers were diced into 5mm or 10mm square chips using a Disco dicing saw with diamond blade.

Chips were cut with 45 degrees orientation to the sapphire wafer flat. To protect the samples, a layer of Shipley 1818 photoresist was applied, spun at 500 rpm for 30 sec, and allowed to air dry for 2 hrs (~2 microns). A minimum of 4 blade passes per complete cut was used to gently cut though the 0.5mm wafers. The Shipley protection layer was removed with acetone and isopropanol rinse after dicing.

After dicing, chips were spin coated with 1.2 microns of OCG 825-35cs photoresist, spun at 5000 rpm for 45 sec, and soft baked on a hotplate at 120 C for 90 sec. Thicker resist known as "edge beads" were present on all sample edges compared to the sample center. After baking, samples were exposed for 30 seconds at 11 mW/cm^2 in a JBA mask aligner (no-contact mode) using an "edge bead removal" pattern that covered the resist in the center but left 0.5mm exposed on all sides to expose the edge beads. After exposure a razor blade was then used to manually scrape the sample corners, before developing the sample in OCG 934 for 30 sec, rinsing with DI water, and drying with dry nitrogen. Removal of the edge bead enables uniform photomask contact for the critical electrode layer patterning. The samples are then reloaded into the mask aligner using a chrome-on-quartz mask for 8 sec at 11 mW/cm2. Exposed samples were then developed in OCG 934 for 35 sec while continuously stirring to ensure the resist coming off the sample did not remain near the pattern. The exact exposure and development times were adjusted for each sample run. Samples were immediately rinsed with deionized water after development, dried with dry nitrogen, and inspected under an optical microscope.

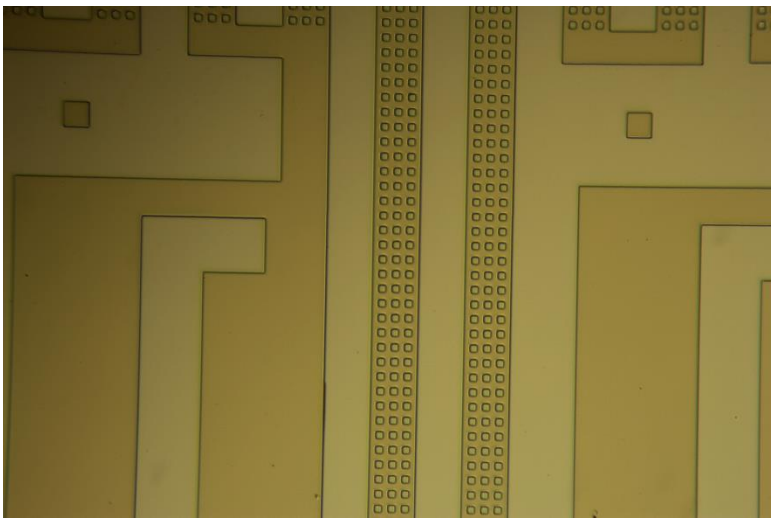

Figure 31: Optical microscope image of a SQUID array electrode pattern of photoresist after development on top of the Au contact layer. The darker regions are the patterned photoresist. The 2 alignment squares are 10 um x 10 um in size. This sample was directly loaded into an Argon ion mill to transfer the photoresist pattern into the underlying Au-YBCO film.

Argon Ion Mill Dry Etching

Argon ion Milling is typically used as a nonspecific dry etch (low selectivity but effective on all materials) to pattern thin films for which a chemically specific etch is not known. Energetic Argon ions are impinged on a material, which can create substantial physical sputtering from the material surface. Etching via ion milling is an anisotropic process, where a polymer resist mask can be used without the worry of resist undercutting that is present in isotropic wet etching. Ion milling is the preferred microfabrication method to pattern YBCO electrodes smaller than ~10 microns. A typical ion mill run removes soft metals like Au and Ag at the same rate, roughly 2.85 times faster than YBCO (a tough oxide). Wet etching of YBCO using 8% phosphoric acid (aqueous) was also used, however substantial undercutting of the photoresist mask occurred accompanied with severe undermining of the metallic

contacts. Ion milling is an energetic dry etch process that requires specialized substrate cooling procedures to mitigate thermal degradation effects.

Energetic particles impinging upon polymer materials can break down the polymer chain bonds resulting in decreased solubility and photoresist hardening. When ions strike the surface of a polymer the organic molecules break down and can outgas small atoms such as H2. The H2 can evolve from the polymer surface leaving behind involatile carbon species. Heavily irradiated resists can have a hardened carbonized surface layer that will be insoluble in typical organic solvents. Additionally, high current ion irradiation can heat the mask resulting in resist reflow. All of these contribute to the difficulty in removing resist masks especially at high ion fluences, such as after ion milling. Substrate cooling is effective at abating this situation at high currents. As long as a layer of uncarbonized resist remains at the bottom of the resist mask i.e. sufficiently thick resist, organic solvent stripping is possible. Ion hardened resists must be removed via physical polishing or etching processes such as oxygen plasma ashing.

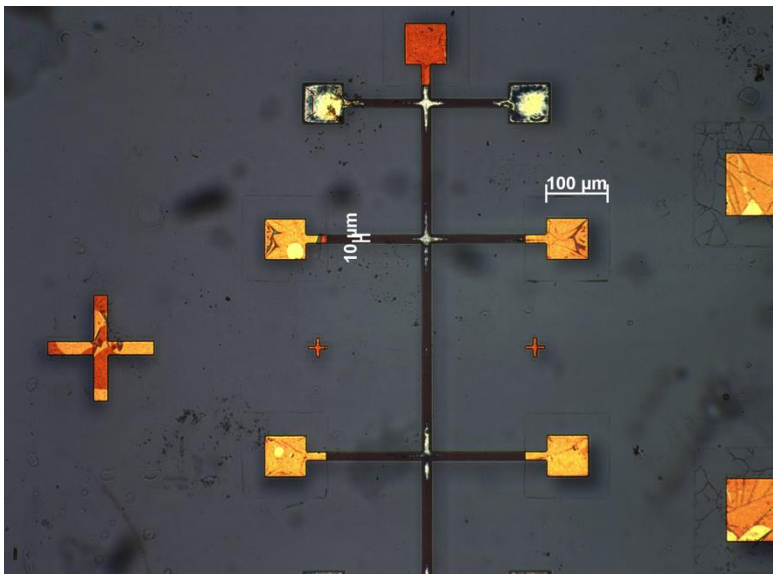

Figure 32: Ion hardened resist remains after Argon ion milling following isopropanol and acetone rinse, most evident by the dark areas on the Ag contact pads. The gray area outside of the yellow contacts and brown electrodes is exposed sapphire. The residual resist appears to form sheets that fold and wrinkle rather than lift even after heavy ultrasound cleaning in acetone. Note that this sample also underwent a short oxygen plasma etch after solvent rinse to attempt to descum the sample, where the two white/black pads near the top are tarnished silver

Standard YBCO ion milling begins with a broad beam ion source configured in our lab in the DC gridded variety. Neutral Argon working gas is introduced into the discharge chamber that is open on the opposite end, oriented towards to the sample stage. Energetic electrons generated from a heated cathode filament inside the discharge chamber strike the working gas to ionize the gas into a plasma. Some of these ions recombine with the electrons in the metal walls of the discharge chamber, others are attracted to a pair of accelerator grids located at the open end. To increase the probability of ionization, a static magnetic field is applied within the discharge chamber to further "stir" up the electrons in the discharge chamber. The accelerator grids consist of two closely spaced, convex, and perforated

molybdenum sheets with a large potential held between them; typically 500 V. These sheets allow the ionized working gas to pass through via many small holes that serve as apertures, where the holes are aligned to preferentially pass ions in one direction. Any ions that pass through the accelerator grids will gain kinetic energy in the direction of the sample stage. Therefore a slightly divergent, broad beam of ions aimed at the sample stage is created. The beam shape is maintained by neutralizing the energetic ions via an electron source positioned between the accelerator grids and the sample stage. The final neutral ion beam impinged upon the sample has an equal density of ions and electrons within the beam volume.

There are several important process engineering considerations for Argon ion milling. First consideration is the chamber pressure, which must be low enough that the mean free path of the working gas is larger than the sample to source distance. The ion beam current rapidly decreases with increased distance from the source to target due to charge exchange between the beam ions and the background gas. In other words, when the distance from the source to the target is equal to the charge exchange path length at the operating pressure only 36.8% of the beam current is incident on the target [Ion Beam Processes book]. For a 500 eV beam of Argon at a pressure of 1.7e-4 Torr, the charge exchange path length is 0.8m.

Next the discharge voltage selects the specific gas ionization, for Ar the first ionization potential is 15.8 eV, the second ionization is 27.6 eV, and the third ionization is 40.9 eV. The first ionization of Helium is 24 eV. In other words, a minimum discharge voltage of 15.8+27.6=43.4 Volts is required to produce a doubly ionized Argon beam from a single step process. In practice there can

be 5-10 volts more potential within the discharge plasma relative to the anode, and multistep processes can occur within the discharge chamber where singly ionized Argon collides with a second energetic electron both resulting in doubly ionized species being present within the beam for discharge voltages as low as 25-30 volts.

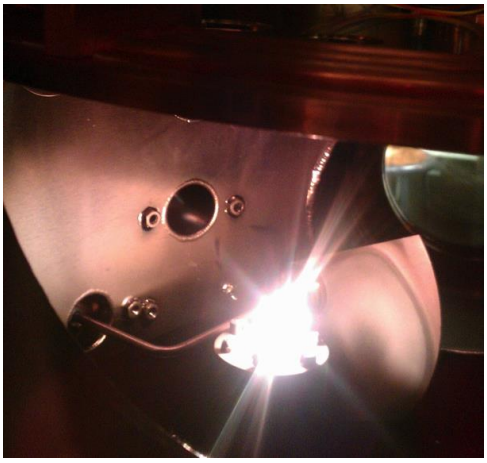

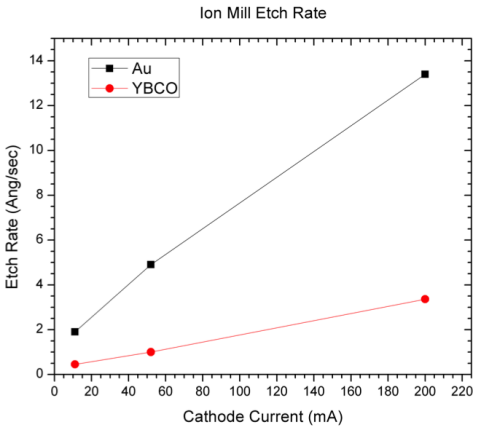

Figure 33: (left) View into ion mill chamber through a viewport during etching. 3.5 cm Kaufmann ion source with white-hot neutralizer placed over the upward facing source. Shutter is rotated behind the source in the open position, sample is loaded into the copper carousel directly above the source (top). (right) Using the typical source parameters, see text below, the usual etch rates for YBCO vs Au can be tabulated.

Early work in this thesis employed a 3.5 cm Kaufmann ion source with a liquid nitrogen cooling stage (Figure above). The neutralizer consisted of a straight tungsten wire directly over the source, heated to white-hot temperatures. A custom liquid nitrogen cooled sample stage was constructed to cool the sample, since the neutralizer heat load onto the sample during etching was very high. A typical etching procedure involved evacuating the chamber to less than 2e-6 Torr, then liquid nitrogen was pushed through the sample stage to stabilize the sample temperature. With the sample stage stabilized at 77 K, Argon was introduced into the chamber at 2.0e-4 Torr using a constant leak rate. A discharge voltage of 55.0-60.0 V, and an acceleration

voltage of 250-300 V were used ensuring double ionization effectively impinging 500-600 V Argon ions onto the sample source with a beam current density at the source of 1.04 mA/cm^2 (10 mA cathode current). On average YBCO was etched at ~3 nm/min and Au etched at ~12 nm/min. The cryogenic cooling was accompanied with active shuttering to protect the superconductor from deoxygenation and to steepen the pattern sidewalls with etch depth. Shutter protocol included a 1:1 shutter to etch time with a typical etch lasting no longer than 30 sec between shuttering. The ion milling was continued until the etched regions were no longer brown and/or contained grains. Even with great care most samples exhibited a reduced and/or a broadened Tc transition width of equal magnitude, (2-5K) presumably from thermal degradation during the etch. After etching, the resist mask was stripped with acetone and rinsed with isopropanol. While this source was effective at etching up to four 5mm samples, the etching was inhomogeneous for larger samples with approximately ~1nm/mm less etched material per distance away from the beam center up to beam diameter.

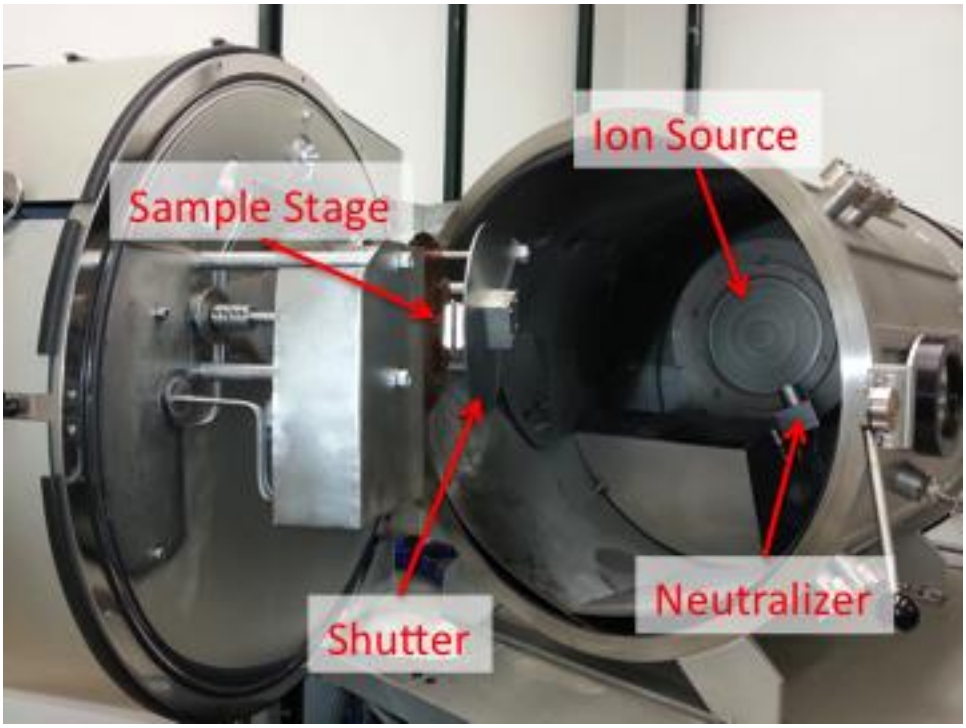

Figure 34: Ion Tech DC Argon Ion Mill (19 cm) configured with water-cooled sample stage and chamber walls

To increase the etch area and reduce the YBCO deoxygenation, we implemented a larger ion mill source with an Ion Tech system designed to reduce the sample heat load. The majority of samples were processed using this large 19 cm Kaufmann source featuring a rotating, water chilled, and adjustable angle sample stage. Stage rotation increases the etching uniformity over the whole beam area and the angle adjust enables optimization of the etch rate and sidewall angle. A shield was installed halfway through the chamber on the bottom half (see Figure above), where a downward angle of the sample stage elastically reflected the sputtered ions into the shield rather than deposit into the source (undesirable). Neutralization was performed using a plasma bridge neutralizer (PBN) aimed directly into beam at the source exit normal to the beam direction. Plasma bridge neutralizers are designed with

heat shields to isolate electron beam filaments from the main chamber thereby reducing the heat load onto the sample. A further reduction of the heat load was designed through water-cooling of the chamber walls and the ion source exterior walls. Samples were adhered to the water-cooled sample stage using Dow corning vacuum grease.

A typical ion mill process used a 50 V discharge (creating doubly ionized Argon), 500 V acceleration voltage (1000 V ions), and beam current density ~1.04 mA/cm2 (~300 mA cathode current). On average YBCO was etched at 14 nm/min and Au/Ag was etched at 40 nm/min. Using SRIM, we estimate a 1 keV Ar ion will penetrate approximately 3 nm into YBCO before stopping. In collaboration with Cybart and Cho, the conductance of a Au capped YBCO sample was measured using the Van der Pauw method during an ion mill etch (Figure below). As the sample is ion milled, the thickness decreases which reduces the sample conductance proportionally. Since the YBCO films were grown on insulating substrates (sapphire), all conduction must occur through the Au-YBCO layers. Indeed the conductance linearly decreases with etch time as the Au layer is removed. Near the Au-YBCO interface the conductance dramatically decreases due to a change in the measurement current. Once the Au layer has been removed, a linear decrease of the conductance is revived with a reduced slope corresponding to the slower YBCO removal rate compared to the soft Au metal. As the etch approaches the YBCO-Sapphire interface the conductance becomes nonlinear due to measurement error (change in excitation current).

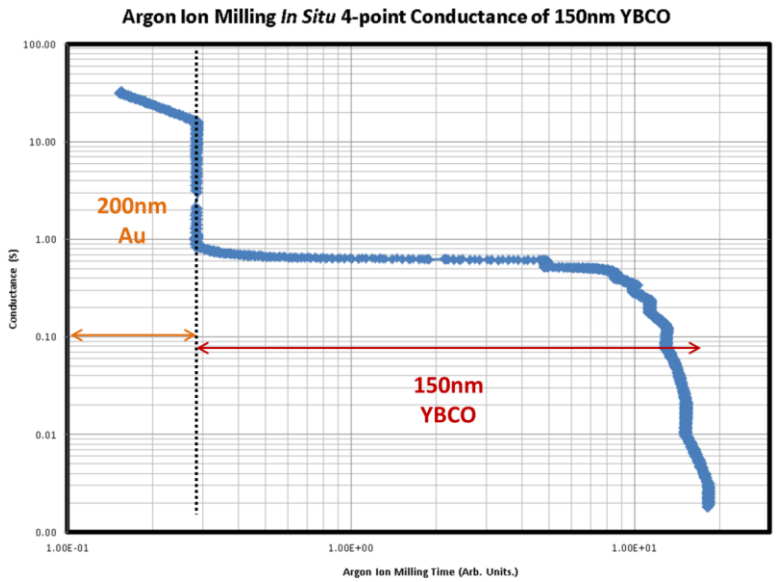

Figure 35: *In situ* conductance versus time measurement during ion milling (shuttering transients removed) of a 150 nm thick YBCO film with a 200 nm thick Au capping layer. Note the difference in conductance versus time slope for the soft metal Au versus the hard ceramic YBCO. The rapid conductance decrease at the end of the etch is due to a decreased current density, a measurement error source when the sample resistance increases beyond the current limiting resistor value.

Based on the *in situ* conductance measurements during ion milling, it is possible to reproducibly reduce the YBCO film thickness by observing the change in the room temperature sample conductance before and after ion milling. The conductance is a linear function of thickness except at the layer interfaces. Of course controlled thinning processes are only possible for samples that don't undergo significant degradation at any point in the ion milling process else the constant resistivity assumption breaks down. As well, experimentally thinned regions of YBCO are particularly sensitive to environmental degradation where the thinnest samples were found to be unstable in ambient conditions.

Gold Removal Patterning

The Au must be removed over the junction areas else the irradiation will be stopped in the high atomic density *in situ* capping layer. The high Z capping layer is effectively an ion mask. A second photolithography step was performed with an identical spin, exposure, and development process compared to the electrode layer. The "Gold Removal" pattern consisted of openings in all junction areas with resist covering the remainder of the circuit. Samples were then immersed in a Transcene Gold Etchant, consisting of potassium iodide in saturated iodine ($KI\&I_2$). The concentrated Gold etchant removes 200nm of Au in approximately 40 seconds and 200nm of Ag in 10 seconds before a deionized water rinse was used to stop the etch. Transcene Gold Etchant does not remove the sticking layer materials (Ti or Cr). Ion milling was also used to remove the Au-Ti layer together, which exposed a cleaner YBCO film than the wet etch albeit requiring a few hours more processing time and greater process complexity. A typical height profile after resist stripping is measured using a Dektak Profilometer to verify the depth of the ion mill etch and the completeness of the Au removal process (Figure below)

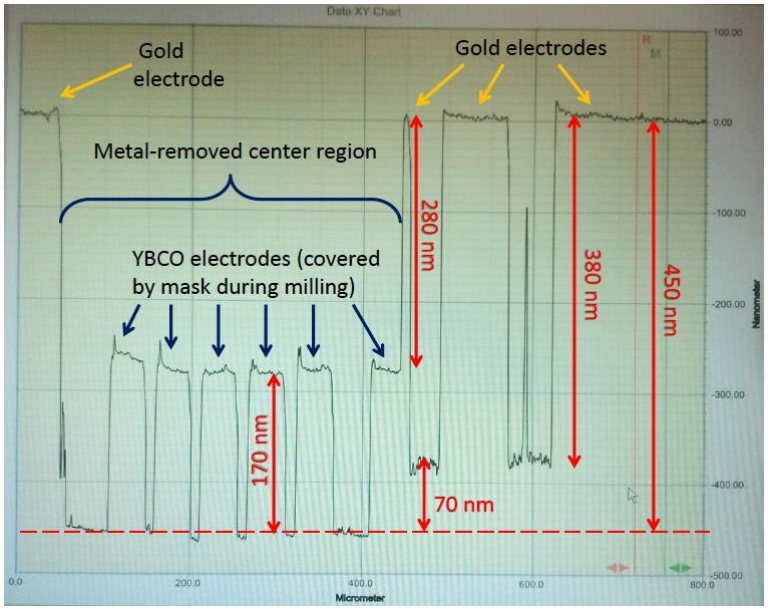

Figure 36: Dektak profilometry of a 6 YBCO bridge sample after ion milling and gold removal

Care must be taken to avoid damaging the alignment marks during Au etching, as all alignment marks are patterned with an exposed Au surface. If an alignment mark in the Gold Removal layer is patterned exactly the same size as the electrode layer, then the Au on the alignment mark will distorted by the inevitable misalignment between the Gold Removal pattern and the Electrode pattern. Generally an minimum of 5 microns must be added on all sides of an alignment mark to ensure that a combination of pattern misalignment and wet etch undercutting will not distort the Au layer. Precision alignment marks with Au capping are particularly important for alignment in electron beam lithography.

Mask for Ion Damage Josephson Junction Patterning Via Implant

In this thesis two different junction patterning techniques were used: direct write and implant mask. Direct write junctions were all written by Ethan Cho and Shane Cybart using a focused helium ion beam (See E. Cho Thesis

and [47]). In this thesis I will only describe the implant mask process, in which a similar process has been described in detail both Cybart's and Katz's theses previously. The full trilayer material system was designed to use electron beam lithography (EBL) to pattern < $80\ nm$ wide canyons into a 900 nm thick layer of photoresist. The photoresist thickness is chosen based on SRIM range calculations to stop 175 keV Ne ions thereby protecting the underlying YBCO from irradiation except in the junction regions (See Figure Below). We remark that previous ion masks were made as thin as 800 nm, where performance Josephson junctions were fabricated despite the implantation of Ne into the top 10-20 nm of the YBCO film under the mask.

Very small pattern dimensions are necessary for Josephson junctions ($\leq 80\ nm$) and are achievable using electron beam lithography. However patterns on the order of 10nm cannot be directly written into a very thick resist i.e. resist contrast limited to approximately 1:3 aspect ratio of the pattern size to the resist thickness. High weight (950 amu) PMMA is the positive resist of choice for fine feature and high contrast EBL, where the optimal PMMA thickness for fine feature patterning is between 50-100 nm. In principle an oxygen reactive ion etch (RIE) can be used to transfer the EBL pattern into the thick photoresist underlying the PMMA. The most obvious difficulty in using a RIE process to transfer a PMMA pattern into a thick photoresist layer is the lack of an etch process with sufficiently high specificity between the polymers using oxygen; PMMA has a low oxygen etch resistance. A particularly high etch selectivity towards photoresist compared to PMMA would be required because of the 10:1 thickness ratio. An RIE etch of sufficient performance is not currently known, so an intermediate etch stop layer is used. In this case a layer

of Ge is used as an etch stop towards oxygen plasma. Thermally evaporated Ge easily wets most surfaces and hence easily grows smooth, thin films of uniform thickness without pinholes. A wide range of reactive ion etch processes are also available for Ge. In order to transfer the EBL junction pattern into the Ge layer using a RIE process, a slightly thicker PMMA layer (120 nm) must be used for high fidelity. The complex material system making up the trilayer implant mask is captured in the Figure below.

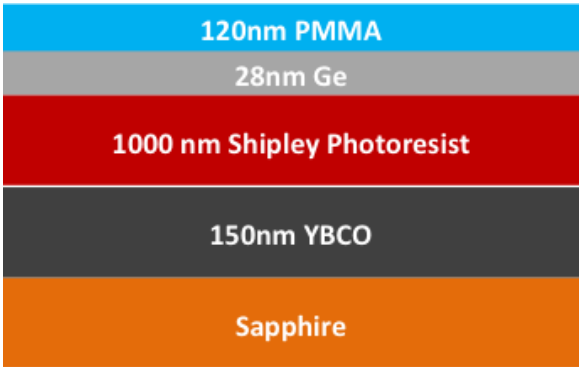

Figure 37: Typical trilayer resist stack constructed on top of YBCO thin film

The mask is constructed by first spin coating the patterned YBCO circuit with Shipley S1813 at 7000 rpm for 45 sec followed by a hard bake on a 130 C hotplate for 6 hrs. Residual resist on the backside of the samples must be removed with an acetone wipe before hard baking, else extra nonuniformity in the EBL pattern will result (defocusing within a write field). Samples were then loaded into the custom built thermal evaporator using Dow Corning vacuum grease, and 28 nm of Ge was evaporated corresponding to a 1800 Hz change of the quartz crystal sensor installed just above the sample. Ge must be deposited at a significant rate ~1-2 nm/sec to ensure the smoothest film morphology and the least amount of sample heating. Excessive sample heating will cause the resist to reflow and bubble thereby cracking the Ge layer. Typical quartz crystal microbalance frequencies change by 100-200

Hz/sec to achieve the 1-2 nm/sec rate of deposition. Finally poly(methyl methacrylate) 2% in chlorobenzene (950k PMMA-C2) was spin coated at 2000 rpm for 45 sec, short baked at 105 C for 2min on a hotplate, followed by a 3hr convection oven bake at 107 C. If the PMMA bake were performed at temperatures approaching the hard bake temperature (130 C), then the photoresist layer would contract and/or evolve volatile solvents thereby cracking and crazing the Ge layer. Such a low PMMA bake temperature is nearly equal to the PMMA glass transition temperature (120 C), where bake temperatures below 170 C will not remove the inherent polymer strain decreasing contrast. The key properties of the Shipley photoresist include exceptionally low reflow and contraction properties below the hard bake temperature, which enable the extended, low temperature convection oven bake required to fully remove the chlorobenzene from the PMMA layer. Insufficient removal of solvent from the PMMA film will result in decreased contrast and significant variation in the electron threshold dose.

The use of a hotplate necessarily transfers heat into the sample from the substrate side, meaning a thermal gradient exists throughout the sample from the backside contacting the hotplate up to the top surface exposed to ambient air. Hence the use of a hotplate with a thick multilayer resist stack will heat the underlying layers more than the surface layers inducing strain that can also crack and craze the Ge. Convection oven baking uniformly heats the sample from all directions, and thus is a less aggressive bake that is well-suited to soft trilayer masks. Any breaks in the Ge etch stop layer can be catastrophic as all holes in the Ge will transfer into the underlying photoresist

during the final RIE process. These holes will then permit ions to pass through the mask resulting in YBCO damage outside the junction regions.

Later generation trilayer masks were also coated with an 8 nm thick layer of silver on top of the PMMA via thermal evaporation before electron exposure. This thin layer of silver dissipated charge from the exposed areas and was removed before development by a 10 sec dip in Gold Etchant ($KI\&I_2$) followed by a deionized water rinse. The extra conduction layer enabled dramatic improvements to microscope beam optimization times and increased pattern uniformity.

Electron Beam Lithography of Junction Regions

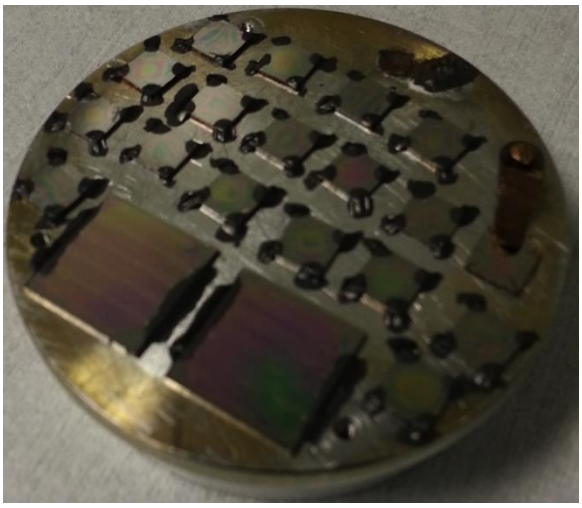

Figure 38: Scanning electron microscope stage loaded with YBCO samples coated with trilayer masks just before electron exposure. Each sample is individually grounded using conductive carbon paint to the Al stage. The stage is precision leveled and all sample backsides are cleaned to maintain the stage level.

High molecular weight PMMA is chosen as a positive resist for electron beam lithography (EBL) to due the very long polymer chains, which can be cut by high-energy electrons. Electron scission of the polymer chains results in regions of shorter chains which are more soluble in PMMA developer than the

undamaged long chains. The dose of electrons required to make PMMA soluble in developer is called the threshold dose of the resist. A typical high aspect ratio PMMA developer consists of methyl-isobutyl-keytone (MIBK) diluted with isopropyl alcohol (IPA) in a 1:3 ratio. Electron damage of the resist primarily occurs from the large number of secondary electrons ejected from the higher Z materials underneath the PMMA rather than the primary electrons themselves. Thus every electron beam lithography pattern and resist stack configuration must be tested with a series of electron doses and development processes to determine the unique configuration for each pattern. A typical threshold dose for a ~30nm wide PMMA line in a standard trilayer stack on YBCO is ~1.75 nC/cm, using a 30 keV electron beam, and 80 second agitated development in 1:3 MIBK:IPA (Figure Below). Chilled development was also attempted, where -16 C 1:3 MIBK:IPA did result in higher pattern contrast due to increased solubility contrast between short and long PMMA polymers in developer. The cold development was slower than room temperature development where the time was increased by ~10 sec and electron dose increased by ~10% to achieve threshold PMMA clearance in ~15-20nm lines.

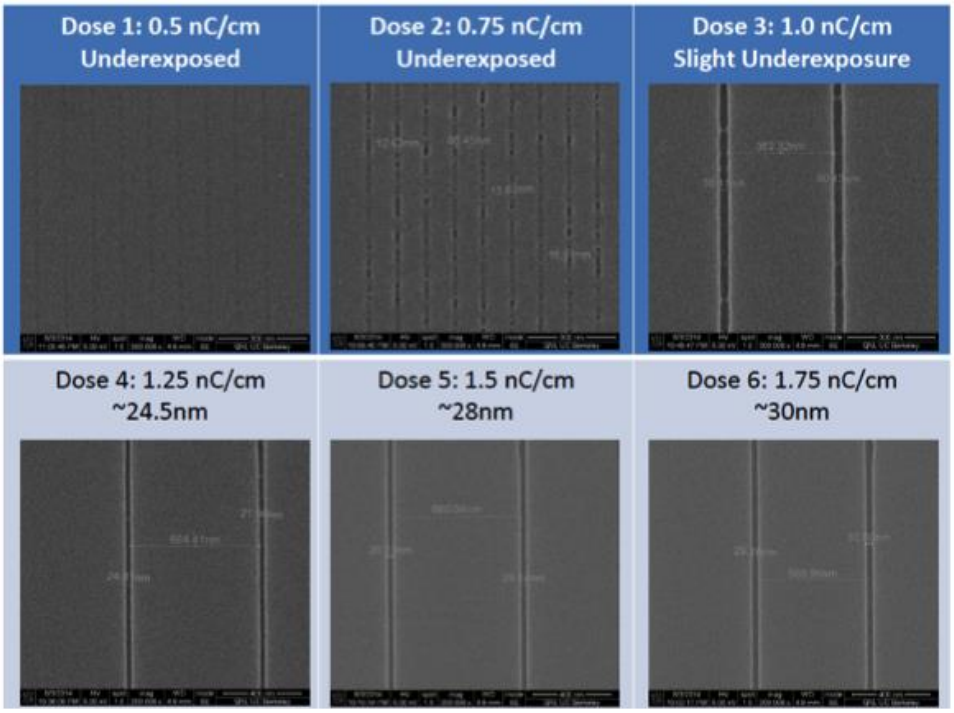

Figure 39: Top-down scanning electron microscope (SEM) imaging of a range of single pixel line patterns after exposure and development in the top PMMA layer of a trilayer constructed on YBCO before RIE. A 30 keV electron beam was used to exposure the patterns.

For this thesis, standard scanning electron microscopes (FEI SEMs) were equipped with Nanometer Pattern Generation System (NPGS) to take control of the beam to perform electron beam lithography (EBL). The junction areas cannot be viewed for alignment or focusing procedures. Each beam current (aperture) and beam energy (acceleration) will change the beam position (shift and tilt) as well as the spot geometry (focus and stigmatism). The smallest microscope aperture was selected to minimize the beam current, on average 30 pA at 30 keV. A 30 keV beam was used to uniformly penetrate the PMMA film with electrons and because the smallest beam spot size was available at the highest voltage setting. The microscope zoom was set to 3200x creating a 1.37 nm point-to-point spacing in both the in plane directions (approximate beam diameter ~13 nm). Generally we attempted the largest write field

possible while maintaining a ~50% overlap between beam spots at adjacent pattern points, where the point-to-point spacing is limited by the hardware DAQ and the magnification. A 10 mm working distance was set to optimize the depth of field i.e. sample area with a uniform beam spot size.

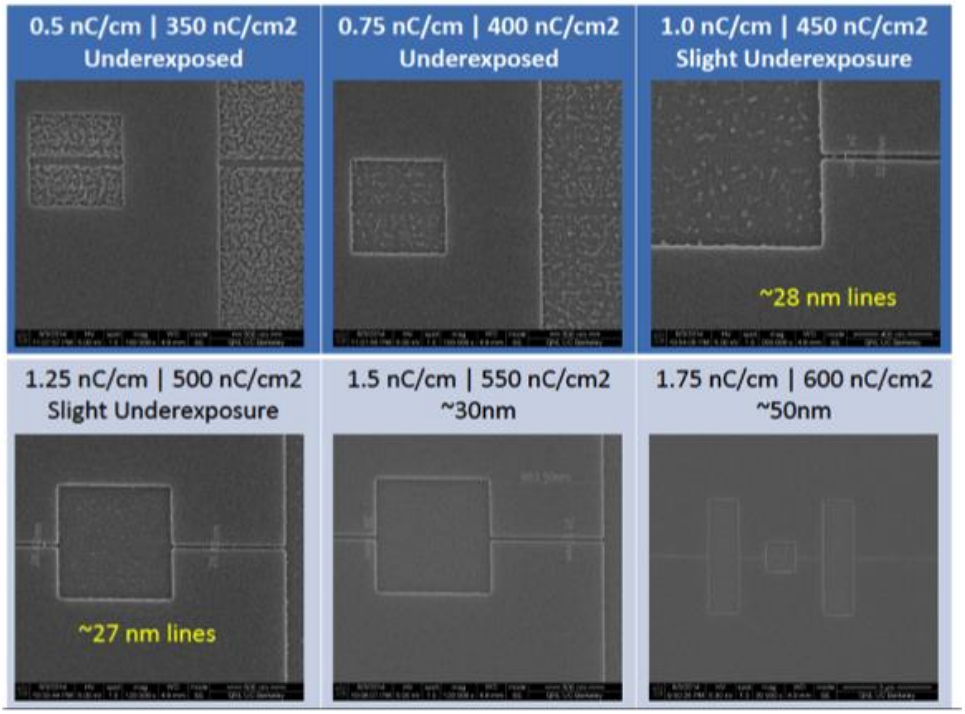

Figure 40: Top-down scanning electron microscope (SEM) imaging of six different area and single pixel line doses after exposure and development in the top PMMA layer of a trilayer constructed on YBCO before RIE. A 30 keV electron beam was used to exposure the patterns. Note that area doses below the threshold of 550 nC/cm2 do not completely clear the PMMA and residual resist contamination remains after development.

Samples were mounted to a precision-leveled specimen holder using a sparing amount of colloidal carbon paint on all corners to ground the sample to the stage. The carbon paint was preferred over silver paint since it can be removed with isopropanol before development, whereas silver paint requires solvents such as acetone that would catastrophically attack the trilayer. All samples were manually scratched with a tweezer on the corners to clear the trilayer and ensure low resistance electrical continuity from the carbon paint to the YBCO circuit electrodes. Careful grounding of the circuit to the sample stage is required to eliminate charge build-up during writing due to the insulating sapphire substrate. The mounted samples were loaded into the SEM and the 30 keV beam was turned on after the chamber vacuum dropped

below 2e-6 Torr. Detailed narratives of the EBL process has been described by Cybart [56]. Great care was taken not to image any of the trilayer regions to be patterned during pattern alignment, including moving the stage manually along specially designed guide marks within the electrode pattern, and "blind" stage moves where the beam was blanked as the sample was navigated into each write field. For manual writing typical alignment marks consisted of at least 2 diagonal marks within each write field for EBL performed on tools without a laser interferometer stage. The beam must be focused near each write field to achieve the smallest spot size as required for fine lines. Beam focusing is performed by "burning" a contamination dot in "point" beam mode at the highest magnification followed by normal scanning mode imaging where the focus and astigmatism are adjusted to optimize the image. This technique only works in vacuum systems where organic contaminants are present, where the electron beam assisted deposition of carbon creates the contamination dot. The electron beam assisted deposition of carbon creates a dot in the same shape as the beam impinged on the sample surface. A different procedure is used with tools configured with laser interferometer stages and on the fly, software controlled beam adjustments. Focusing and stigmatism adjustment is performed around the outside of the pattern area focusing on Au and polystyrene nanoparticles. Multiple points are acquired around the sample and input into a numerical compensation algorithm designed to automatically adjust the focus and stigmatism over the whole sample area.

For EBL performed on Vistek tools with a precision laser interferometer stage, multiple 10 um x 10 um squares were positioned around the whole

pattern area with no other electrode element within a 100um of the square. The square shape is picked up using automatic pattern recognition software to set the global coordinates for pattern writing with a laser stage. For manual tools like the FEI microscope, 5-10 um stubs were added to the electrodes around each write field that were electrically connected to the circuit permitting enhanced charge dissipation. Alignment marks must have high electron contrast relative to adjacent structures. In the case of high energy beam (100 keV), very few secondary electrons are produced even from high Z materials making alignment mark design even more important. Gold-capped alignment marks are effective on both sapphire and YBCO substrates.

Reactive Ion Etch of Trilayer Implant Mask

Reactive ion etching (RIE) is a vacuum process that uses both chemical and physical sputtering etching processes to anisotropically etch many materials. A plasma discharge is created by capacitively coupling radiofrequency (RF) energy into a working gas mixture at low pressure. The RF excitation (13.56 MHz) is generated from a parallel plate capacitor oriented along the axis of a cylindrical vacuum space (chamber walls are grounded). The sample is placed on the anode or "target surface" which is isolated from ground. The plasma tends to be slightly positive, i.e. higher concentration of ions than free electrons, as the electrons are partially collected on the electrically floating anode thereby creating a DC voltage that creates a static electric field in addition to the RF field between the parallel plates. The net negative charge of the anode attracts the positive ions from the plasma imparting kinetic energy perpendicular to the anode surface. This kinetic

energy is necessary to produce anisotropic physical etching. In this way the RIE reactor is configured such that the ionized working gas species are accelerated towards the target where they attack and react with the target surface. Higher acceleration (higher DC voltage) increases the ion energy thereby increasing the etch anisotropy and physical sputtering effects. The accelerated ions can strike the target atoms with sufficient kinetic energy to induce physical sputtering, a low chemical specificity process. Chemical etching is also possible when the plasma ions react with the target atoms (high chemical specificity) to form volatile gas molecules which are actively pumped away from the discharge chamber. Any chemical reactions that produce nonvolatile species will not etch the target but rather will chemically modify the target surface. Careful choice of working gas chemistry and plasma mode can be used to increase etch selectively between species in a target sample.

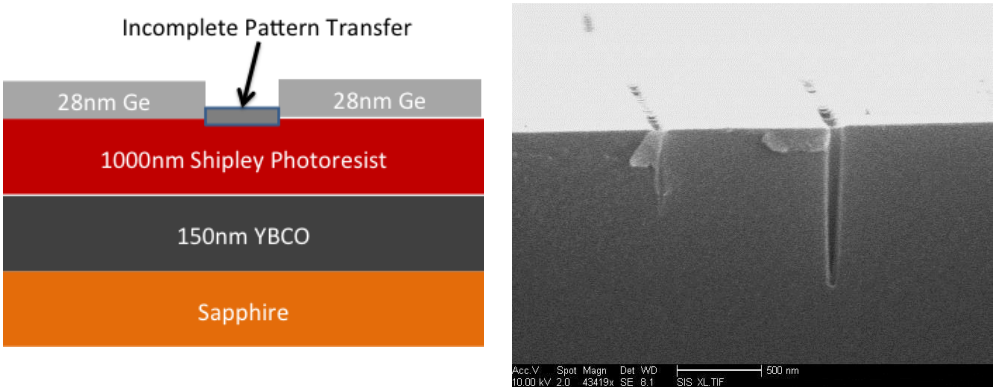

Figure 41: (left) Cartoon of incomplete line transfer from the PMMA layer into the Ge etch stop. (right) SEM image at a overhead glancing angle of a trilayer cross section after final RIE processing, where the bright top is the Ge layer and the darker bottom is the Shipley photoresist. Note canyons are incomplete due to a failed Ge pattern transfer.

Two different RIE processes are performed in series to fabricate the junction implant mask: First a C-Cl2-F2 (Freon12) etch to transfer the PMMA

pattern into the Ge etch stop, followed by a low pressure oxygen etch to transfer the Ge pattern into the thick bottom layer of photoresist. The Ge etch requires both an anisotropic etch and moderate chemical specificity between PMMA and Ge. The etch must be anisotropic to avoid broadening of the junction lines. Moderate chemical specificity is required in that the PMMA resist must remain long enough to transfer the EBL pattern into the Ge etch stop. Hence it is highly desirable that the Ge layer be thinner than the PMMA layer, but thick enough to remain throughout the long oxygen etch to pattern transfer into the underlying photoresist. The acceptable process latitude is quite small to achieve canyons with vertical walls narrower than 50nm (20:1 aspect ratio). Residual PMMA remaining at the bottom of the junction lines after EBL development, too thick of Ge, or too thin of PMMA will result in a failed pattern transfer to the etch stop layer. The RIE processing of the trilayer is the most challenging aspect of the ion damage junction fabrication process due to the narrow range of acceptable parameters to achieve the canyon critical dimensions.

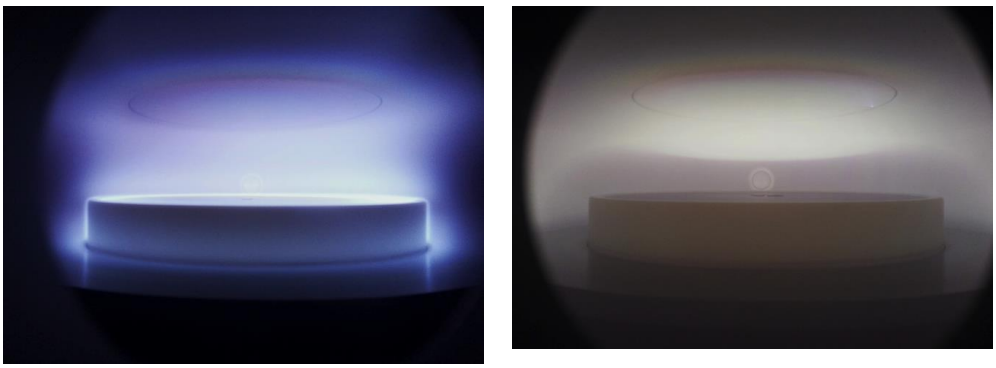

Figure 42: Side window view of Reactive Ion Etch plasma modes in the optimized state, note the samples in the center of the anode. (TRION Phantom III) (left) C-Cl2-F2 plasma with RFpower= 25 Watts, pressure= 130 mTorr, gas flow= 50 sccm, DCbias= 0V. (right) Oxygen plasma with RFpower= 48 Watts, pressure=1.0 mTorr, gas flow = 7 sccm, DCbias= -30V. Note the ~1.25" tall plasma "dark space" where ballistic gas flow occurs.

To investigate the parameter space of the PMMA pattern transfer into Ge etch stop, bulk samples of PMMA and Ge were etched simultaneously for a range of RF power and process pressures (Figure Below). The gas flow rate was fixed at 50 sccm of Freon12 and all samples were etched for 5 minutes. Freon12 (C-Cl2-F2) working gas was used instead of pure chlorine or fluorine to enhance the chemical specificity towards Ge instead of the PMMA polymer, in addition to being much safer to handle than pure Cl_2 and F_2. PMMA and Ge films were deposited to 1 cm Si chips such that only half of the Si sample area was covered thereby enabling Dektak profilometry of the step from the Si to the Ge/PMMA film surface. Control samples were used where Ge was deposited on top of a layer of PMMA where the Ge on PMMA step height was compared to the Ge on Si and PMMA on Si steps. Clearly higher pressure and lower power processes have the largest etch selectivity between Ge and PMMA (Figure below). This result makes sense, as higher pressures increase the concentration of ionized reactants available at the target, higher pressures decrease the mean free path at the target surface, and lower RF power decreases the DC bias i.e. ion acceleration thus minimizing physical sputtering.

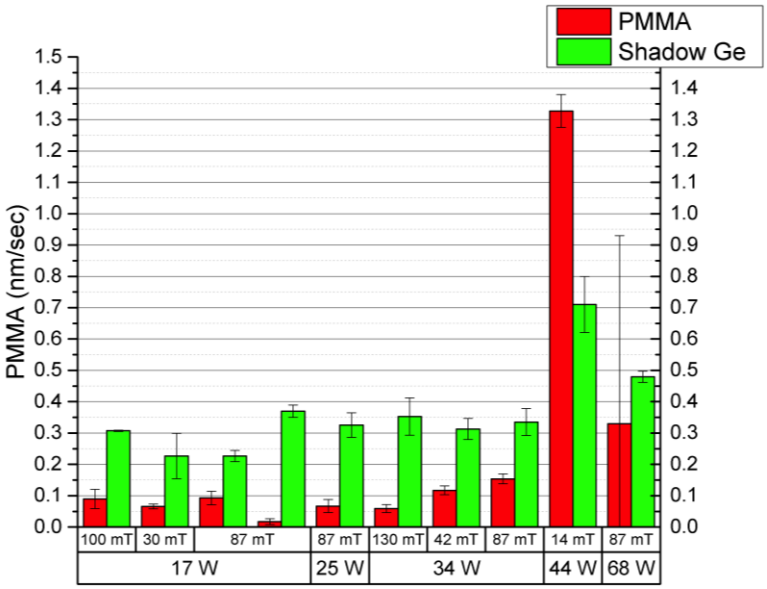

Figure 43: Comparison of the etch rate of thermally evaporated Ge to 950k PMMA for a range of RIE processes using C-Cl2-F2 (Freon12) working gas.

Oxygen RIE of the hard baked Shipley photoresist requires specialized processing techniques. The optimal oxygen RIE is performed at approximately 1 mTorr with 48 Watts of RF power to generate approximately 1 inch of "dark space" above the target. The height of the dark space was the critical process parameter to maintain run-to-run reproducibility for the creation of vertical canyon walls. A plasma dark space indicates ballistic ion transport, where light emitted from plasmas are primarily due to diffusive collisions between plasma species emitting light. A ballistic dark space enables large ion accelerations with high directivity, both of which are required to achieve the very high etch anisotropy (~50 nm wide lines in 1000 nm of photoresist).

It is essential to clean and precondition the RIE reactor prior to etching, or contamination of the working gas occurs introducing competing side reactions. The oxygen etch is particularly sensitive to reactor contamination due to the low process pressure where only a small number of reactant ions are impinged on the target. The concentration of reactant ions penetrating

the canyons is sensitive to the canyon width, where the mean free path within the canyons is primarily determined by the canyon width (see Figure below). As the etch evolves with time the volatile species reacted from the sample contribute to the working plasma, as is evident from a color change from an early etch "blue-white" spectrum of pure oxygen to a "white-green" spectrum. Any other plasma colors during the oxygen etch are indicative of contamination, where a vacuum leak (say pink hues from a leak in the nitrogen vent valve) will change the gas chemistry resulting in etch failure.

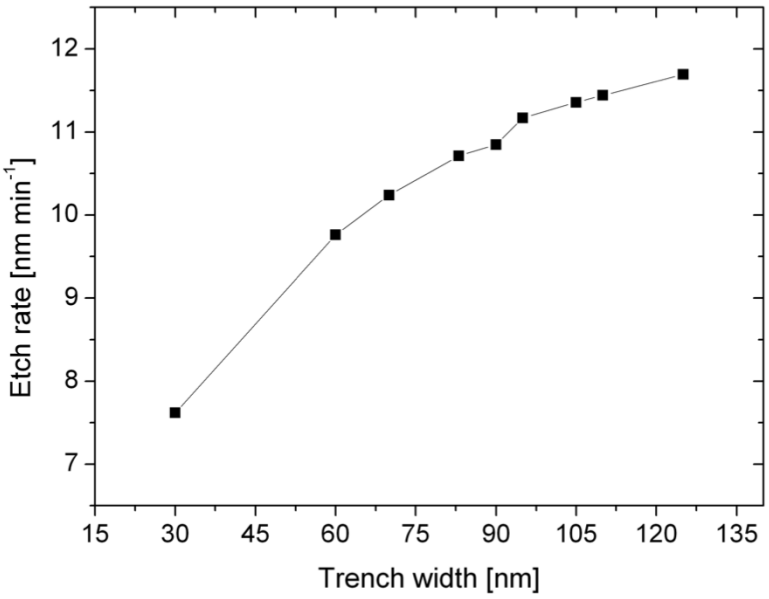

Figure 44: Oxygen RIE rate versus canyon width, note the gradual decrease in etch rate for the smallest canyon widths (trench width). Experiment performed in collaboration with P. Roediger.

The majority of RIE processing was performed using a Trion Phantom III system. The Ge and canyon etches were performed in series without breaking vacuum. Before samples were loaded, the reactor was preconditioned with 600 seconds of $C\,Cl_2\,F_2$ etch: 130 mTorr pressure, 50 sccm gas flow, and 25 Watts of RF power (identical process for Ge etch). When the preconditioning etch was omitted, the process pressure of the canyon etch required spot

tuning for every process run to obtain the specified dark space height. Since the $C\ Cl_2\ F_2$ Ge etch must precede the oxygen process without breaking vacuum, the reactor must be conditioned to always present the same starting state for the oxygen etch to decrease the run-to-run variance. In particular, each cycle of the RF excitation accelerates the plasma ions up and down between the capacitor plates, with ions occasionally striking both the chamber walls and the target surface. Hence contamination on the chamber walls and deposition of ions onto the chamber surfaces both occur during RIE processing. Since the chamber walls cannot be removed from the process, preconditioning the reactor walls with the Ge etch ensures the most consistent gas chemistry for the oxygen etch.

Now I will describe the typical process protocol. Firstly the chamber was preconditioned as stated above. Secondly a brief canyon "test etch" was performed to verify the plasma stability before samples were loaded. To perform the canyon etch 7 sccm of oxygen was introduced into the chamber and a butterfly value was manually adjusted to set a 1 mTorr pressure. Our RIE was unable to spark the working gas into plasma at the process conditions. To spark the plasma, the oxygen flow was turned up until the chamber pressure increased to ~20 mTorr (~20-30 sccm). Then 48 W RF power was applied "sparking" the plasma, after which the oxygen flow was immediately dropped down to the initial 7 sccm restoring the desired process condition. Once the plasma stabilized the butterfly valve was finely adjusted to achieve a 1" dark space and the new chamber pressure was noted. The "test etch" should last no longer than 1-2 minutes.

The process was then stopped, the chamber vented using dry nitrogen, and samples were quickly loaded using Dow Corning vacuum grease (301) slightly off-center on the target stage. The chamber was then evacuated and chilled water applied to the sample stage to minimize sample heating during RIE processing. The loaded reactor was turbo-pumped until a 1.1e-4 Torr base pressure was achieved (at least 30 min). The Ge etch was then performed for 97 sec using 130 mTorr of $C\ Cl_2\ F_2$, 50 sccm gas flow, and 25 Watts of RF power. After Ge etch completion, the reactor was then pumped to a base pressure of ~9e-5 Torr with the cooling water remaining on for a minimum pump time of 2 hrs (to completely clear the $C\ Cl_2\ F_2$ gas and etch products). Finally, the canyon etch was performed in exactly the same manner as the test etch for 1200 seconds (~90-100 nm/sec etch rate). Once the canyon etch was complete the chamber was pumped for 5 min, after which the cooling water was stopped and the samples were allowed to return to room temperature in a static 200 mTorr oxygen environment (typically 1 hr to avoid water condensing on the samples). After the samples were removed, the reactor was cleaned with a oxygen etch for 2000 seconds with 200 Watts RF power, 100 mTorr pressure, and 50 sccm flow (no water cooling). To verify the completeness of the RIE etch and the canyon critical dimensions, the Si calibration sample run in parallel is cleaved to expose the cross section of the implant mask (Figure below). If the RIE etch was satisfactory, then the canyon width was inspected using top-down SEM imaging for all samples. A specific ion dose was then calculated based on the average canyon width (see first discussion in this chapter).

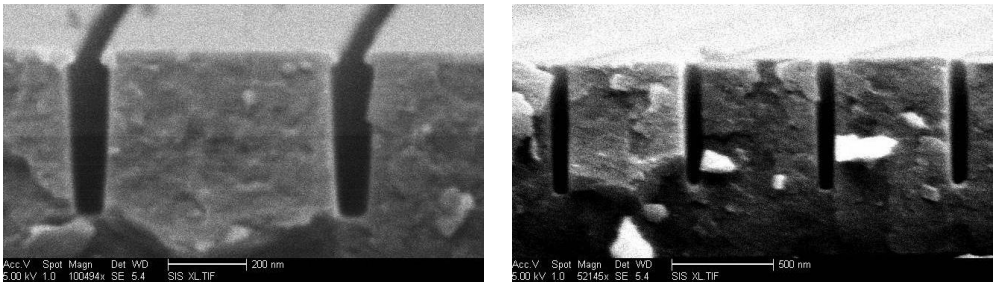

Figure 45: Scanning electron microscope images of the trilayer cross-section after processing. Note the images are taken from a glancing angle slightly above the top of the mask. (left) Failed RIE etch where the initial 50nm PMMA lines are broadened, Ge etch stop is severely undercut, and the canyon sidewalls are sloped. (right) Example of a successful RIE etch with high fidelity pattern transfer, no etch stop undercutting, and vertical canyon walls.

Ion Implantation of Patterned Trilayer Samples

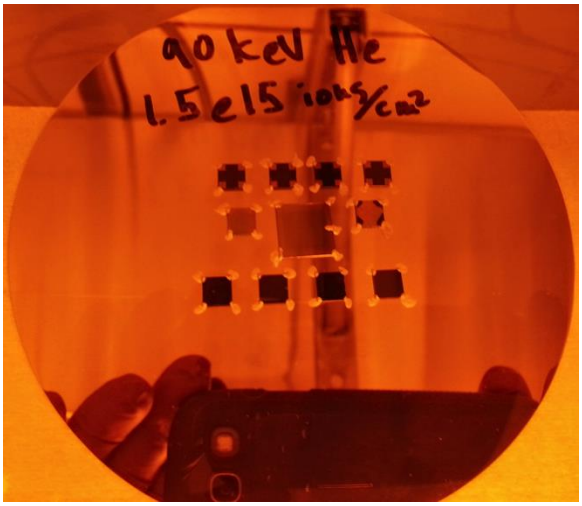

Figure 46: Samples ready for implant, loaded onto a Au coated Si carrier wafer using silver paint

To create the ion damage Josephson junctions, the patterned trilayer samples were bombarded with ion irradiation. Before irradiation, all samples were loaded onto a Au or Ag coated Si carrier (P+ doping) wafer using highly conductive colloidal silver paint. The carrier wafer was then loaded into a thermal evaporator at a slight angle (~10 degrees) to the evaporation source where 7nm of Au was flashed onto all samples. The thin layer of Au combined with the silver paint in contact with the carrier wafer ensures a low resistance

charge dissipation path during the ion implantation process. Without these charge dissipation procedures, the trilayer will charge up during implantation thereby screening some of the ions away from the junction regions. The carrier wafer was then implanted with either 90 keV of He_4^+ or 175 keV Ne_{20}^+ at normal incidence to minimize run-to-run variation i.e. assuming negligible channeling effects. Implantation was performed using an electrostatically scanned ion beam over the carrier wafer area. After ion implantation the trilayer mask becomes ion hardened and is sometimes difficult to remove. A typical stripping process involves a 5 min soak in acetone with ultrasonic agitation, where a thin layer of hardened resist typically remains but is thin enough for wire bonding. Aggressive stripping of the trilayer mask is not required for sample characterization, and complete removal of the hardened resist often results in degradation of circuit performance.

Sample Characterization Techniques

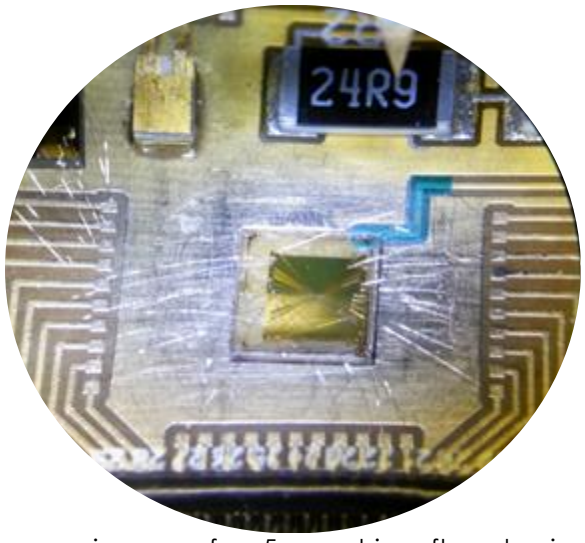

Figure 47: Microscope image of a 5mm chip after aluminum wire bonding ready for transport measurements. Note the Lakeshore DT-670 Si diode thermometer (top left), surface mount resistor heater (top right), YBCO sample (center), and wire bond compatible signal launches (printed circuit board wires on left, right, and bottom of sample). A wire wound magnet is pressed against the back of the sample stage providing magnetic fields perpendicular to the plane of the sample (not shown).

To characterize the transport properties of the YBCO circuits a variety of custom cryogenic dip probes were built. Each "dip" probe was designed to mount either a printed circuit board or chip carrier containing the YBCO sample in a vacuum "cold space" that can be immersed in liquid cryogen. Printed circuit boards were designed with many vias connecting the ground planes on the top and bottom of the board for thermal cooling. The cold space was designed to incorporate a BaSrCaCuO superconducting shield surrounding the sample stage. Samples were mounted using a sparing amount of epoxy in close proximity to a Lakeshore DT-670 Si diode thermometer, resistive heater, and wire wound magnet (Figure above). Thermally decoupling the sample from the cryogenic bath via a vacuum space enables control of the sample temperature using the heater and thermometer

elements. Cooling was performed using either direct immersion into a liquid bath or convective cooling by lowering the dip probe into the vapor directly above a cryogenic bath. Sealing the dip probe into a vacuum tight cryostat and regulating the pressure above the cryogen effectively controls the temperature. Liquid nitrogen baths can be modulated from 77 K to 48 K by "pumping" out the vapor space from ambient pressure (77 K) down to approximately 200 mTorr (48 K). All probes configured with BSCCO superconducting shields were initially cooled in liquid nitrogen inside a triple layer mu-metal shield to minimize Earth's field reaching the sample to less than 10 uT.

Samples were electrically connected with 75 um diameter Al-Si wire using ultrasonic wedge wire bonding at room temperature. Samples were connected using 4-point probes consisting of differential signals isolated from ground. All DC leads were fed from room temperature to the sample using twisted pairs of fine copper or manganin wire. Tightly twisted wire pairs are well known to mitigate 60 Hz noise for differential measurements. Heater and thermometer lines were separated from the sample lines to further minimize electrical noise at the sample. All electrical connections fed into the cold space must be "thermalized" or cooled to the bath temperature before reaching the sample stage. Cooling of the electrical leads to the bath temperature ensures that the Johnson noise injected into the sample match the bath temperature. Samples were tightly coupled to copper cold fingers in the cold space where the cooling power from the external bath is throttled by the effective thermal resistance of the cold finger to the external bath. Additionally, helium exchange gas (10-1000 mT) was back filled into the

vacuum space to further thermalize the cold space and the sample. A custom low pass RC Pi-filter was installed on all twisted pairs between the sample and the warm electronics to attenuate instrument noise (RC knee at 30 kHz). Silver paint was applied to the twisted pairs in the cold space to attenuate some radio frequency noise from the warm electronics (RF powder filter).

The entire experimental configuration was contained within an RF shielded room including the cryostat and warm electronics. All DC leads were connected to warm electronics through a custom-built "break-out box", where each lead was connected to the center-pin of a BNC connector on the "break-out box". A single point ground configuration was used where all instruments and cryostat were connected to the break-out box chassis, which was connected to the wall of the shielded room. All line power was fed through isolation transformers into the shielded room, where line power can be disconnected from the room as needed. Low-noise SR560 preamplifiers ($3\ nV/\sqrt{Hz}$ at 50,000 gain) powered with shielded lead-acid batteries where used to amplify the low level differential signals. Digital data acquisition was performed using custom Labview software interfaced with the National Instruments NI-9215 "DAQ" analog-to-digital convertor module.

Resistance vs Temperature Measurements

To characterize the temperature dependent resistance, a 17 Hz current source is passed through the sample and the generated voltage as a function of temperature is recorded. The current signal is generated from the oscillator output of a lock-in amplifier (EG&G 7260 DSP) and passed through a current limiting resistor. The differential voltage across the sample was amplified with a

SR560 preamp and then fed back into the lock-in amplifier. A 300 msec time constant on the output was used to average the signal. The lock-in output was then acquired using the NI DAQ system and converted into a dynamic resistance (dV/dI) as a function of temperature using Labview. The preamplifier filters were set to low pass with a 3 kHz bandwidth. The temperature was measured using a Lakeshore DT-670 Si diode sensor and a Cryocon model 32 temperature controller. Excitation currents were chosen to deliver ~10^5 mA/cm^2 to measure Tc. Critical transition temperature measurements require excitation currents that are larger than the experimental noise but small enough to capture the onset of critical current. The thermal link between the sample and the temperature sensor must be very strong to assure that the sample is at the same T as the thermometer.. To minimize any lag between the sample and thermometer temperature, the cooling rate is limited to <50-100 mK/sec.

Current-Voltage Characteristic Measurements

Current-Voltage (IV) characteristics are the most fundamental SQUID measurement, and are useful to examine the Josephson junction parameters. The simplest configuration uses a 0.5 Hz current source generated from an Agilent 33522A function generator passed through a current limiting resistor and a current sensing resistor in series with the sample. The differential voltage across the current sensing resistor is amplified with an SR560 preamp and measured. A lower noise method involves the use of a customized current driver circuit, where a summing amplifier is used to collect the excitation signals fed into a differential current drive circuit, that subsequently biases the

SQUID. Ground loops are broken using a differential current drive technique. The voltage developed across the sample is measured and amplified with another SR560 preamp and digitized. Typical preamp gains for SQUID arrays are of the order of 1000x, with the low pass filter set to 12 dB at 300 Hz. A minimum of 1000 points acquired at 10,000 samples per second was used for digitization of both the current and voltage channels. IV characteristics of Josephson devices must be performed at high enough current bias to capture the asymptotically linear behavior of the RSJ type devices. Current-Voltage characteristics are commonly measured over a range of temperatures with the highest temperature based on the zero voltage Tc obtained from the RT measurement.

For SQUID devices, a fast magnetic field can be applied to the sample at the same time as the slow current sweep used in the IV measurement. If the magnetic field is at least 10x faster (typical 30 Hz) than the IV sweep (typical 0.5 Hz), then at all regions of the IV will modulate with the magnetic field. When the applied field is equal to one flux quantum, then the maximum depth of the SQUID IV modulation in the current axis can be used to estimate the current modulation [20].

The critical current vs magnetic field "Ic(B)" characteristic can be extracted from the magnetic field modulated IV curve. A typical Ic(B) measurement is performed using a slow 25 mHz magnetic sweep while measuring the IV characteristic at 7 Hz. The magnetically modulated IV characteristic is acquired with 100,000 points at 10,000 samples per second. The critical current is numerically extracted using a numerical sample and hold

scheme, where a current sample is taken when a specified voltage threshold is exceeded (often 1-10 uV for single SQUIDs).

Voltage vs Magnetic Field Characteristic

Voltage vs Magnetic Field (VB) characteristic of SQUID devices is acquired using a battery generated DC bias current fed into the SQUID using a wire-wound adjustable resistor. Magnetic field is swept through a solenoid coil coupled to the SQUID using a 1 Hz excitation generated from an Agilent 33255A function generator. The magnitude of the magnetic field is recorded using a current sensing resistor in series with the magnetic coil, where the coil current is scaled by the coil constant to obtain the applied field. The coil constant was calibrated independently using a Hall sensor Gauss meter. The coil current and the SQUID voltage are amplified using two SR560 preamplifiers. Many different SQUID bias currents in both polarities should be acquired to characterize a SQUID device. Small magnetic field ranges characterize the SQUID properties, whereas large field ranges probe the junction Fraunhofer pattern.

Dynamic Impedance Measurements

Analog dynamic impedance measurements can be performed on both the IV and VB characteristics. A 2.2 kHz amplitude modulation (0.1-1.0%) is added to either the current (IV), voltage (VI), or magnetic field signals (VB) swept at 25 mHz generated from the Agilent 33255A. Three different SR560 preamplifiers are used, two set as low pass amplifiers with a 12 dB roll-off knee at 30 Hz, one high pass amplifier with a 12 dB roll-off knee at 100 Hz. The high pass preamp is fed into a SR7260 DSP lock-in amplifier synchronized with the

amplitude modulation output from the Agilent 33255A generator. A 5 msec lock-in time constant is used to average the dynamic signal. For IV measurements, the lock-in output is equal to the small signal dynamic resistance (dV/dI) or dynamic conductance (dI/dV). For VB measurements, the lock-in output is equal to the small signal field-to-voltage transfer function (dV/dB).

4. Mutual Coupling Effects in Closepacked Series-Parallel SQUID Arrays

Motivation

A number of groups around the world have a continuing interest in the development of serially connected (DC) SQUID arrays. Series arrays of SQUIDs are a promising solution for applications that are compatible with lumped element architectures, such as wideband RF sensors [57][58], high slew rate second stage amplifiers [59][60], and absolute field sensors (SQIFs) [61][33]. In order to construct high performance SQUID arrays, a scalable Josephson junction technology must exist that can be patterned with a high device density, maintain required properties with arbitrary substrate placement, and with low parameter spread in junction parameters i.e. critical currents (I_C) and normal state resistances (R_N). All of these design constraints have been met in niobium technology at liquid helium temperatures ($Nb \cdot AlO_X \cdot Nb$ trilayer junctions), however circuits at higher temperatures require the use of complex material systems such as $YBa_2Cu_3O_7$. In this work, ion damage Josephson junctions are used to construct large scale series-parallel SQUID arrays for use in Earth's field environments.

Tight geometric placement of SQUIDs in an array is highly desirable to both increase device voltage and decrease intrinsic/environmental noise. Consider a SQUID array where all of the individual SQUIDs in an array are optimally biased at the same working point with identical flux coupling into all

elements (uniform fields). The peak-to-peak voltage of N identical SQUIDs in series scales as N, hence the transfer function should also scale with N. The noise of a series array is proportional to the $\sqrt{N}$ when the thermal noise from the junction resistors is dominant [20]. In addition to the junction noise, the other dominant noise source is the SQUID flux noise. Flux noise power S_Φ is inversely proportional to the SQUID transfer function $\frac{dV}{dB}$ (Volts/Telsa proportional to N), thus the white flux noise power scales as $\frac{1}{N}$ [62]. Hence significant signal-to-noise increases are possible in very large series SQUID arrays ($N \gg 1$).

Circuit imperfections are always present, such as material defects, processing induced degradation, or lithographic deviations. Therefore an ideal SQUID array topology should be robust, particularly versus junction parameter spread. A scalable parallel architecture is a possible path forward, where weak and broken connections are bypassed across a segment of SQUIDs constructed in parallel to the bias current. In the presence of small parameter variations, parallel SQUIDs coherently phase lock resulting in a beneficial averaging effect. However, SQUID arrays are inherently less sensitive than single SQUIDs for applications with external detection coils. Picotesla and smaller field sensitivities have only been demonstrated with external detection coil architectures designed to increase the effective SQUID area. External detection coils are typically coupled to a single SQUID via a coplanar input coil directly placed on a flux focusing structure integrated with the SQUID. The tight flux coupling of a single SQUID is lost in a parallel SQUID array device since the coplanar input coil must wrap around the parallel array, with the input flux split between many SQUIDs. Independent input coils for each SQUID have been demonstrated for series arrays, however not for parallel arrays [59].

Therefore a clear trade-off exists between magnetic field sensitivity and parallel array size, where robust performance is expected in either case. Consequently parallel arrays are generally unsuited for applications demanding picoTesla or better field sensitivity, but parallel devices tend to be more robust towards circuit imperfections, materials degradation, and thermal fluctuations.

Unique layout considerations exist in the design of large arrays of SQUIDs, such as the opposing constraints of high SQUID density and high SQUID field sensitivity (large area per SQUID). Secondary considerations include the layout design rules for a given junction and lithography technology. The inductance of SQUIDs constructed from magnetically thin $YBa_2Cu_3O_7$ films (thickness on the order or less than the magnetic penetration length) is dominated by the kinetic inductance rather than the geometric inductance, necessitating small loop areas for maximum SQUID modulation. The SQUID modulation is commonly parameterized by $\beta_L = \frac{LI_C}{\Phi_0}$, where $\beta_L \leq 1$ describes a SQUID with greater than 50% current modulation in response per flux quantum [20]. Here L is the total SQUID inductance, I_C is the SQUID critical current, and Φ_0 is a flux quantum. To compensate for a decreased SQUID area, additional flux-focusing structures must be attached to the SQUID that are much larger than the SQUID loop. Flux focusing structures reduce the maximum number of SQUIDs possible per unit area. Hence we use a practical metric of maximum output voltage per unit area as a function of SQUID field sensitivity. The trade-off between field sensitivity and voltage output must be well understood prior to the circuit layout for high performance applications.

In this Chapter we investigate the properties of SQUID arrays with SQUIDs directly connected with neighboring devices and feature sizes near the photolithographic limit. First we consider the basic device physics of mutual inductance, competitive currents, and flux trapping effects for these "closepacked" SQUID array circuits. Then we will compare the DC performance of closepacked series-parallel arrays to "loosely coupled" parallel arrays in series.

Mutual Coupling Effects

It is often assumed that SQUIDs in close proximity will suffer from performance degradation when the mutual inductance between SQUIDs becomes significant. Here mutual coupling between adjacent SQUIDs is mediated by self-fields generated by the screening currents within each SQUID generally antiparallel to the applied field. Since the mutual coupling works against the applied field, tightly coupled SQUIDs can become less sensitive. Additionally, partial decoherence can result since the antiparallel fields can introduce spatially inhomogeneous phase offsets (varying screening current magnitude) since self-fields fall off with distance. Both decreased sensitivity and spatially inhomogeneous phase offsets present unique challenges for generalized circuit layout design rules. In this section we describe and elaborate on the details of the mutual coupling effects.

If the physics of the phase coherence of the 2-junction SQUID ("DC SQUID") is analogous to double slit interference in optics, then the analog of a parallel segment of "P" DC SQUIDs (P+1 identical junctions in parallel) is a P-slit interference grating. Parallel SQUID array devices have been investigated

from the early days of SQUID research [63] [64]. P+1 junctions in parallel only exhibit SQUID properties when they are connected by a small inductance (small β_L), else the quantum interference disappears between parallel junctions. In the absence of self and mutual inductance effects, the SQUID current modulation with magnetic flux can be qualitatively understood in the form of the diffraction relation of a linear grating [64]:

$$I_C(\Phi) = I_C(0)\left|\frac{sin\left(P\pi\,{}^{\Phi}/_{\Phi_0}\right)}{sin\left(\pi\,{}^{\Phi}/_{\Phi_0}\right)}\right|$$

Where "P" is the number of the slits in the grating. There are two periods observed in the $I_C(\Phi)$ pattern: the largest current change corresponding the single SQUID area and a minor period corresponding to the sum of all the SQUID areas in parallel. The smaller magnitude minor period rides on a "flattened bottom" near integer values of $\frac{\Phi_0}{2}$ between sharpened current maxima at integer values of of Φ_0. E Cho [19] has recently investigated the interference grating SQUID circuit using a Fourier analysis technique to extract the current distribution.

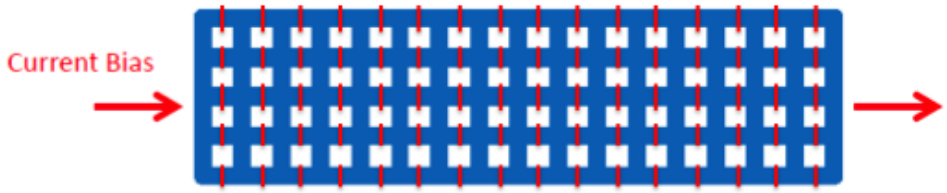

Figure 48: Exemplar NxP Closepacked SQUID array with N=16 and P=4. Ion damage Josephson junctions indicated in red

Consider a segment of "P" identical DC SQUIDs connected in parallel, such that all junctions are shared between two SQUIDs except the junctions on the 2 edges (see Figure 48). For "short" junctions (see Chap 1) the currents are uniformly distributed across the full junction width resulting in a uniform phase

difference ϕ_i across each junction. The total current through the segment is $I_{Tot} = \sum_{i=0}^{i=P+1} I_C(i) sin\phi_i$ (note P+1 junctions for P SQUIDs in parallel), such that the net phase difference across each SQUID is difference in phase between the two parallel junctions $\phi_j - \phi_i = \left(\frac{2\pi}{\Phi_0}\right) \Phi_{ij}$ where Φ_{ij} is the flux enclosed by the loop containing the ith and jth junctions. Thus the flux can be contributed from 1, 2, up to P SQUIDs. The enclosed flux contains the contributions from the applied field, SQUID self-inductance, and mutual inductance (closely following reference [65]):

$$\Phi_{ij} = \Phi_{applied} + \Phi_{self} + \Phi_{mutual}$$

$$\Phi_{self} = L_i I_C(i) sin\phi_i - L_j I_C(j) sin\phi_j$$

$$\Phi_{mutual} = M_{i-1} I_C(i-1) sin\phi_{i-1} - M_{j+1} I_C(j+1) sin\phi_{j+1}$$

Where $L_{SQUID}(ij) = L_i + L_j$ is the SQUID self-inductance, M_{i-1} and M_{j+1} are coefficients representing the flux passing through a SQUID loop originating from the left and right (respectively) side arms in the parallel to the bias current. In general M_i is not equivalent to the mutual inductance calculated from two adjacent closed loops. Flux from nearest neighboring SQUID loops is always opposite in direction to the self-induced flux. Mutual flux on the order of the self-flux will result in a reduced flux change within the SQUID loop and hence a diminished SQUID response. In a regular square lattice of closed superconducting loops, a strong mutual inductance effect would manifest in a checkerboard of antiparallel neighboring flux quanta (the lowest energy configuration) [4].

Analysis of the same geometry with 2 SQUIDs in parallel (P=2) has previously been shown that the maximum critical current of the parallel segment is equal to $I_{Tot} = \sum_{i=0}^{i=P+1} I_C(i)$ only in a specific range of conditions,

such as identical critical currents for all junctions and negligible mutual inductance [65]. Hence, one indicator of a significant mutual inductance effect would be sublinear critical current scaling with the number of short junctions in parallel. Additionally, any irregularity and asymmetry in the major and minor periods or changing lobe pattern over many flux quanta would be indicative of significant mutual coupling and junction parameter spread [66]. As the mutual inductance is increased in a uniform closepacked array, the magnitude of the critical current modulation to magnetic field decreases for the minor grating peaks (inhomogeneous flux between parallel SQUIDs). Increasing mutual inductance also decreases the sharpening effect on the single primary oscillation peaks.

In principle, the mutual flux can be estimated by calculating the field generated by the nearest neighbor side arms within the SQUID aperture (Biot-Savart type). In practice the static current solution for each junction requires the solution of the simultaneous differential equations of all parallel junction phases combined with the flux quantization constraint of each closed loop. Hence simulations must incorporate an empirical model of junction parameter spread and a specific device geometry to obtain accurate results and have not been performed by the author.

Competitive Current Effects

Flux enclosed within a superconducting loop is equal to the line integral of the phase gradient around the loop. The phase difference around the loop is proportional to the circulating current. The path of the line integral is generally taken deep enough within a superconducting electrode so as to

include all magnetically induced currents. However, if the induced currents from intimately placed structures overlap, i.e. structures sharing electrodes, then any integration path necessarily includes current contributions from multiple loops. The superposition of circulating currents from these sources must be simultaneously solved within the flux quantization condition for each coupled loop. Here we describe the complex interaction of screening currents within a superconducting electrode shared between multiple SQUIDs as a competition between currents. To solve for the quantization condition we choose to integrate the phase around the SQUID loop along a path defined by the magnetic penetration depth. When the magnetic penetration depths overlap from adjacent structures, the fluxoids become phase linked and phase bias is introduced.

External magnetic fields (less than H_{C1}^{Film}) are screened from the inner superconducting regions by induced currents up to the London penetration depth λ_L from the electrode surface (in the absence of flux trapping). The induced continuum of current paths in which the supercurrent density is constant within λ_L are easily visualized as current "streamlines" (Figure below). These streamlines of screening current can be further visualized as cylindrical-like surfaces within the electrodes surrounding the superconducting loop of a magnitude sufficient to screen the external flux ($\Phi_{\text{screening}} = L * I$ where I is total sum of the induced current). The local supercurrent density is given by $\vec{J}(x,y) = \frac{-1}{\mu_0 \lambda_L^2}[\vec{A} + \frac{\Phi_0}{2\pi}\nabla\phi]$ [67]. In the magnetically thin ($thickness \leq \lambda_L$) limit these surfaces of constant phase gradient (streamlines) uniformly penetrate the thickness of the film. The magnitude of the phase gradient is proportional to the supercurrent tangential to each surface in the absence of magnetic fields.

The calculation of current distribution of any particular segment must include the screening currents from all neighboring structures superimposed with the bias currents (Figure below).

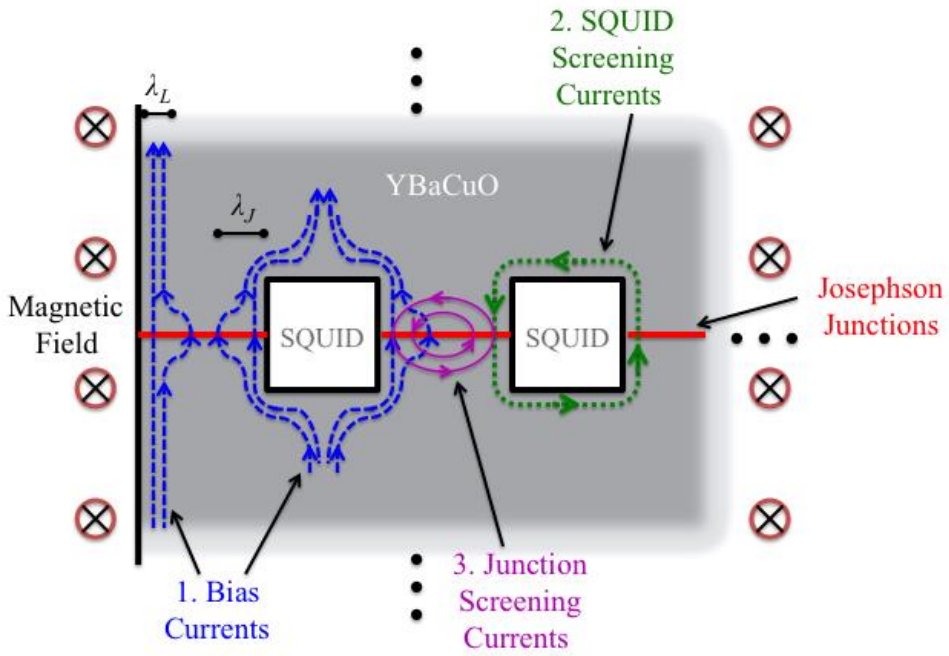

Figure 49: Top down view of a parallel SQUID array constructed from a magnetically thick film of $YBa_2Cu_3O_7$ and planar ion damage Josephson junctions. Approximate current streamlines are illustrated coming from three separate contributions: 1. Current bias (dashed blue), 2. SQUID loop screening currents (dotted green), and 3. Josephson screening current (solid magenta). The London penetration depth λ_L and Josephson penetration depth λ_J are labeled for clarity.

The magnetic penetration length is a material dependent parameter defining the depth an external magnetic field will penetrate a superconductor. In c-axis oriented $YBa_2Cu_3O_7$ films the in-plane London depth for fields applied perpendicular to the surface is typically 150-170 nm at 0 K. Any thick superconducting wire with its smallest dimension much greater than the magnetic penetration depth would have zero magnetic field in the center, except for an exponentially decaying edge region of characteristic depth λ_L; 95% of currents will be within $2\lambda_L$. Hence the concept of cross-

sectional averaging of currents and therefore phase are poorly defined in magnetically thick circuits since the current flow is not homogeneous-rather flowing within ~λ_L of the edges.

Phase biases from overlapping currents become important when the spacing between superconducting loops is on the order of the magnetic penetration depth. Superconducting loops spaced closer than $4\lambda_L$ will superimpose fields caused by induced currents. The overlap of screening currents from multiple sources indicates the interaction of fluxoids ($\overrightarrow{\Phi_L} = \vec{A} + \lambda_L^2\vec{J}$) between the two loops, decreasing the potential energy barrier between the adjacent vortices. The effective penetration length is a function of temperature and film thickness. Screening currents must penetrate deeper than λ_L for complete flux exclusion in very thin films. The diamagnetic surface energy is also decreased from the bulk film, which reduces H_{C1}^{film} (see next section on flux trapping). The effective penetration length in very thin films is given by the Pearl Length $\Lambda = \frac{{\lambda_L}^2}{thickness}$ valid for $\Lambda \geq \lambda_L$. Generalizing the magnetic penetration length for 2D (thin film) systems, the effective 2D screening parameter is then the Pearl length divided by the width of the electrode $\Lambda_{2D} = \frac{\lambda_L^2}{thickness * width}$ (unitless).

In a sufficiently wide and/or thick superconducting electrode relative to the effective penetration length Λ (aka $\Lambda_{2D} < 1$), then magnetic fields will be confined to the edges of the electrodes. When $\Lambda_{2D} \geq 1$ fields will be present throughout the electrode and not only in the holes, the kinetic inductance dominates the geometry, and the flux barrier energy decreases. It is important to note, that in thin films the majority of the screening energy is stored in the

charge carriers rather than in trapped magnetic fields. Hence the maximum/largest mutual inductance coupling between closed superconducting loops decreases with decreasing film thickness.

For the reasons described above, thick electrodes (in all dimensions) are the preferred design constraint for SQUID devices. For SQUIDs operating near $\frac{T}{T_C^{film}} > 0.8$ (assuming a Gorter-Casimir type penetration depth $\lambda(T) = \lambda(0)\left[\sqrt{1-\left(\frac{T}{T_C}\right)^4}\right]^{-1}$), special consideration to the temperature dependence of the London length is required. The London penetration depth changes by less than 5% percent from $0 < \frac{T}{T_C^{film}} < 0.5$, but by as much as 300% in the range $0.9 < \frac{T}{T_C^{film}} < 0.99$. In fact, many materials properties (the energy gap, H_{C1}, H_{C2}, coherence length) are close to full value at temperatures significantly below T_C. Hence, device operation near 77 K is merely a cooling convenience for materials such as $YBa_2Cu_3O_7$ and actually defines a sensitive working point temperature where all these parameters are still temperature dependent. The wide range of possible operating temperatures is a significant advantage to the unconventional high T_C superconductors. However the best circuits studied for conventional superconducting materials have been long known to operate such that $\frac{T}{T_C^{film}} < \frac{1}{2}$ (e.g. Nb in liquid helium: $\frac{4.2\ K}{T_C = 9.2\ K} = 0.46$).

In the phase bias regime of overlapping currents, the superposition of circulating currents within a shared SQUID arm can diminish the net circulating current and introduce flux dependent field (phase) offsets to the SQUID current-field characteristic. Here we assume the critical current of all electrodes to be much larger than the SQUID critical current (typically 1-100

μA). Following [68], the critical current of a single SQUID tightly coupled to a second closed superconducting loop is

$$I_C^{SQUID}(\Phi) = I_C^{SQUID}(0)\left|\cos[\frac{\pi\Phi}{\Phi_0} + \pi\left(\frac{\Phi}{\Phi_0} - n\right)\alpha]\right|$$

where n is an integer and α is defined as

$$\alpha = \frac{\frac{a}{s} + \frac{M_G}{L_K}}{1 + \frac{L_G}{L_K}}$$

where "a" is the length of the shared wire, "s" is the circumference of the second loop, M_G is the geometric mutual inductance between the two loops, L_G and L_K are the geometric and kinetic self-inductances of the SQUID loop (respectively).

Consider two SQUID loops (holes) that are closely spaced such that they share a single conduction path in parallel with the bias current. If the electrode is constructed such that $\Lambda_{2D} \geq 1$ the induced circulating currents from each hole overlap, and the resulting currents will be a superposition of the induced currents from both loops. If the loops are identical then the sum of currents are equal in magnitude and opposite in direction in the shared electrode. Hence for very closely spaced loops the resultant current will be partially or completely cancelled. In reality, this of course depends strongly on the differences of the junction currents. For instance, large critical current asymmetry in a single 2 junction DC SQUID will result in the VB characteristics approaching a single junction SQUID (RF SQUID) character. A large mutual inductance between identical closepacked SQUIDs would result in decreased field sensitivity from what would be expected from the single SQUID.

Hence in the competitive current regime both flux focusing and phase offset effects would be present. Flux is excluded from the neighboring closed loops and constructively adds to the externally threaded flux effectively increasing SQUID sensitivity (flux focusing). In the limit of vanishing inductance (small neighboring loops), an additional phase of $\frac{a}{s} * 2\pi$ is added to the single SQUID resulting in a shift in the apparent external field where the critical current is maximized i.e. the position of the central peak shifts. In general the central peak position is also a function of the trapped flux in the neighboring loops. In a closepacked regular square array (see Figure 48), most SQUID loops are surrounded on all sides, and are sharing electrodes with the SQUIDs in the series and parallel directions. In the case of all identical SQUIDs (junction parameters and SQUID areas) throughout the array the phase contribution of competitive current effects would cancel. However, any variation in the inductance, critical currents, or effective SQUID areas (SQIF devices [69]) would result in significant competitive current effects. Hence the litmus test for competitive currents in a regular array of SQUIDs would be de-phasing of net SQUID phase (phase offsets results in multiple oscillations at roughly the same frequency) or offsets in the central peak position between closepacked and separated/spaced apart/segmented arrays.

Potential Energy Barriers for Flux in SQUID Arm Electrodes

A potential energy barrier exists throughout the circumference of closed superconducting loops to impede the entry and exit of flux vortices. McCumber and Halperin estimated the energy required for a phase slip (vortex entry) across a superconducting wire at zero current to be

approximately $\frac{\sqrt{6}I_{C_{wire}}\Phi_0}{2\pi}$ [70]. Hence flux will tend to cross a superconducting loop at the point of lowest critical current i.e. the Josephson junctions. The barrier energy is higher than typical thermal fluctuations even for wires on the nanoscale, although fluctuations persist from other mechanisms [71]. The work of Cho and Cybart has shown that critical currents on the order of 1 mA for 100 nm wide wires of 25 nm thick $YBa_2Cu_3O_7$ corresponds to a barrier energy of approximately 10,000 K. Meissner currents in narrow wires are highly elongated, where screening currents are unable to circulate freely and must follow the wire geometry. Flux vortices are therefore difficult to form in narrow wires, where the elongated currents significantly strengthen the potential barrier for flux entry. Below the critical field $B_{Critical} \sim \frac{\Phi_0}{(width)^2} < H_{C2}$ flux vortices are completely expelled from the interior of a narrow superconducting strip regardless of the materials properties [72]. Wires 5 microns or less will completely exclude vortices in the presence of the Earth's field when $\Lambda_{eff} > width$ (magnetic field penetration throughout the wire). Therefore the potential energy barriers to flux motion in a SQUID array can be controlled through circuit layout in both Josephson junction placement and wire width.

Flux quantization of closed superconducting loops necessitates at least one "jump site" where vortex movement is possible, else the loop would never be able to gain or lose flux (satisfy the flux quantization condition). Consider the simplest model where the lowest Ic along the loop will be the preferred jump location. All other locations will have a potential barrier to flux entry proportional to the Ic at that location. If the Ic was the same everywhere along the loop then the flux will not prefer to jump at any specific location and will have an equal probability to jump anywhere along the loop

circumference. A trapped vortex within a superconducting loop is stored as a surface current of a sufficient magnitude ($\Phi_{loop} = L * J$ where J is the circulating current) to generate an exact integer number of enclosed flux quanta. The "hole" formed by the SQUID loop is the energetically favorable point where the magnetic field has the lowest potential energy ($\vec{J} = 0$ but $\vec{A} \neq 0$). The application of a current $I(x, y)$ at any point on the loop will exert an effective magnetic force on the trapped vortex, roughly equal to the magnitude of the overlap of the magnetic field patterns generated by the vortex and the current at that point ("magnetic pressure" [73]). Brandt and Clem [74] have numerically calculated the spatial distribution of fields and currents for isolated, magnetically thin superconducting loops.

In the absence of trapped flux within the electrodes, the preferred flux jump point for SQUIDs will always be the points of lowest critical current i.e. the Josephson junctions. In other words when variations in $J_C(x, y)$ occur over distances large compared to the vortex size, the regions of large and small $J_C(x, y)$ constitute potential-like wells and hills for physical motion of the vortices [73]. The ends (edges) of the junctions attract vortices because of the net zero critical current $J_C(x, y)$ outside of the electrode (the image anti-vortex externally attracting the junction vortex).

A Josephson junction interrupting a closed superconducting loop dramatically lowers the energy barrier and serves as a preferred jump site for flux into or out of the loop. In a 2 junction SQUID biased in the voltage state, the flux action is to enter through one junction and simultaneously exit the other. When a Josephson junction connects two separate superconducting loops, flux can be "shuttled" from one to the other following the Lorentz force

direction [73]. Loops interrupted by overdamped junctions (for instance RSJ) limit flux jumps to a single potential well hop at a time. Hence it is possible of all SQUIDs in a parallel array to shuttle flux in the same direction through their shared Josephson junctions simultaneously. However, when two loops share an electrode that doesn't contain a junction, then the flux is unlikely to be shuttled between the two loops unless the Ic of the shared electrode is the lowest Ic in either loop. Hence closepacked series-parallel SQUID arrays of the type shown in Figure 1 are likely to exhibit interference patterns from neighboring loops in parallel, while interference in the series direction is very unlikely.

Experiment

Two different series-parallel SQUID array layout architectures were created to test the effect of tight placement of SQUIDs in the series direction. Circuits were fabricated with $YBa_2Cu_3O_7$ ion damage Josephson junctions using nanolithography and ion irradiation on 4 inch wafers. Detailed descriptions of the fabrication process have been described earlier (See chapter 3). The Figure below shows the layout of both "segmented" and "closepacked" N series by P parallel SQUID arrays. The closepacked array geometry most closely approximates a completely regular 2D array of SQUIDs. N was fixed at 1000 for all arrays, and P was varied from 1-9 SQUIDs (2-10 junctions) in parallel. Small inductance SQUIDs were designed with square holes 3 um x 3 um, $L_{geo} \sim 20\ pH$. Hence for a maximum current modulation design ($\beta_L \leq 0.1$) the 2 micron wide junctions must have a critical current on the order of $10\ \mu A$ (3.3 kA/cm^2 for 150nm thick films) or less. The spacing of

each parallel segment in the "segmented" array was chosen to minimize mutual inductance between SQUIDs in the series direction.

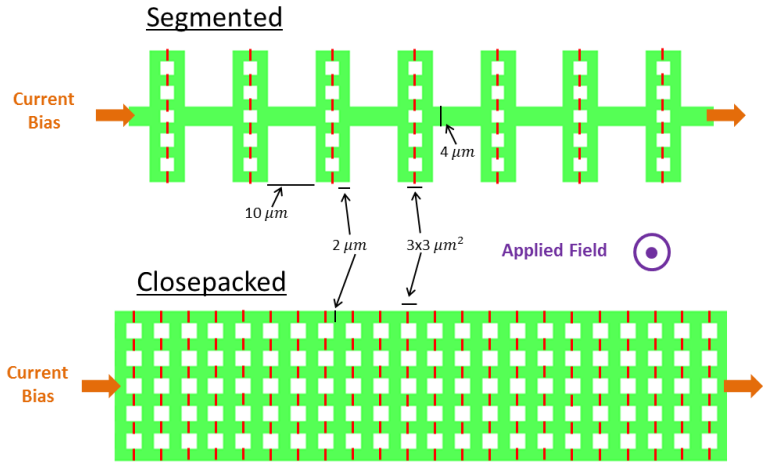

Figure 50: Selected portion of the circuit layout for Segmented versus Closepacked SQUID arrays. Ion damage Josephson junctions are indicated in red, $YBa_2Cu_3O_7$ in green, sapphire substrate in white.

The effective magnetic penetration length $\Lambda = \frac{(150nm)^2}{150nm} = 150\ nm$ in the temperature range $\frac{T}{T_C^{film}} < \frac{1}{2}$, and up to $\Lambda = \frac{(200nm)^2}{150nm} = 267\ nm$ for temperatures $\frac{1}{2} < \frac{T}{T_C^{film}} \lesssim 0.8$ (Gorter-Casimir dependence). Hence the ratio of the penetration depth to the 2 micron bridge width varies from $\Lambda_{2D} = 0.075 - 0.133 < 1$, establishing that magnetic fields will be excluded from the center of the electrode in the absence of flux trapping. Additionally, even in the closepacked geometry the SQUID loops will be magnetically spaced much more than 4Λ apart. Hence we have designed the device geometry to minimize the effect of phase offsets from overlapping currents as is required to isolate the effects of mutual inductance and flux focusing. From a practical viewpoint, the 2 micron wide shared electrode is the smallest dimension we can reliably fabricate over a 4-inch wafer without significant materials degradation and lithographic errors.

Performance

Completed devices exhibited an unirradiated bulk material T_C^{mid} = 84 K with a 6 K wide transition and a junction $T_C{}'$ in the range of 50-60 K. As-grown $YBa_2Cu_3O_7$ transition widths are 1 K or less, indicating the presence of some materials degradation during device processing. The junction dose ($175\ keV\ Ne_{20}^+$ ions at 1e13 ions/cm^2) was chosen to create S-S'-S junctions where the S' barrier region maintains a finite $T_C' < T_C^{bulk}$ i.e. reduced but finite order parameter in the barrier. Current-Voltage (IV) characteristics for the array were first taken in the absence of magnetic field (See Figure below). The IV curves are non-hysteretic as would be expected by the small cross sectional area (3e-7 mm^2) junctions (resultant C ~ 10^{-15} Farad, $\beta_C \ll 1$, junctions overdamped) and the internally shunted nature of the S' barrier. A very large I_CR_N product (2.5 mV) is observed as expected from the large number of devices in series (~1-10 μV per junction). The I_CR_N product does not diminish with the number of devices in parallel (comparing all devices, not shown), indicating that the resistance decreases and the current increases proportionally with the number of junctions in parallel. Individual SQUID I_C was extracted from the apparent I_C^{array} through dividing by the number of SQUIDs in parallel to estimate individual SQUID characteristics. All SQUIDs were characterized by directly coupling the bias and amplifier circuitry to the SQUID in a "direct readout" technique.

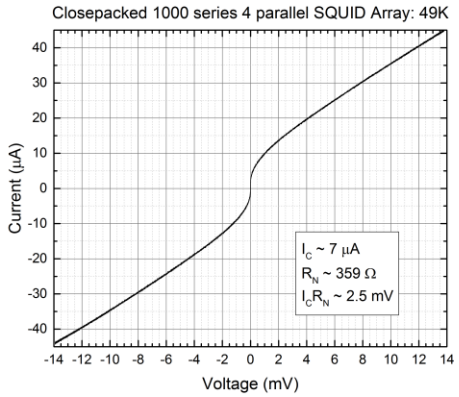

Figure 51: Exemplar IV characteristic for a 1000x4 series-parallel SQUID array. The curvature near I_C is much larger than would be expected from thermal rounding, and is indicative of likely junction parameter spread.

As in previous investigations by our group [33], [75], we find that the curvature near I_C is much larger than would be expected from thermal noise rounding. The voltage onset appears between 5-10 μA, significantly larger than random thermal fluctuations at 50 K (~2 μA). Hence thermal fluctuations alone would not be expected to create the excess curvature near I_C. Instead we attribute the increased rounding to the spread in critical currents in the junctions across the large-scale array (5,000 junctions in a 4x1000 SQUID array). We note that we cannot rule out measurement noise as a possible source of the excess curvature near I_C. We define excess noise as the noise injected into the SQUID circuit from the measurement configuration. Nonetheless, the non-RSJ type curvature near I_C introduces errors in extraction of I_C and R_N that complicates direct comparison of different devices.

When the critical current of the array is divided by the number of junctions in parallel we always find the onset of finite voltage where we can measure SQUID behavior for junction critical currents less than the thermal fluctuations i.e. thermally fluctuated junctions. This remarkable result is unique

to parallel SQUID designs, where phase coherence is maintained for junction currents much less than what is possible in 1D arrays (series only arrays). In the limit of extremely close junction spacing, all parallel junctions couple and behave as a single extended junction with a critical current equal to the sum of all parallel junction currents. If the current doesn't scale with the number of junctions in parallel, then "long" junction effects are present where currents are only carried by the outermost junctions i.e. currents screened from the "interior" of the parallel segment. Hence very closely spaced junctions will behave as a single junction with a net critical current large enough to reduce the effects from thermal fluctuations. Parallel junctions are therefore stabilized against thermal fluctuations, even in the presence of I_C and R_N spread, in the limit of coherent phase around parallel segment i.e. net critical current scales with the number of junctions in parallel.

To characterize the degree of current modulation in the presence of external magnetic fields, a 10 Hz magnetic field roughly equal to a single flux quantum (flux through single SQUID varying $\pm\frac{\Phi_0}{2}$) was applied while simultaneously biasing the array with 0.5 Hz sinusoidal current bias (see Figure Below). In this way the voltage modulation (along $\hat{x}$) of the device can be used to estimate the current modulation (along $\hat{y}$). The ratio of the change in current per flux quanta to the SQUID I_C is a measure of the β_L modulation factor [20][3]. Additionally the bias dependent modulation becomes apparent, where the maximum change in the voltage modulation along the current axis occurs above the SQUID array I_C. Current modulation below I_C is possible due to the combination of early voltage generation from thermal fluctuations and the magnetic field dependence of the in-plane junctions

(Fraunhofer pattern). The maximum voltage response of the SQUID occurs when the SQUID is current biased in the vicinity of the largest current modulation to magnetic flux. At temperatures much lower than the optimum bias point the character of the IV changes, where dynamic resistance continuously increases and the SQUID modulation is significantly reduced (not shown). We attribute both these effects to the start of strong link i.e. "flux flow" behavior. The magnitude of the SQUID array modulation is a strong function of temperature and bias current.

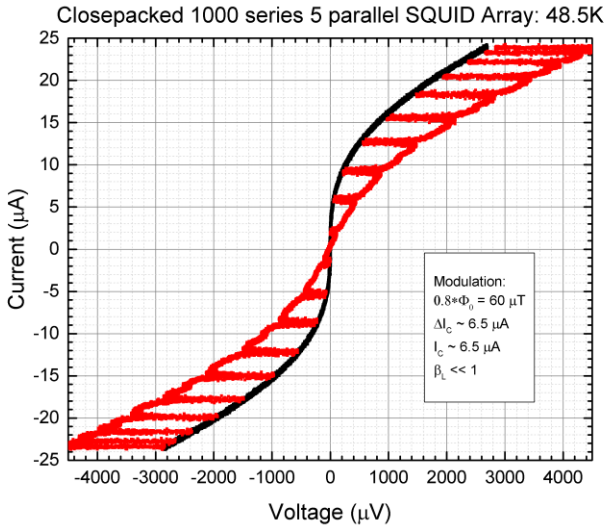

Figure 52: Effect of applying a 10 Hz magnetic field approximately equal to one flux quantum (over area of a single SQUID) to a SQUID array biased with a sinusoidal 0.5 Hz current sweep. The current modulation (vertical distance) between the zero field (black) and with applied field (red) measures the SQUID sensitivity to magnetic fields.

The Voltage-Field (VB) characteristic is the most commonly used SQUID characterization for magnetometers, and is shown below for a current bias chosen to maximize the SQUID peak-to-peak voltage (Vpp). Uniform magnetic fields are applied perpendicular to the array. As the bias current is increased from zero, the Vpp smoothly increases to a maximum and then more gradually

decreases. The magnetic period of largest voltage change corresponds to the SQUID effective area (Figure Below). The effective SQUID radius is equal to the lithographic (loop) hole size plus half the bridge width, confirming the significant flux focusing effect. Rounding of the sharp corners in square SQUID designs is the most significant lithographic error during patterning, thus aperture size is calculated for both round and square holes. A typical dynamic resistance is on the order of 100-1000 Ohms. The magnitude of the SQUID modulation is nearly equal to the $I_C R_N$ product extracted from the IV characteristics.

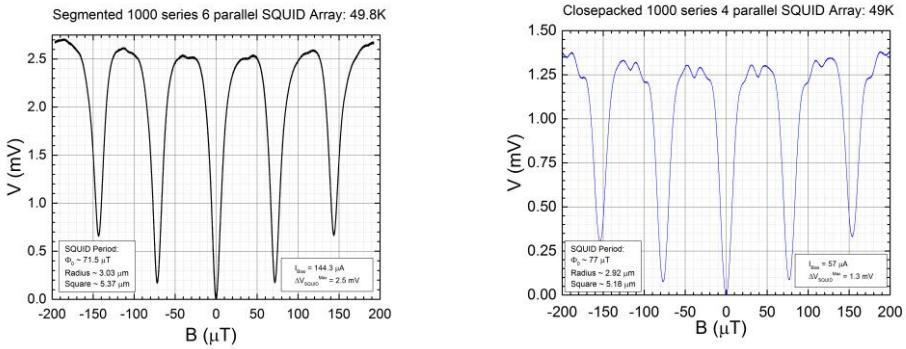

Figure 53: Left – segmented 1000x6 SQUID array with voltage and field offsets removed. Right – close-packed 1000x4 SQUID array with voltage and field offsets removed.

The effective SQUID area (approximately 5 um x 5 um) is dominated by flux focusing effects (SQUID hole 3 um x 3 um), as anticipated since $\Lambda_{eff} \ll (electrode\ width)$. Sharpening of the VB curve is also observed (Figure above) i.e. not purely sinusoidal, with the sharper oscillations observed in devices with more than 2 SQUIDs in parallel. The critical current is maximum and the voltage is minimum at zero applied field. The "flattened top" of the VB characteristic (between -20 uT to -40 uT in the Figure below left) is observed at the $\frac{\Phi_0}{2}$ bias point, where an additional small SQUID oscillation is also evident for small

current biases. The largest Vpp is observed in the central ($B = 0$) minimum with subsequent minima at higher fields decreasing in a characteristically Fraunhofer envelope (Figure Above).

The VB characteristics for both segmented and closepacked SQUID arrays were regular over many flux quanta (Figure Above). The SQUID phase offsets were similar for all devices i.e. similar magnetic field offset. All devices were characterized in a magnetically shielded environment where a residual field of the order of 10 uT was trapped in the mu-metal/permalloy shields during cool-down. Magnetic field offset was the same for all devices irrespective of current polarity (symmetric SQUID inductance). Multiple devices were characterized during each cool down in both the segmented and closepacked geometries to confirm this result. We remark that close-packed SQUID arrays appeared to have higher device yields than segmented arrays. We attribute the increased robustness of the closepacked architecture to the multiply connected nature of the array in the serial direction i.e. large conduction area, whereas the segmented architecture was only singly connected between parallel segments i.e. small conduction area. Large conduction area circuits are robust versus circuit imperfections and materials degradation.

The current bias dependence of the SQUID array VB characteristic is shown below. The subsidiary minima corresponding to the parallel interference grating are most evident at current biases below the maximum Vpp point. The dominant Vpp of the central minimum monotonically increases with bias occurs over a wide range, up to three times I_C ($I_C = 36\ \mu A$ for this device and temperature). Optimum bias currents considerably higher than Ic are

indicative of deviations in the IV curvature from an ideal RSJ model, and points toward parameter spread in the critical currents of the junctions.

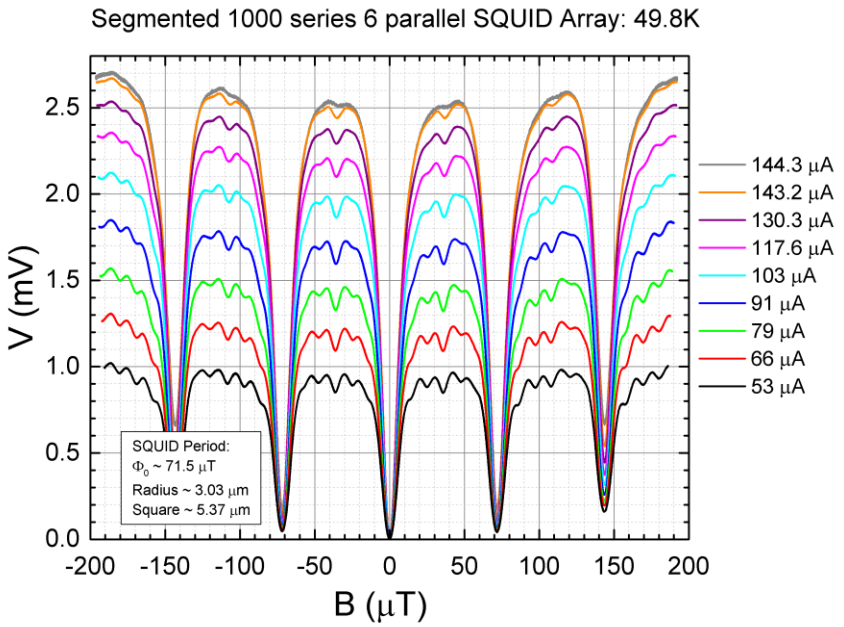

Figure 54: VB characteristics of a segmented 1000x6 SQUID array at different current biases up to the maximum Vpp working point.

The highly regular oscillations between the major minima very closely correspond to the sum of the total parallel effective area in a single parallel segment. This confirms the redistribution of bias and screening currents across the parallel segment with a high degree of phase coherence. The result strongly suggests that screening currents do not significantly couple multiple SQUIDs in the series direction. Cybart et. al. has also reported this result in only the closepacked geometry [33]. Coupling of SQUIDs in the series direction i.e. coupling of multiple London fluxoids along the bias current direction would introduce additional subsidiary oscillations that would not correspond to the number of SQUIDs in parallel. This result supports the model of a barrier to flux

entry in the series direction with flux movement only through the Josephson junctions.

Sharpened (narrower peak) SQUID oscillations are present at all current biases (Figure Above), however the oscillations between the major minima disappear at high current bias. Since the period of the oscillations between the major minima corresponds to the total effective area of all SQUIDs in parallel, the minor oscillations are analogous to a multislit interference grating. Effects from both interference between neighboring slits and diffraction from individual slits are present in a multislit grating. When the interference grating oscillations disappear, the phase coherence between SQUIDs in the parallel direction must also be lost. In the absence of phase coherence between SQUIDs, the parallel array behaves as a multislit grating illuminated with incoherent light. In other words, the disappearance of the minor oscillations is due to a decoherence effect mediated by high current bias. The currents in a shared electrode can strongly interact at high current bias, where initially edge bound supercurrents must flow deeper into an electrode at high bias introducing a competitive current effect. The superposition of supercurrents "competing" for conduction in a shared electrode can introduce sufficient phase variation so that the flux quantization condition across the parallel segment is no longer unique i.e. phase coherence around single SQUIDs but phase decoherence around multiple SQUIDs.

Phase coherence around single SQUIDs with simultaneous decoherence around multiple SQUIDs is only possible in junctions with uniform current density. Uniform current density junctions are known as "short junctions", where uniform currents ensure a uniform phase difference at all

points across the junction. High quality short junction properties as are evident in the Fraunhofer patterns of both segmented and closepacked arrays (Figure below). The Fraunhofer patterns shown in the Figure below reflect short junction behavior with the SQUID period ~8x faster than the junction period. Thin film planar Josephson junctions weakly screen external magnetic fields, resulting in screening currents penetrating a distance roughly equal to bridge width in all directions around the junction [52]. The extracted Fraunhofer period agrees well with the predicted period from the treatments of Humphreys [52] and Rosenthal [15]. We estimate the Josephson penetration depth ~10 microns near 50 K further confirming the short junction nature [76]. Short junction behavior is necessary to support the model of all parallel junctions acting in concert to dominate the thermal fluctuations. Thus we have experimentally demonstrated that the coherence of parallel SQUID arrays is enhanced compared to single SQUIDs in the short junction limit.

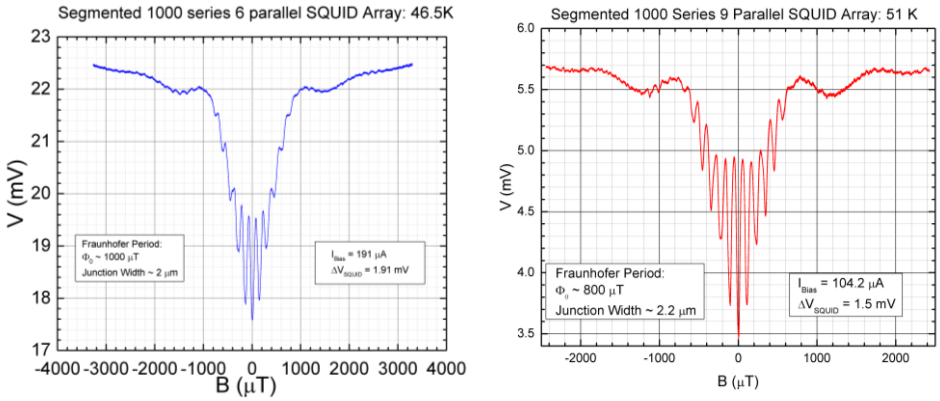

Figure 55: Left – Segmented 1000x6 SQUID array biased for maximum peak-to-peak voltage. Right – Segmented 1000x9 SQUID array also at maximum voltage bias. Note the quality of the junction Fraunhofer pattern superimposed with the SQUID interference pattern. The lithographic variation in the junction bridge width is apparent in the difference between the Fraunhofer periods of the left versus right devices.

An important property of SQUID devices constructed from in-plane Josephson junctions is the magnetic field dependence of the junction that is

superimposed on the SQUID pattern. As shown in the figures above and below, the SQUID oscillations of varying magnitude are present throughout the Fraunhofer pattern. We attribute the change in magnitude of the SQUID oscillations to the Fraunhofer type modulation of the junction critical current with increasing magnetic field. The $\beta_L = \frac{I_C^{SQUID}{}_L}{\Phi_0}$ modulation parameter is proportional to SQUID critical current, which is a strongly field dependent parameter for in-field junctions. Hence the applied field could be used to tune the modulation parameter when the SQUID current is large: a magnetic field dependent β_L. In other words, there is a natural equivalence between the ion dose, bias temperature, and bias field to adjust the current of the weak link. The figure below shows a change in voltage modulation in the first Fraunhofer maxima compared to the zero field central peak. In this case the zero field β_L was already small, with complete current modulation. Thus a further decrease in critical current actually diminished the SQUID voltage modulation. However a large critical current SQUID ($\beta_L > 1$) can benefit from a magnetic field induced I_C reduction to increase the SQUID current modulation per flux quantum. At the time of this thesis no sample has been observed with these properties, and we remark that large flux biases generally increases the SQUID nonlinearity that could be detrimental for some applications.

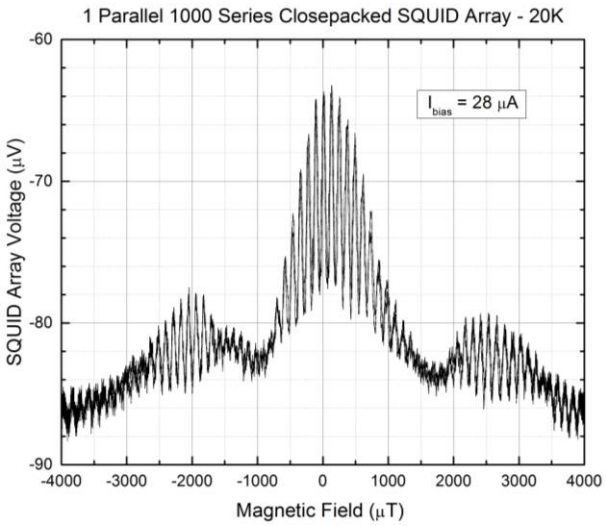

Figure 56: Fraunhofer pattern for heavily damaged Closepacked SQUID array capturing the SQUID oscillations on the zeroth and first Fraunhofer peaks

The temperature dependence of the maximum SQUID Vpp for many devices in 2 fabrication cycles is captured in the Figure below. Due to the sharpening of the VB with increased number of parallel SQUIDs, the central peak Vpp is the best measure to compare devices with different numbers of parallel SQUIDs rather than the commonly used slope based metrics ($\left(\frac{dV}{dB}\right|_{\Phi_0/4}$ in units of V/T). Each point on the graph corresponds to a different bias current, chosen to maximize the peak-to-peak voltage of the central peak oscillation. The SQUID period is stable within 5% from 20-50 K, in agreement with the thermal stability of the London penetration depth for $\frac{T}{T_C^{bulk}} \leq \frac{1}{2}$. The wide range of device parameters and geometries enables a broad comparison of the closepacked versus segmented SQUID array architectures.

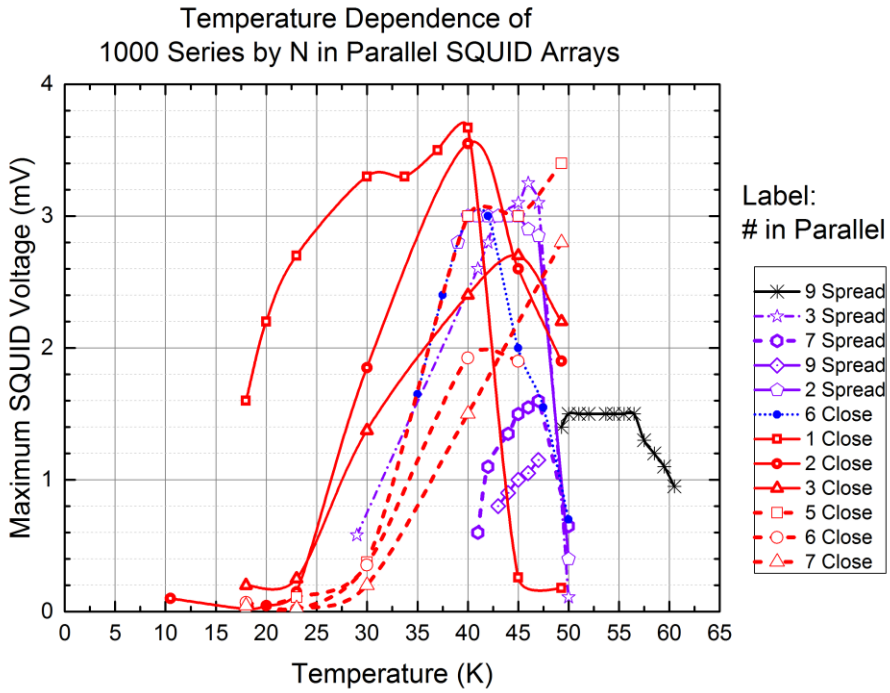

Figure 57: Temperature dependence of S-S'-S junction $YBa_2Cu_3O_7$ SQUID arrays in the closepacked and segmented geometries. No devices except "9 spread" exhibited voltage above 55K. "Close" indicates a closepacked layout, "spread" indicates a segmented layout.

The shape of the maximum Vpp as a function of temperature shown in this figure is unique for S-S'-S SQUIDs compared to S-N-S and S-I-S devices. The Vpp of SQUIDs with either S-N-S or S-I-S junctions will asymptotically increase at lower temperatures [8]. Clearly the maximum SQUID voltage is a strong function of temperature with the largest voltages clustered between 40-50 K (except segmented 9 parallel). Remarkably, both the segmented and closepacked devices exhibit nearly the same temperature dependence and maximum peak-to-peak central peak voltage. The general behavior is as follows with the caveat that not enough data points were taken to determine an exact functional dependence. Almost all SQUID arrays operated at voltages exceeding 1 mV for a wide temperature range (>10 K) successfully

demonstrating massively scalable devices in both architectures (~1000x single SQUID voltage). As the T is lowered below the T_C' of the junctions, the maximum modulation voltage quickly increases ~10 times within 5 K. At colder temperatures the Vpp decreases more slowly with temperature in the range of 0.14-0.17 V/K (notable exception of 1 parallel which is slower). A simple model of the decreased Vpp at lower temperature is to assume a decreased SQUID modulation from an increased critical current at low temperatures i.e. undesired increase of the modulation parameter β_L. However the quadratic increase of the junction critical current ($I_C(T) = I_C(0)\left(1 - \frac{T}{T_{C'}}\right)^2$) is not large enough to sufficiently change β_L to produce an order of magnitude decrease of Vpp in the temperature range 20-50 K. The low temperature onset of flux flow behavior can also reduce the SQUID Vpp since flux flow junctions are less sensitive to magnetic fields compared to typical RSJ devices. Flux flow behavior at low temperatures is a property of S-S'-S junctions [46]. Above all the shape of the maximum Vpp in S-S'-S SQUIDs presented here appears general [77], and can be used as a starting point for empirical S-S'-S device models in circuit simulations.

The change in the SQUID's maximum Vpp as a function of temperature is a sensitive measure of the junction parameter spread. Note that Vpp smoothly transitions between data points in the Figure Above. Junction parameter spread should be well defined and easily observable within these large arrays (2,000-10,000 junctions/device). On average the maximum $V_{peak-to-peak} = N * \overline{I_C R_N}$ which is always less than N identical SQUIDs ($\overline{I_C R_N} < \max(I_C R_N)$) since not all devices within the array can be biased at the maximum Vpp working point simultaneously. Parameter spread (most

evidently critical current) across the large arrays is apparent in several ways (Figure above). First a "residual" voltage is observed in the "close[packed]" devices for $T < 25\ K$ and $T > T_{onset}$ (Figure Above), where the Vpp doesn't monotonically decrease to zero, but rather exhibits a nearly constant voltage for at least 5 K that is ~10x less than observed Vpp max. Residual voltages most likely indicate devices with significant critical current deviations from the majority of SQUIDs within the array. The single parallel SQUID array "1 close" is the most vulnerable to parameter spread. The "1 close" array statistically outputs the same maximum voltage as the parallel arrays, however a stable 100 μV output is observed for 45-50 K indicating ~3% (0.1 mV / 3.6 mV) of devices operate at higher temperatures before the majority activate at 40 K. Additionally, the reduction of the single SQUID array Vpp at colder temperatures is more nonlinear and decreases more slowly at low temperatures compared to the arrays with parallel SQUIDs.

Several arrays ("9 spread", "2 spread") were stable at the maximum Vpp over a 5-7 K range, unlike the other devices that were maximized over a temperature range of less than 2 K (for instance "3 spread"). If the broader range of operation was simply the effect of an increased parameter variance, then the total number of devices optimally biased at any given temperature would be significantly less than 1000 SQUIDs in series and the voltage would be lower. Instead the largest array "9 spread" possessed a statistically diminished Vpp(max) while the "2 spread" voltage matched the experimental average. The smoking gun for increased variance in "9 spread" is the symmetric and temperature broadened voltage onset and falloff. As stated previously, the maximum Vpp for the single ideal RSJ SQUID is insensitive to temperature for

low inductance devices ($\beta_L < 1$) [78]. Hence the temperature stability of the maximum Vpp in the "2 spread" device could indicate a device with low SQUID parameter variance compared to all other devices, which is plausible since "2 spread" is both smaller in device area and junction number compared to the "9 spread" (3000 junctions in "2 spread" compared to 10,000 junctions in "9 spread").

In practice it is difficult to distinguish between a spread in the critical currents of the junctions across the array and non-uniform magnetic fields across the device. These devices are quite large in linear extent (8 mm long), where a 5-10% variation would only require a linear gradient on the order of 100 $\frac{\mu T}{cm}$. Furthermore we cannot rule out a reduced Vpp in the "9 spread" due to the reduced $YBa_2Cu_3O_7$ I_CR_N product at higher temperature. However, both the BCS gap energy and thermal fluctuation energies do not differ enough from 40-60 K to account for the difference in "9 spread" performance compared to the other devices. Despite the parameter spread, we remark that the functional devices yield (~12/99 arrays or 12%) from the two 4 inch wafers comprised an outstandingly uniform batch run for any $YBa_2Cu_3O_7$ SQUID array containing 1,000s of junctions yet seen in the literature.

Conclusion

In this work we have performed transport measurements of a large number of series-parallel SQUID array devices fabricated in our laboratory. Overall we conclude that both closed-packed and segmented architectures containing equal area SQUIDs operate with statistically similar performance. Devices exhibited voltages significantly higher than what is possible with single

ion damage junction SQUIDs (1-100 uV), and establish SQUID array technology as one possible path towards millivolt and higher signal circuits. Technologically we constructed arrays at the lithographic limit of common research photolithography tools, proving SQUID devices can be placed at least as close as 2 microns without significant performance degradation in 150 nm thick $YBa_2Cu_3O_7$ films. All designs exhibited a high degree of phase coherence even in the likely presence of critical current nonuniformity. Hence the common assumption that close-packed SQUID arrays will suffer performance degradation from mutual inductance effects is unfounded in the limit of $\Lambda_{2D} = \frac{\lambda_L^2}{thickness * width} < 1$.

We have demonstrated that ion damage Josephson junctions are massively scalable in two different SQUID array architectures, with a junction density higher than what has been and probably is possible with other technologies: 4.2 million junctions per cm^2 in the closepacked architecture. The typical Vpp temperature dependence of SQUIDs constructed from S-S'-S junctions has been characterized, a necessary step forward towards the development of accurate circuit simulation tools. The broad range of temperature operation (>10 K) is unique to high temperature SQUIDs. It also presents a unique opportunity to any circuit designer for applications requiring a range of working temperatures. Critical current tuning is possible in S-S'-S ion damage junctions with three equivalent parameters: junction ion dose, operating temperature, and applied B-field (Fraunhofer bias).

SQUID arrays constructed from high density junctions are highly favorable for low noise circuits since both the SQUID signal strength and flux noise are improved in very large arrays ($N \gg 1$). High density junctions are also

favorable in the construction of RF lumped element circuits such as RF power detectors and antennas. This work also verified that closepacked SQUIDs are inherently stabilized by the coherent action of parallel junctions. High performance SQUID arrays can be constructed from individual junctions with critical currents smaller than would be stable from ambient thermal fluctuations. Furthermore, high coherence parallel SQUIDs can be tightly placed when the electrode dimensions are sufficiently narrow to impede flux entry except in the junction regions. Understanding these limits opens the door towards the design of multiply connected SQUID circuits such as the BiSQUID (see next chapter) and the design of circuits operating very close to T_C^{film}.

Significant performance limitations still exist in the design of highly sensitive SQUID magnetometers. It is difficult to achieve nanoTesla level or better field sensitivity in SQUID arrays, particularly for applications that require external flux coupling via input coils. Future array designs must incorporate larger flux focusing structures to improve field sensitivity. Two obvious candidates for flux focusing structures include wider shared electrodes and the incorporation of flux focusing "fins" in the parallel direction [62]. Minimized flux trapping and flux movement in $YBa_2Cu_3O_7$materials is key for low noise circuits. Flux focusing structures formed by widened electrodes can easily trap flux and increase SQUID noise through motion of the trapped flux. Previous work has shown that the use of thin film materials with flux pinning centers (flux pinning lowers noise) are unfavorable for the uniform fabrication of high quality Josephson junctions due to film inhomogeneity. A possible path forward is the use of hollow flux focusing structures, for example closed loops directly attached to a SQUID designed with a narrow line width ($B_{critical}$ =

$\frac{\Phi_0}{(width)^2} < B_{ambient}$). Future SQUID array designs could conceivably include flux focusing "loops" within the array to improve SQUID sensitivity, where one such design (BiSQUID) is considered in the next chapter.

5. Comparison of Device Characteristics of Closepacked BiSQUID and Two Junction SQUID Series Arrays

Introduction

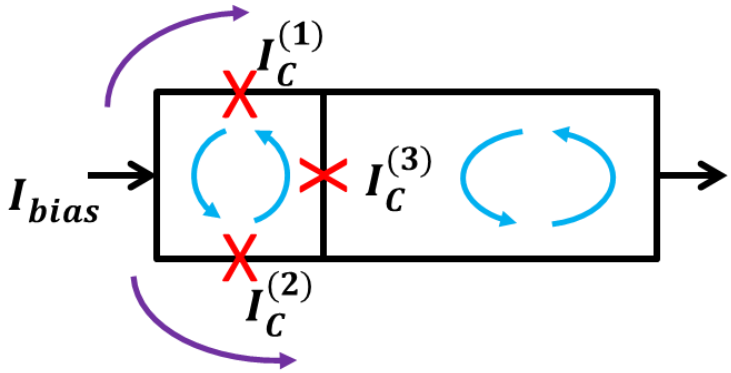

Figure 58: Effective circuit model of the BiSQUID as proposed by Kornev et. al. [79]. Junctions J1 and J2 are shunted by junction J3. Bias currents distribute in purple, magnetic screening currents in blue.

In this chapter we investigate a novel SQUID device containing 3 Josephson junctions called a BiSQUID, which has created recent interest due to its linear Voltage-Field characteristic [80]. The design and optimization of linear BiSQUID circuits was first conceived by Kornev [79]. The BiSQUID "double SQUID" architecture (Figure above) consists of two parallel junctions interrupting a single superconducting loop with a 3rd junction shorting the SQUID loop. In this way two independent loops are formed with 3 junctions in one loop and 1 junction in the other such that the loops are connected in series. BiSQUIDs are typically designed with identical critical currents in

junctions 1 and 2, and with a larger critical current in the 3rd junction. The 3rd junction can remain superconducting when junctions 1 and 2 are biased into the voltage state. In this way the 3rd junction will behave as a nonlinear inductance (when biased below its critical current), which counteracts the non-linearity of the SQUID formed by junctions 1 and 2. Linearization of the BiSQUID Voltage-Magnetic field characteristic is predicted to occur only if the nonlinearities are equal and opposite i.e. within a narrow range of loop inductances and junction critical currents [79]. In this work we directly compare the magnetic interference pattern and Voltage-to-Field transfer function of BiSQUIDs with standard DC SQUIDs.

Circuit Design and Layout

To compare the performance of BiSQUIDs to standard two junction DC SQUIDs, the layout for both devices were designed as alike as possible. The central design goal was to generate a BiSQUID circuit that could be scaled into an arrayed lumped element for High Frequency (HF) sensing. Josephson junctions were designed for a direct write fabrication process using a manual, focused helium ion beam microscope. Direct write patterning enables variable critical current designs using the same junction geometry, in contrast to ion masked patterning which requires variation in junction geometry to change I_C as all junctions are irradiated uniformly [33]. For direct ion beam writing, a maximum microscope write field area of (120 μm)^2 was chosen in the absence of stage movement. YBCO electrode size was constrained to a minimum 4 micron feature (optical lithography) to ensure high fidelity photolithographic patterning. The main circuit specification was to create the

largest SQUID voltage possible, by completely filling the write field with SQUIDs/BiSQUIDs to create a (~120 μm)^2 "cell". Both the BiSQUID and DC SQUID cells were then repeated in a larger array containing many cells accompanied with the appropriate alignment and guide marks for the direct write process. Thus the larger device was constructed using a hierarchical design style with the "cell" at the lowest level. The idea was to ultimately optimize the BiSQUIDs cell design, catalog the optimal layout and circuit parameters, and insert the cell into a layout library as the fundamental circuit to construct RF sensors in a hierarchical design style using design automation software (in collaboration with Hypres, Inc.).

SQUID layouts were designed with low loop inductances to maximize the DC SQUID current (or voltage) modulation. Low loop inductance requires the BiSQUID 3rd junction I_C to be larger than junctions 1 and 2 [79]. The primary SQUID layout is identical in both the DC SQUID and BiSQUID devices with 4 micron wide, 25nm thick YBCO bridges, and a primary SQUID hole of $5\,\mu m\ x\ 5\,\mu m$. Weakened magnetic screening and enhanced kinetic inductance would be expected from such a thin film, with an effective range of Λ such that $\Lambda = \frac{\lambda_L^2}{thickness} \sim 3.6 - 1.6\,\mu m$ penetration depth between 80-50 K respectively. The inductance of the primary $5\,\mu m\ x\ 5\,\mu m$ SQUID hole surrounded by 4 micron bridges was designed using $L_{SQUID} = L_{geometric} + L_{kinetic} \approx 20pH + 80pH$ or approximately 2-3 pH geometric inductance per square with $L_{kinetic} \sim 4L_{geometric}$. Thus the critical current of junctions 1 and 2 is designed at $\approx 10\,\mu A$ or less to achieve 50% or greater current modulation. BiSQUIDs were designed to a fixed 1:2 area ratio between its two holes, with the hole of the 3-junction loop ($5\,\mu m\ x\ 5\,\mu m$) smaller than the hole of the 1-junction loop

($5\ \mu m\ x\ 10\ \mu m$). The BiSQUID hole ratio was devised to aid in analysis where the magnetic interference contribution from each loop can be separated based on the SQUID periodicity. The pattern of the 1 junction loop contains two more squares than the 3 junction loop corresponding to an approximate inductance ratio of $\frac{L_{5x5}}{L_{5x10}} = \frac{8\ squares}{10\ squares}$. Finally, BiSQUIDs designed with a low inductance layout are expected to have the greatest linearity enhancement for 3rd junction critical currents larger than junctions 1 and 2 [79].

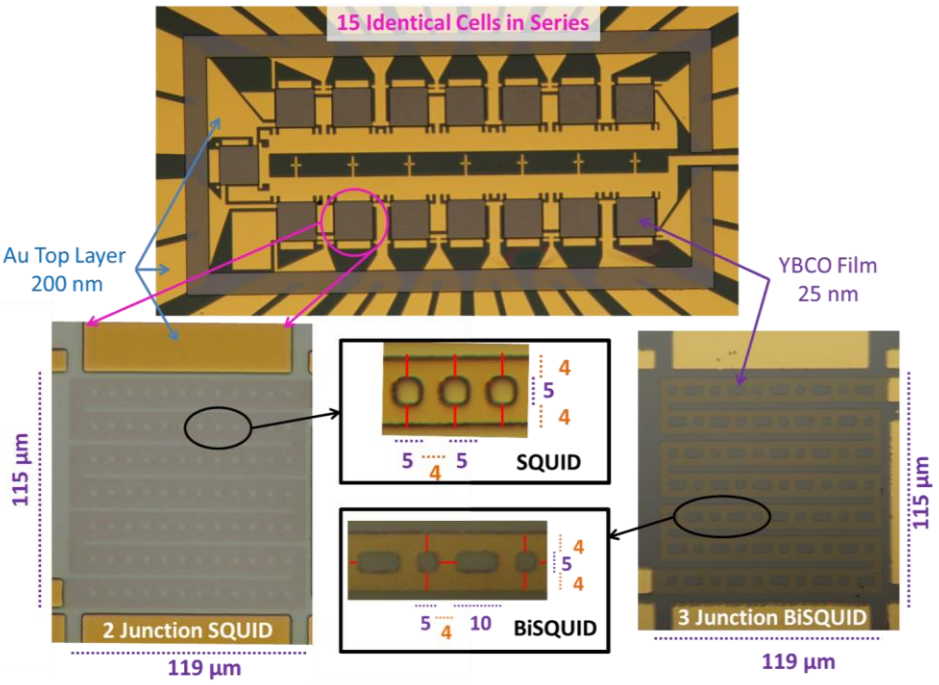

Figure 59: (Top) Optical photograph looking down on the test chip containing 15 cells strung in series used in both BiSQUID and DC SQUID arrayed architectures (see text). Note the multiple leads per device enabling each cell to be measured independently. (Bottom) Close-up of a single cell of each architecture containing either 84 two junction DC SQUIDs (Bottom Left) or 35 BiSQUIDs (Bottom Right). Zoom in (Bottom Center) displays the location of ion damage junctions in red, with dimensions in microns.

The Figure above displays the test chip and cell layout for both the 3-junction BiSQUID and 2-junction DC SQUID architectures. Each individual ~(117 um)^2 cell contains either 84 DC SQUIDs or 35 BiSQUIDs. The device density in each cell is remarkably high, the 2 junction SQUID contains approximately 6.14*10^5 SQUIDs/cm^2 or 1.23*10^6 junctions/cm^2. The circuit was designed with Au over the majority of the circuit to protect the underlying YBCO from spurious irradiation damage during the Helium direct write process. The Au protection layer also minimized charge build-up during junction patterning and heat accumulation during electrode patterning. Both types of arrays were

designed in a multichannel layout with 15 identical, high-device-density cells connected in series on a single 5mm x 5mm die. Only the layout contained within each cell differs between chips, where all electrode and alignment structures are identical for both BiSQUIDs and DC SQUIDs devices. All 15 cells in the series were configured with 4-point probes to test each cell individually, such that the performance of both individual cells and any series combination of cells can be characterized (Figure Below). In particular the device performance and thus $I_C R_N$ parameter spread can be characterized for each individual cell.

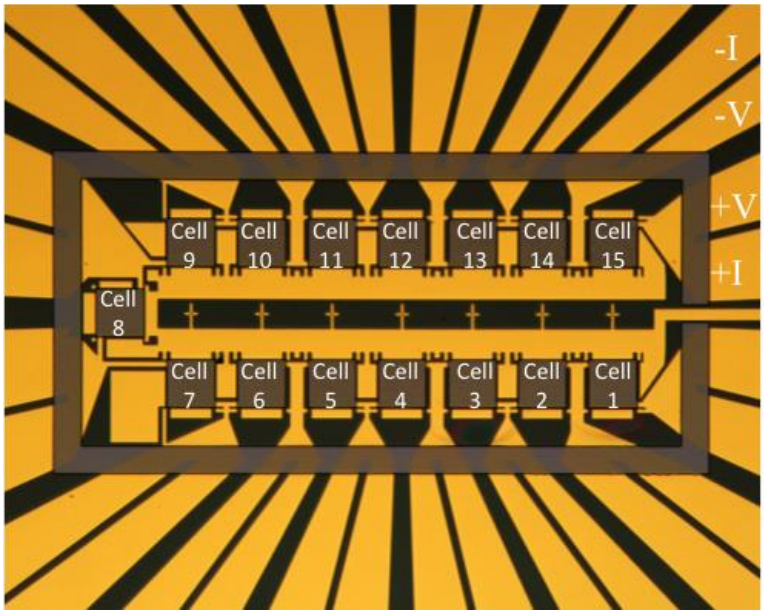

Figure 60: Asymmetric 15 cell circuit with each cell number labeled for analysis. An exemplar 4-point measurement is given for the measurement of cell "15"

Device Construction and Experimental Design

To construct these devices, Theva films [81] consisting of 25 nm thick YBCO (grown on R-cut sapphire substrates) capped with 200 nm of Au (deposited *in situ*) were patterned in one step into the electrode layer using photolithography and Argon ion milling. The YBCO thickness was chosen to be

less than the penetration range of 30 keV He (~40-50 nm). Gold was then removed over the junction regions using photolithography and wet KI & I_2 etching. Subsequently, ion damage Josephson junctions were patterned by Cho and Cybart using their direct write process with a focused Helium ion beam (30 keV He_4^+) [47]. Each cell of either 84 DC SQUIDs or 35 BiSQUIDs was patterned in a single Helium ion microscope field-of-view, where the stage position and focus were adjusted before writing each cell. The junction critical current is a fast function of He ion dose. Thus a range of circuit parameters can be fabricated in the following procedure: specify the working point temperature, apply empirical models to estimate the junction fluence to correspond to this working point, use the working point fluence as the maximum dose, and scale the fluence of all other junctions to be equal to or less than the maximum based on the designed critical current ratio.

To compare the device physics of the BiSQUID against a "gold standard", two chips of 2-junction DC SQUIDs were fabricated: "SQgamma" and "SQcarly". In this work the junction exposure is written as a single pixel line dose of ions per nanometer. The tightly focused helium beam is scribed many times along a single line where effective dose is calculated from the beam spot (~1 nm), beam current (~0.5-1.0 pA beam current), and dwell time per pixel. A dose of 200 ions/nm (1 nm spot equivalent to 2.5e16 ions/cm^2) was delivered to all cells on "SQgamma" resulting in a 72-81 K operating range. A dose of 300 ions/nm (1 nm spot equivalent to 3.8e16 ions/cm^2) was delivered to all cells on "SQcarly" resulting in a 50-70 K operating range. Here operating range is defined as temperatures in which the SQUID peak-to-peak voltage is greater than 100 μV. The operating temperature of "SQgamma" was

sufficiently high ($T_C^{film} = 82\ K$) so as to exacerbate the effect of thermal fluctuations. Thus a range of critical currents and working point temperatures were used to compare BiSQUIDs to DC SQUIDs.

Seven different BiSQUID cells were fabricated using two different chips: six cells on "BiSQagnes" with the 3rd junctions dosed at roughly half the helium fluence of identical doses used on junctions 1 and 2, and one cell from "BiSQalpha" with all junctions dosed identically. In this way BiSQUID circuits with varied critical currents in the 3rd junction can be compared. All other cells are not considered in this work. All junctions in "cell 15" of BiSQalpha were written identically at 350 ions/nm (1 nm spot equivalent to 4.4e16 ions/cm^2). Three different dosage pairs were used in the six BiSQagnes cells, with the 3rd junction dose always lower than junctions 1 and 2 (Figure below). All cells in BiSQagnes are replicated except cell 12, which is unique. Note that a dose of approximately 100-150 ions/nm (1 nm beam) is required to reduce the junction T_C below the T_C^{film}. At doses lower than 100-150 ions/nm the critical current was reduced and the penetration depth increased creating a "Dayem Bridge".

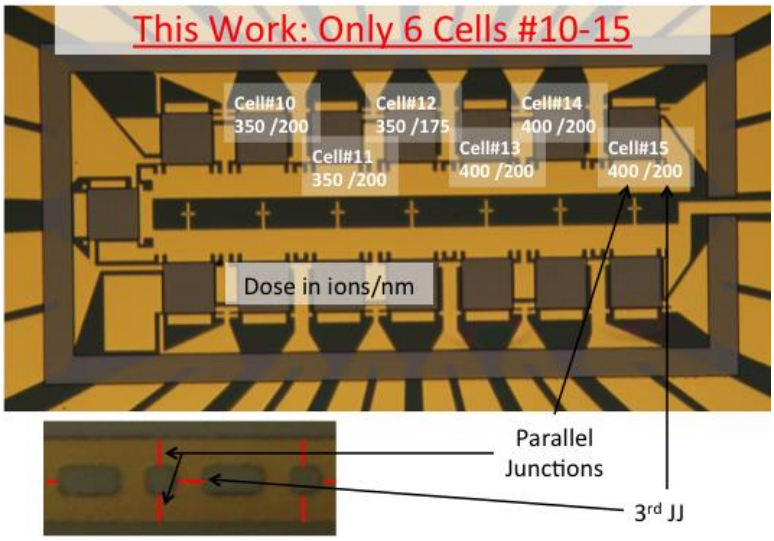

Figure 61: BiSQUID Chip "BiSQagnes": Layout of ion doses for the 6 BiSQUID cells considered in this work. Format: (Junction 1 and 2 dose)/(3rd junction dose). For a 1 nm diameter focused He ion beam, 1 ion/nm is 1.27e14 ions/cm^2

Basic Circuit Characteristics of BiSQUID Compared to DC SQUID

The Current-Voltage (IV) characteristic for the highest performance single cell of the DC SQUID variety is captured in the left figure below, in this case cell 12 at 52 K ("SQcarly", 50-70K operation). "SQcarly" is the main DC SQUID chip analyzed in this work. The IV curve of Cell 12 exhibits a $20\ \mu A$ critical current and a $135\ \Omega$ normal state resistance ($I_C R_N \sim 2.7\ mV$ or $\approx 32\ \mu V/SQUID$). The analog derivative of the IV curve (dynamic resistance) was simultaneously acquired using a small-signal lock-in technique (0.5 uA signal, technique discussed in chapter 3) and is displayed in the figure below right. The dynamic resistance is plotted versus the same voltage range as the IV curve to directly compare the dynamic resistance with the IV curvature. Note the largest dynamic resistance occurs just after the onset of voltage (just above Ic), where the dynamic resistance is larger than R_N. Two different bias regimes are present as measured by the steepness of the derivative: a very steep slope starting from the onset of the voltage state and a constant R_N at high bias. The

bias current range is selected to demonstrate the linear dynamic resistance "R_N" at high bias, which in this case onsets after 40 mV or about 0.47 mV/SQUID. The curvature of the IV curve near zero voltage (initial steep section below 5 mV) is a complex function of the thermal fluctuations [18] and the critical current parameter spread in the junctions (see following section). In general the collective behavior of the 84 DC SQUIDs in cell 12 are well described by the RSJ model.

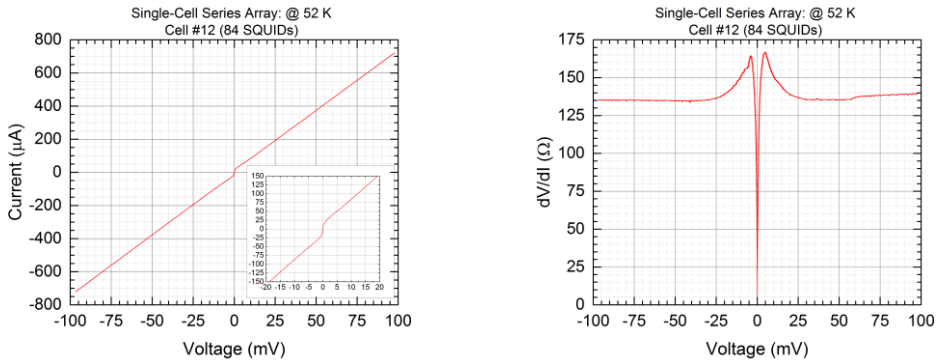

Figure 62: DC SQUID Chip "SQcarly": (left) IV characteristics for a single 84 DC SQUID series array pixel. (right) analog derivative of the IV curve

To examine the worst case scenario of junction parameter spread, we measured the IV characteristics of 6 BiSQUID cells in series (210 devices) in the Figure below (BiSQagnes). Note that Cells #10-11 are dosed with (350 || 200), Cell #12 dosed with (350 || 175), and Cells #13-15 are dosed with (400 || 200); see layout discussion above. The first number is the dose (ions/nm) applied to junctions 1 and 2, the second number is the dose applied to the third junction. Hence a measurement of dissimilar cells in series examines the device performance in the case of large parameter spread. Analysis of the parameter spread between BiSQUID Cells is presented later in this chapter. The IV characteristic is well described by the RSJ model except the presence of a continuous positive curvature at high bias. This curvature is evident from the

straddling of the RSJ fit (red line Left Figure) over the data (black line Left Figure). The BiSQUID junctions have similar parameters to the DC SQUID arrays, approximately $20\,\mu A$ critical current and $2\,\Omega/device$ maximum dynamic resistance at ~50 K. The larger current 3rd junction (half the dose of the 2 parallel junctions) does not appear to distort the RSJ-like behavior. Additionally, the dynamic resistance behavior closely matches Cell 12 of SQcarly with sharp peaking in the vicinity of I_C (maxima @ $\pm 50\,\mu A$) preceded by a smooth, monotonic increase. Thus the BiSQUID junctions are high quality and are comparable to the DC SQUID even in the contrived case of many different cells in series with different amounts of damage, thus direct comparisons between the SQUID and BiSQUID devices make sense.

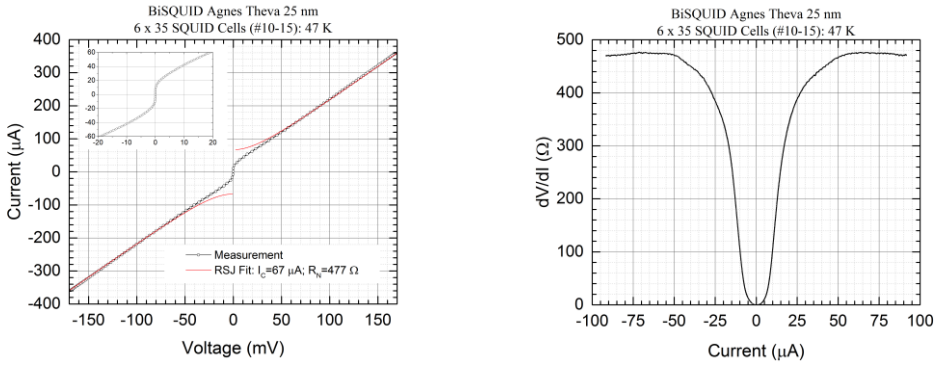

Figure 63: BiSQUID Chip "BiSQagnes" (left) IV characteristic for 6 BiSQUID cells with different damage levels in series-210 SQUIDs with 3 different doses. (right) dynamic resistance of the same data.

Interference Characteristics of BiSQUID Versus DC SQUID

In the presence of magnetic fields the critical current of a SQUID will oscillate such that the current swings between the zero field I_C (maximum, $n\Phi_0$ where n is an integer) and a diminished I_C (minimum, $\left(n+\frac{1}{2}\right)\Phi_0$). The maximum depth of the SQUID's current swing is a function of the modulation parameter $\beta_L = \frac{LI_C^{SQUID}}{\Phi_0}$, and is also dependent on the IV curvature. In the Figure below left,

the magnitude of the SQUID current modulation in the presence of magnetic field is measured as a function of current bias. First we measured the SQUID voltage modulation, then translated it into current modulation at a fixed voltage. The SQUID modulation parameter β_L can be estimated from the $\frac{\Delta I}{I_C}$ ratio using the work of Tesche and Clarke [20], where ΔI is the maximum height of the translated IV modulation in the left Figure below. In the case of SQcarly cell 12, the maximum current modulation occurs between $25\ \mu A$ and $50\ \mu A$ with insignificant current modulation ΔI for biases in excess of $100\ \mu A$ (Figure Below Left). SQcarly cell 12 appears to have current modulation less than 50% of the average I_C, hence this device must have an average modulation parameter of the series $\beta_L > 1$.

The depth of the critical current modulation as a function of magnetic field "$I_C(B)$ curve" can be captured using the voltage sample and hold technique described in chapter 3 (Figure below right). The extracted $I_C(B)$ traces for two different voltage thresholds are displayed in the figure below right for the Cell 12 of SQcarly. Note the presence of the overarching envelope from the junction magnetic interference "Fraunhofer pattern" (low frequency) superimposed with higher frequency SQUID oscillations with a single period $\Phi_0 = 27\ \mu T$. The current swing is deeper at the $50\ \mu V$ threshold (~1.7uV/SQUID) compared to the $250\ \mu V$ (~3.0uV/SQUID) threshold. A current modulation $\frac{\Delta I}{I_C} = 52\%$ for the $50\ \mu V$ threshold corresponds to a $\beta_L \sim 1$ (Tesche and Clarke), while a current modulation $\frac{\Delta I}{I_C} = 28\%$ for the $250\ \mu V$ threshold corresponds to a $\beta_L \sim 2.8$. In practice the SQUID is biased at the point of largest current modulation i.e. the lowest modulation parameter. Additionally, the

high threshold $I_C(B)$ SQUID oscillations are much more sinusoidal while the lower threshold $I_C(B)$ contains non-sinusoidal structure at the current minima. The presence of additional structure at the current minima most likely indicates that not all SQUIDs operate at the same working point. This result is consistent with the IV characteristic data for the critical current parameter spread in SQcarly cell 12. The form of the DC SQUID critical current modulation as a function of both field and working point bias is a general property of 2 junction SQUID devices.

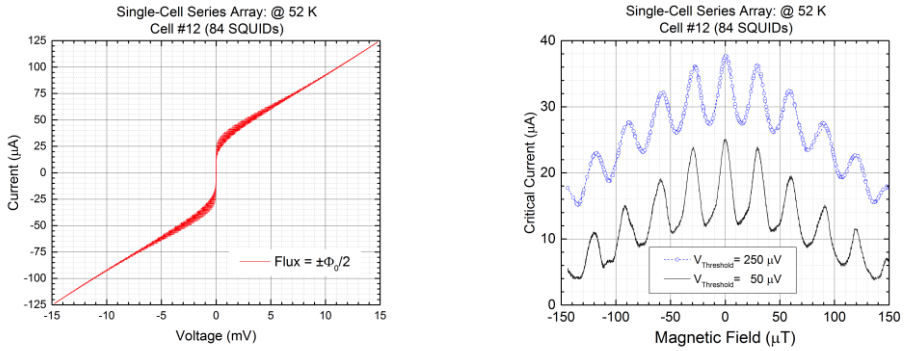

Figure 64: DC SQUID Chip "SQcarly" (left) Slowly swept IV characteristics of DC SQUID array in the presence of higher frequency magnetic field bias of magnitude equal to a single flux quantum. (right) Critical current as a function of magnetic field threading the DC SQUID array for two different working points.

The magnetic interference pattern of the 6 BiSQUID cells (#10-15) are displayed in the Figure below. Each cell was measured independently with all $I_C(B)$ voltage thresholds set to 10 μV. Note that the magnetic field offsets have not been corrected, and a uniform field offset ~3 μT is present for both current polarities (not shown) which is equal to the typical remnant field passing through the magnetic shielding. Thus any phase offsets from the interactions of the screening currents [68] between the two BiSQUID loops appear negligible over a range of circuit parameters. The period of the current oscillations is identical for all cells. Significant critical current variation is apparent, as the maximum I_C does not closely match the junction dose. It is likely that the cell-to-cell variations are related to errors in pattern alignment and focusing procedures during junction writing. Hence through cell-to-cell variations we have six substantially different BiSQUID circuits to compare with standard DC SQUIDs.

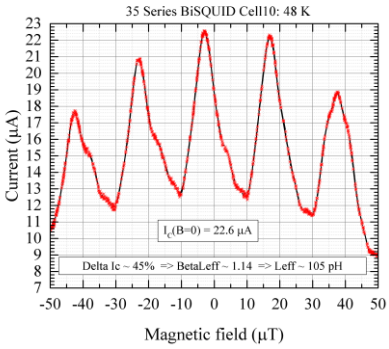

350 $dose$: 22.5 μA ⇒ I_C^{3rd}~40 μA

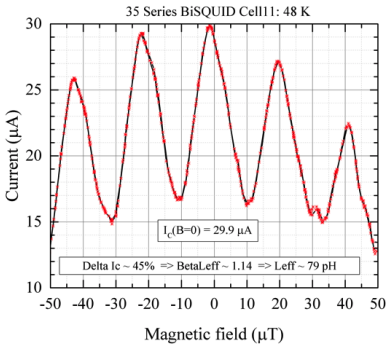

350 $dose$: 30.0 μA ⇒ I_C^{3rd}~53 μA

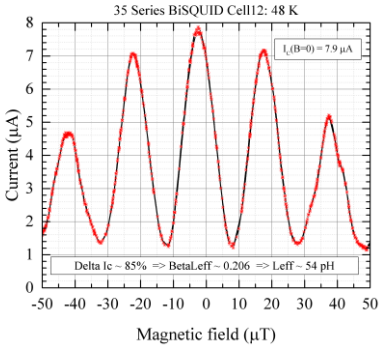

350 $dose$: 7.75 μA ⇒ I_C^{3rd}~14 μA

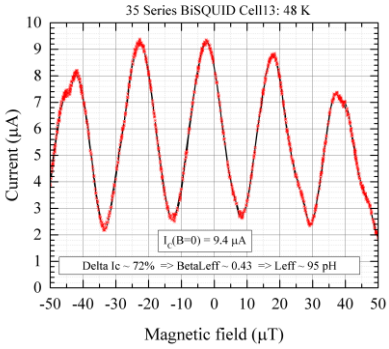

400 $dose$: 9.25 μA ⇒ I_C^{3rd}~40 μA

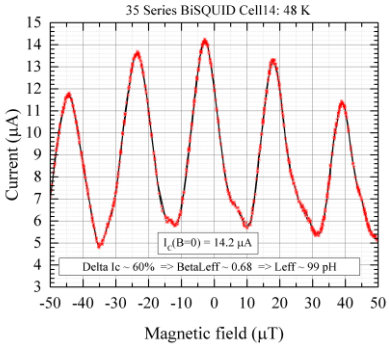

400 $dose$: 14.0 μA ⇒ I_C^{3rd}~61 μA

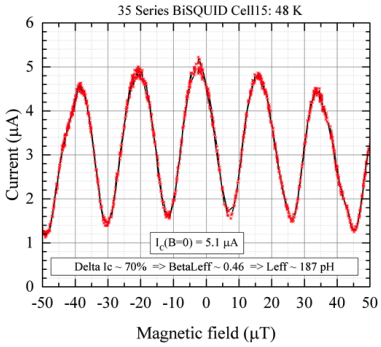

400 $dose$: 5.0 μA ⇒ I_C^{3rd}~22 μA

Figure 65: BiSQUID Chip "BiSQagnes": Critical current as a function of magnetic field for each of the 6 individual BiSQUID cells used in the 6 cell series. The dose of 30 keV helium is displayed in the form (2 parallel junctions || 3rd junction) with units ions/nm: #10-(350 || 200), #11-(350 || 200), #12-(350 || 175), #13-(400 || 200), #14-(400 || 200), and #15-(400 || 200). A coarse estimate 3rd junction critical current is labeled for each device.

One difficulty in characterizing BiSQUIDs is the inability to directly measure the critical current of the 3rd junction as it is chosen to be higher than the other two. A semi-quantitatively estimate the BiSQUID 3rd junction critical

current can be made from the $I_C(B)$ data by scaling the maximum I_C (junctions 1 and 2 in parallel) by the ratio of dose for the 3rd junction versus junctions 1 and 2. Cybart et. al. [47] have previously demonstrated a ~50 K difference in the $I_C \approx 1\ \mu A$ operating temperature for helium ion damage junctions with a 300% different dose. In proximity effect junctions, the junction critical current is exponentially dependent on the junction T_C with a power law contingent on properties of the junction barrier [46]. In this work the critical temperature of the 350 and 400 dose junctions was 60 K and 52 K, respectively. Simple scaling of dose to T_C is confirmed here ($\frac{350\ ions/nm}{400\ ions/nm} \sim \frac{52K}{60K}$). However following this simple scaling, the T_C of the half dose 3rd junctions would be $\sim T_C(175\ dose) = \frac{350}{175} * 60K = 120\ K$ and $T_C(200\ dose) = \frac{400}{200} * 52K = 104K$, with both exceeding the electrode $T_C = 82\ K$. Hence the 3rd junctions might be behaving like Dayem bridges [82], with a T_C identical to the film and a reduced critical current compared to an undamaged bridge. In this work we only have data for 200 dose junctions from the properties of the 200 dose SQgamma devices, which exhibited a $T_C = 80\ K$. Thus we estimate a $T_C = 80\ K$ for the 200 dose junctions, and assume $T_C = 82\ K$ (bulk film T_C) for the 175 dose junctions. Assuming a S-N-S proximity effect model $I_C(T) \propto \left[1 - \left(\frac{T}{T_C}\right)^2\right]$ [46], we coarsely estimate the 3rd junction currents by scaling the maximum I_C for each cell (Figure Above). These estimations are extremely coarse, at most serve as a rough guide for comparison.

Since the Josephson inductance is inversely proportional to junction I_C, the largest inductance change per flux quantum should occur in the circuits with the largest 3rd junction I_C. Large inductance change in the 3rd junction per

flux quantum should result in strong nonlinearity compensation. The smallest 3rd junction I_C's are estimated for Cells 12 and 15, where a highly regular, sinusoidal behavior is observed in both cases. Cells 10, 11, 13, and 14 are estimated to have very similar 3rd junction I_C's, and there are strong similarities in the $I_C(B)$ behavior for these devices. Cells #10, 11, 13, and 14 have sharpened current oscillations compared to the sinusoidal DC SQUID, indicating the presence of higher frequency oscillations.

BiSQUID Cell #12 behaves most closely to a standard DC SQUID device. BiSQagnes Cell #12 was patterned with the smallest dose in the 3rd junction hence is the closest Cell design to a standard DC SQUID circuit. The most nonsinusoidal oscillations (and lowest current modulation) are observed in Cells 10 and 11, where irregular curvature (Figure Above) and small modulation depth are normally indicators of significant mutual inductance effects within the SQUID array [65]. Irregular curvature at the $I_C(B)$ minima was observed in the DC SQUID for low $I_C(B)$ voltage thresholds, thus irregularities near the minima are not specific to the BiSQUID. Generally the structure at the $I_C(B)$ minima will be dominated by a distribution of critical currents within the series array. Hence the primary difference of the BiSQUID compared to the DC SQUID in the $I_C(B)$ characteristics appears as a sharpening of the $I_C(B)$ magnetic interference pattern.

Voltage-Field Characteristics of BiSQUID Versus DC SQUID

The Voltage-Field (VB) characteristic of SQcarly Cell #12 (84 series DC SQUIDs) is displayed at optimal current bias in the Figure below (Top Left). The analog derivative ($\frac{dV}{dB}$) of the same Cell #12 VB curve acquired using a 0.2 μT

modulation is displayed; method described in Chapter 3 (Top Right). Optimal current bias in this case is defined as the current required to maximize the Field-to-Voltage transfer function ($\frac{dV}{dB}$ in Volts/Tesla) at the $\frac{\Phi_0}{4}$ working point. The peak-to-peak voltage (Vpp) of the central VB oscillation is 1.15 mV, corresponding to approximately 13.7 μV/SQUID if all series SQUIDs contribute equally. Vpp signals of at least 100 μV were observed over a wide range of temperature (50-70 K). A remarkably high field-to-voltage transfer function of $\frac{dV}{dB}$ ~125 Volts/Tesla (1.5 V/T/SQUID) is observed at $\Phi = \frac{\Phi_0}{4}$, compared to a high quality single SQUID with Helium ion damage junctions of ~25 V/T at 50 K [83]. No significant field offset is observed in the central VB oscillation between positive and negative current biases. Hence the SQUID devices constructed in this work are high quality and non-hysteretic.

Only one regular frequency of oscillation is observed in both the VB and $\frac{dV}{dB}$ indicating the consistency of the SQUID period and hence uniformity of the effective area for all 84 SQUIDs in the series array. Small distortions of the sinusoidal response are apparent in the $\frac{dV}{dB}$, but are too irregular to infer the presence of higher frequency oscillations that could indicate flux-trapping effects. The junction Fraunhofer pattern does add a linear component to the central SQUID oscillations (Top Right and Bottom Right) to the otherwise sinusoidal $\frac{dV}{dB}$. In this case the Fraunhofer pattern is symmetric about zero field implying a uniform current distribution through the junction barrier (see Chapter 1). At least three oscillations of the junction magnetic interference pattern are present with a period ~250 μT, indicating high quality junctions of bridge width 4 μm in the thin film limit ($\Delta B_{Junction} \sim 1.84 * \frac{\Phi_0}{width^2} = 238\ uT$) [15].

Note that the SQUID oscillations persist for at least 40 flux quanta superimposed on the junction Fraunhofer. Above all no horizontal portion of the $\frac{dV}{dB}$ is observed for signals as small as 0.2 μT (0.7% of Φ_0). Thus the VB of a standard DC SQUID is almost purely sinusoidal except for the contribution of the junction Fraunhofer pattern i.e. DC SQUIDs are not linear.

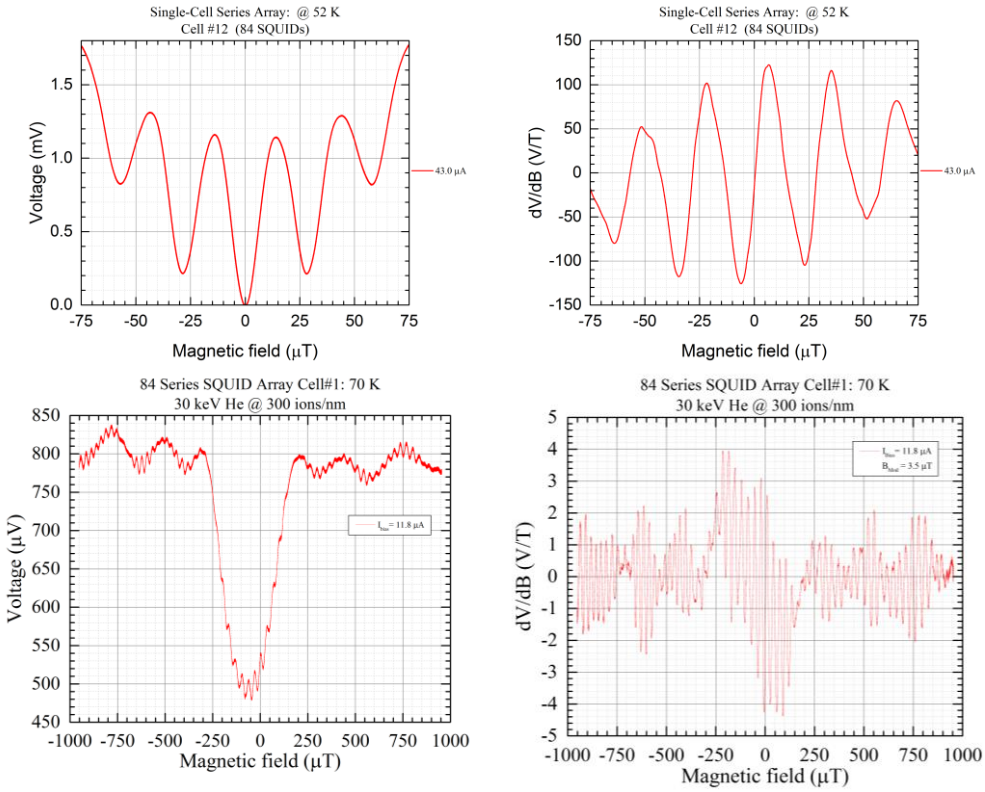

Figure 66: DC SQUID Chip "SQcarly": (Top Left) Field-to-Voltage (VB) characteristic of Cell 12 at optimal current bias, field and voltage offsets removed. (Top Right) Analog derivative ($\frac{dV}{dB}$) of the same Cell 12 VB data with a 0.2 μT modulation. (Bottom Left) Cell #1 VB over a large magnetic field range demonstrating short junction Fraunhofer and superimposed SQUID oscillations. (Bottom Right) $\frac{dV}{dB}$ of the same Cell #1 data with 5 μT probe signal.

The most straightforward BiSQUID circuits to fabricate are designs with identical critical currents in all 3 junctions i.e. junctions patterned with identical ion doses. One such device is Cell 15 of "BiSQalpha" where the IV and VB characteristics are displayed in the Figure below. VB characteristics for a range of current biases up to the maximum peak-to-peak voltage are shown. Two distinct periods are apparent: large voltage 36 μT and minor voltage ~18 μT . We ascribe the 36 μT oscillations to the 3-junction BiSQUID loop (5 μm x 5 μm), and the 18 μT oscillations to the 1-junction loop (5 μm x 10 μm) exhibiting the smaller voltage signal centered on $\frac{\Phi_0}{4}$. Since the 3rd junction

cannot directly contribute to the series voltage, the faster voltage oscillations must be the result of flux shuttling between the 1 junction BiSQUID loop and the 3 junction loop. In this way flux is ejected from the 3 junction loop to maintain the flux quantization condition for both loop areas, hence a series voltage is produced for both loops. Most importantly, the linearity of the BiSQUID is significantly decreased compared to standard SQUIDs when the 3rd junction of the BISQUID I_c is equal to junctions 1 and 2.

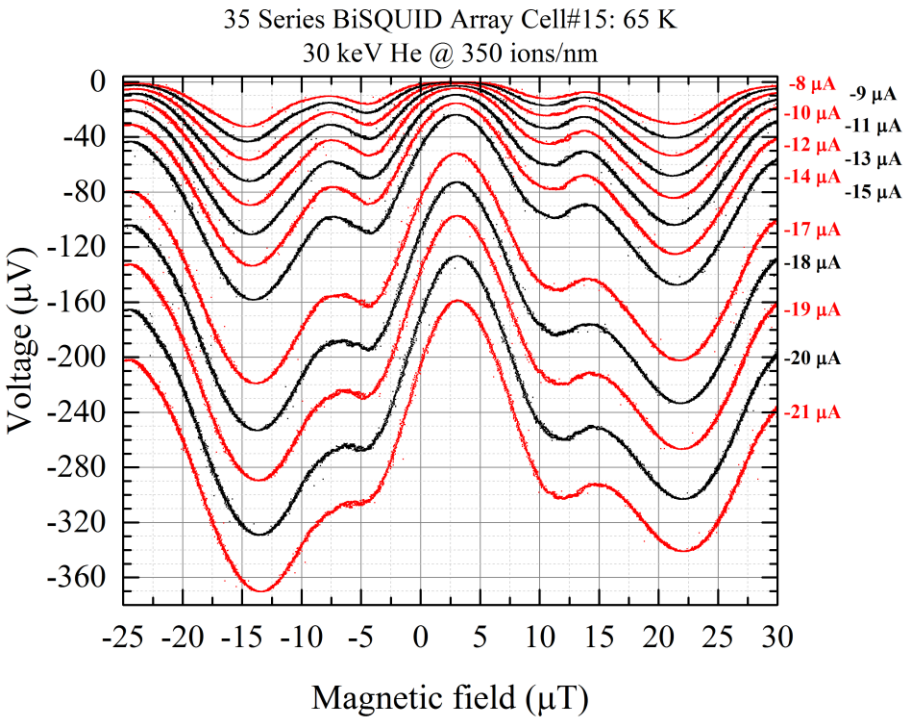

Figure 67: BiSQUID Chip "BiSQalpha": (left) IV characteristic of single cell of 35 series BiSQUIDs with equal helium fluences of 350 ions/nm or 4.46e16 ions/cm^2 applied to all 3 junctions. (right) VB characteristic for many current biases of cell 15.

Effects of Critical Current Parameter Spread

For best performance SQUID arrays require uniformity and accuracy in the circuit parameters. Deviations in the circuit parameters within a SQUID

array, in particular the critical currents, are most evident in the derivative of the IV characteristics and the magnetic modulation of the IV.

A perfect RSJ SQUID device would have a concave nonlinear IV at finite V in the vicinity of I_C which transitions monotonically to a linear resistance. Analysis of the fine structure in the dynamic resistance near I_C is an effective measure of the critical current uniformity within the series array. In the Figure below, the dynamic resistance as a function of bias current is shown for Cell #12 of SQcarly (84 DC SQUIDs). The first deviation from RSJ behavior is the finite resistance at all current biases, indicating that not all devices in the series are in the zero voltage state at the operating temperature i.e. a minority population of diminished junction T_C's. A lack of distinct structure is present for currents less than $50\ \mu A$. More importantly, the insets in the figure below showcase a fine structure from $50 - 150\ \mu A$ that we attribute to differing critical currents for devices within the array i.e. critical current parameter spread.

As the current bias is increased from zero to finite voltage, the dynamic resistance will increase then slowly decrease creating a dynamic resistance "peak". Hence each peak in the dynamic resistance can correspond to an individual I_C. In practice each junction within the array will experience thermal fluctuations that will broaden the dynamic resistance peaks. However, we note that these fluctuations are small ($2.2\ \mu A$ at 52 K) compared to $I_C \geq 20\ \mu A$ of SQcarly Cell 12. The asymmetric structure of the bumps about zero current most likely indicates that multiple processes are present, where bumps that are symmetric about zero current bias are direct evidence of individual critical currents. In general it is difficult to make more precise determinations, however here we assume each symmetric bump in the dynamic resistance as a

function of current corresponds to an individual critical current. In short, we attribute the finite resistance at all biases (lack of a zero voltage state) and the dynamic resistance structure in the range of $50 - 150\ \mu A$ to variance in the circuit parameters. Cell #12 SQcarly is well-described by the RSJ model without correction for parameter spread, hence the variance observed belongs to a minority of outlier devices within an otherwise tight variance of parameters in the series array.

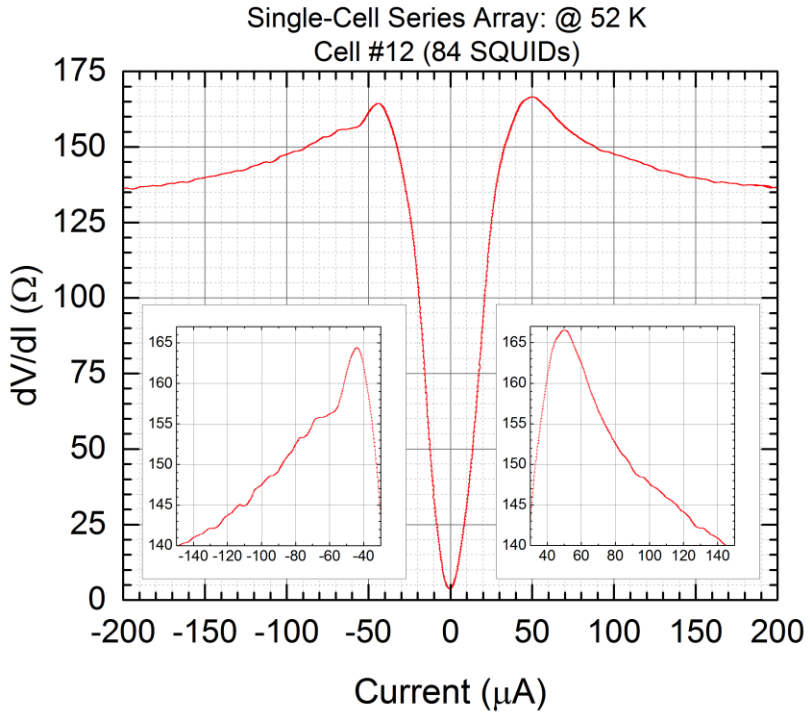

Figure 68: DC SQUID Chip "SQcarly": Dynamic resistance of Cell#12 containing 84 DC SQUIDs in series. (insets) Same data zoomed into the vicinity of Ic

Now we consider DC SQUID devices with significant parameter variations to further demonstrate this point. The dynamic resistance (0.5 μA AC bias) is plotted as a function of bias current for 2 adjacent cells (cells 1 and 13) in the Figure below. The IV characteristics (below figures left) are very different between cells despite the attempted identical patterning parameters. Cell #1

appears to have an extended IV concavity in the vicinity of I_C i.e. significantly rounded IV. In the below figure right, the dynamic resistance of cell #1 contains significant structure both above and below the average I_C. The structures are coarsely symmetric about zero current. Note the significantly elevated current (here $700\ \mu A$ and before $50\ \mu A$) compared to cell 12 required to reach a diminished global resistance maxima (here $\approx 76\ \Omega$ and previously $\approx 165\ \Omega$). We attribute these structures to a significantly increased critical current parameter spread in cell 1 compared to cell 12, with $I_C \leq 120\ \mu A$ for the majority of devices in cell 1. Here the fraction of deviant devices is coarsely estimated by the ratio of the dynamic resistance plateaus enclosing the rounding, $45\ \Omega$ out of $76\ \Omega$ or roughly $60\ \%$ of devices, assuming each series device contributes approximately the same resistance when biased above I_C. Cell 13 also exhibits an even larger critical current spread compared to cell 12 including: a diminished dynamic resistance maxima (here $\approx 100\ \Omega$ and cell 12 $\approx 165\ \Omega$), lack of a zero voltage state, and also appears to have a greater asymmetry than either cell 1 or 12. Hence a moderate critical current parameter spread will tend to round the IV near I_C and decrease the maximum IV slope.

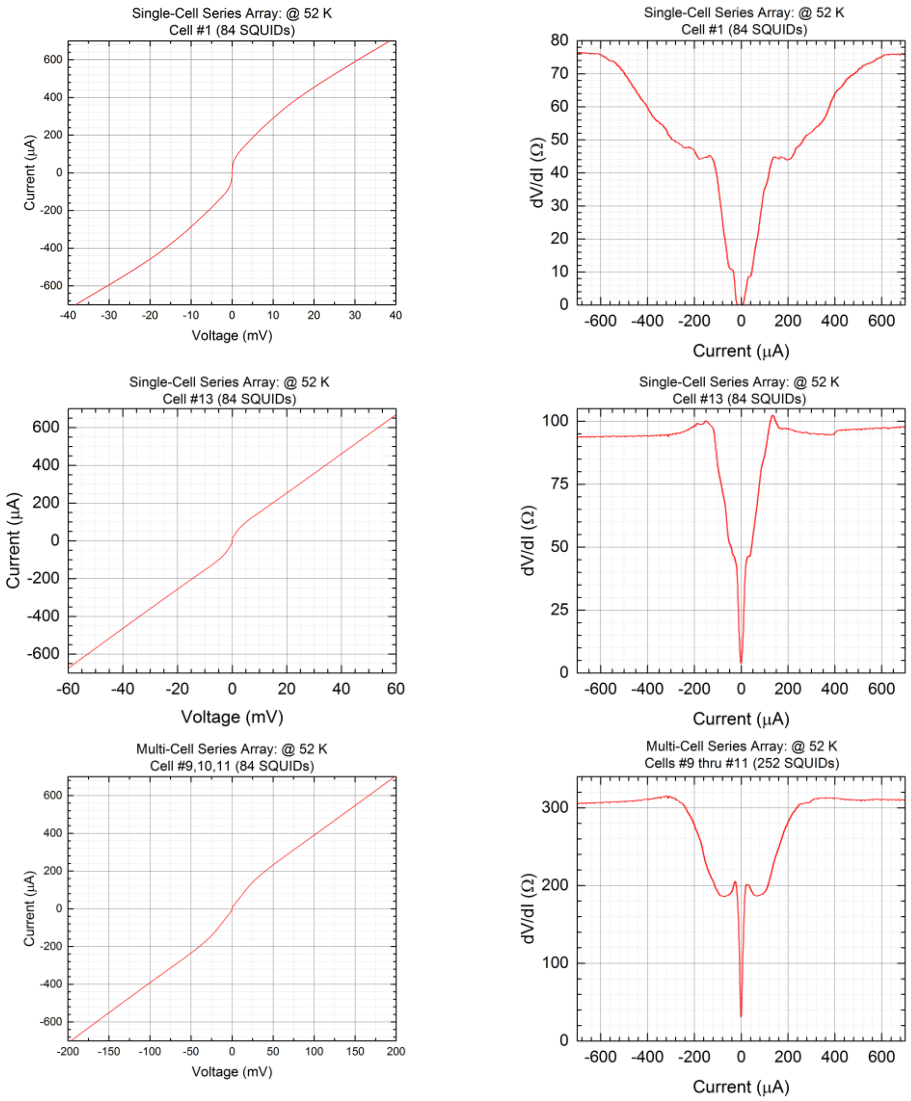

Figure 69: DC SQUID Chip "SQcarly" (top panels) IV and dynamic resistance of Cell #1 demonstrating a wide range of critical currents within the 84 DC SQUID array. (Middle panels) IV and dynamic resistance of Cell #13 (Chip A) which is directly adjacent to Cell #12. (Bottom panels) IV and dynamic resistance of 3 cells connected in series (#9,10,11).

Now we consider the parameter spread by linking 3 Cells in series (#9,10,11) for a total of 252 SQUIDs(see figure above, bottom panels). The combined array appears to contain two fairly distinct RSJ-like curves in the dynamic resistance with prominent peaking at $27\ \mu A$ and $310\ \mu A$. A simple rescaling of the $0 - 27\ \mu A$ curve reproduces the basic features of the $310\ \mu A$

peak. Thus large variation occurs when comparing different Cells, where modest critical current parameter spread exists for individual Cells. Greater variation between cells points towards larger variations in the patterning process associated with stage movement and focusing between Cells, rather than process drift during an individual Cell patterning. Above all, these results indicate that further work is required to identify the sources of variation to further improve device uniformity.

To further elucidate the critical current parameter spread between cells, all 4 configurations (#12,#1,#13, and #9-11) are directly compared (Figure below). All 4 IV characteristics are distinct with different I_C and R_N, and simple scaling of Cells #9-11 cannot perfectly match any of the single cells. Two properties are immediately evident from the dynamic resistance comparison: first, all cells appear to have similar peaking between $20 - 50\ \mu A$, and secondly the magnitude of the dynamic resistance significantly differs. The width of the structure in the vicinity of the critical current transition appears to be very sensitive to differences in SQUID critical currents and normal state resistances within the series array. Intuitively, an increased number of series devices will tend to smooth out the detailed fine structure of the dynamic resistance near I_C indicating precise determination of parameter spread is difficult in very large arrays. Nevertheless the performance of all 4 cell configurations is noteable, the resistances are much higher than ion masked Josephson junctions and the IV characteristics are well described by the RSJ model.

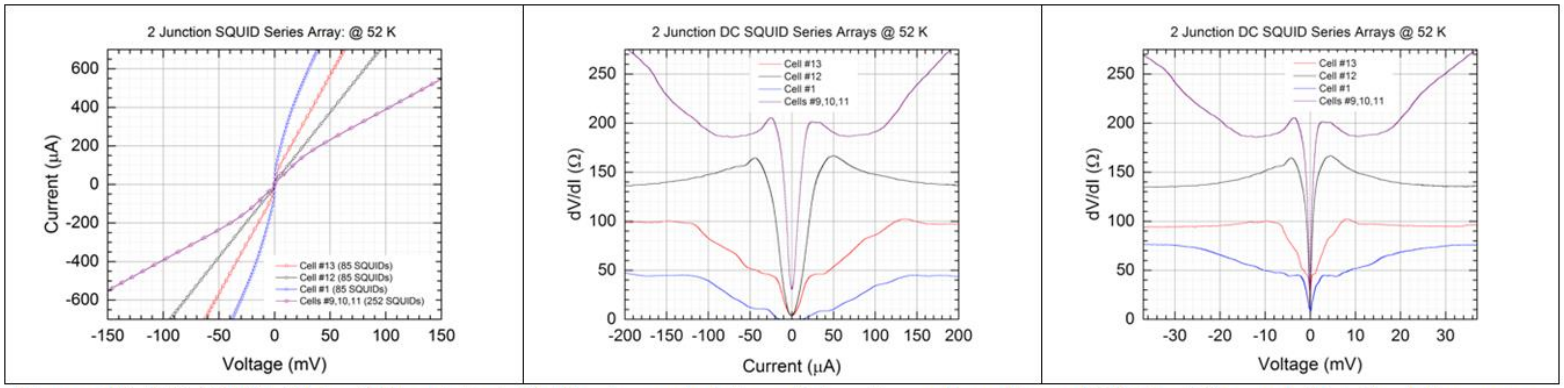

Figure 70: DC SQUID Chip "SQcarly": (left) IV characteristics of 4 cell configurations (#12,#1,#13, and #9-11) at the same temperature. Small signal dynamic resistance as a function of current (center) and voltage (right) for the same 4 cell configurations.

Now we have the tools to consider the parameter spread in each of the 6 BiSQagnes Cells (#10-15) (Figure below). The IV curves are very similar, with R_N nearly equal for all Cells. At first glance the 6 BiSQUID cells appear to perform better than the DC SQUIDs, however this might be expected from the smaller number of devices in series: 35 BiSQUIDs or 105 junctions per cell compared to 84 DC SQUIDs or 168 junctions per cell. Critical current spread is obvious in the zoomed IV (Below Right), with the lowest I_C occurring when all 6 cells are linked in series. One of the most useful aspects of a series array is the effective up-scaling of small voltages. For instance a 100 nV single SQUID signal would be difficult to resolve, but an array of 100 duplicate devices maintains the same curvature with 100 times the signal. Thus we attribute the "lowered" I_C of the 6 cells linked in series to the effective "magnification" of small voltages in the vicinity of I_C. SQUID arrays are much more useful in the study of small SQUID signals, particularly in the presence of thermal fluctuations.

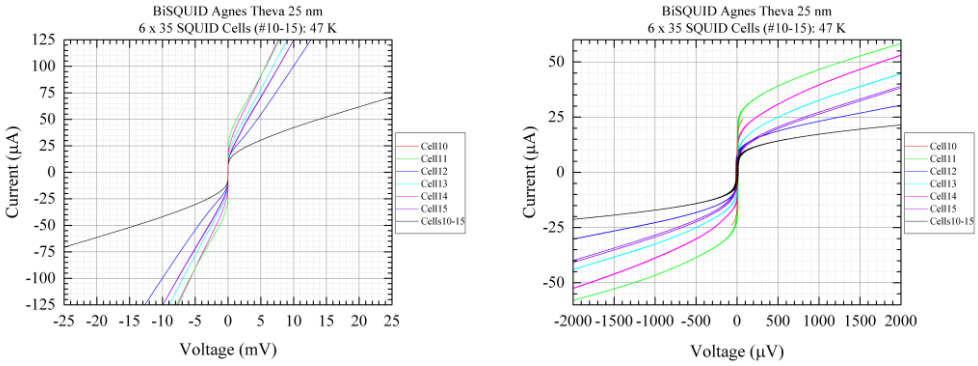

Figure 71: BiSQUID Chip "BiSQagnes": (left) Large bias range IV characteristics for 6 individual BiSQUID cells and all six in series. (right) Zoomed IV characteristics from the left panel focusing on the vicinity of Ic.

Both the DC SQUID and BiSQUID devices are well described by the RSJ model with an increased rounding of the IV in the vicinity of I_C due to critical current parameter spread. However a larger range of critical currents should

have been present in BiSQagnes based on the significant range of patterning doses (350-400 ions/nm). It is possible that a significant parameter spread is present between cells, but occurs in such a way as to cluster the circuit parameters around an average of the junctions with different fluences. More likely the lack of direct correspondence between pattern doses and BiSQUID critical current indicates the present limit in our patterning accuracy and precision. Thus both DC SQUID and BiSQUID devices were successfully constructed with RSJ junctions that behave similarly enough for direct comparisons, though variations between BiSQUID Cells is much smaller than the DC SQUID Cells in these devices.

The small-signal dynamic resistance dV/dI (310 nA excitation) of 4 different BiSQagnes cells is displayed in the Figure below. Three of the cells appear to be very similar (#11,13,14), while cell #12 stands out with both a higher resistance and uniformity. Note that cell #12 was the cell with the lowest dose applied to the 3rd junction: 175 ions/nm or approximately 2.22e16 ions/cm^2. Significant fine structure is present for cells #11, 13, and 14 for biases both above and below the maximum dynamic resistance peak. Compared with the DC SQUID cells, the fine structure of BiSQUID cells #11, 13, and 14 are more pronounced as anticipated from the smaller number of series devices. The dynamic resistance of cells #11, 13, and 14 appear to be very tightly grouped as expected from the IV characteristics. The dynamic resistance of the stand-out BiSQagnes Cell #12 is extraordinarily smooth, with a peak magnitude in the range of 25 μA exceeding what was observed for all 6 cells strung together in series (larger slope). The BiSQagnes cell 12 dynamic resistance also peaks at lower current and voltage than any other device,

(within 20 μA of Ic). Hence BiSQagnes Cell #12 appears to be the most uniform device out of all BiSQUID and DC SQUID chips in this work. Though, the ratio of the maximum dynamic resistance to the asymptotic dynamic resistance (R_N) at high bias is nearly a factor of two, much larger than any DC SQUID device behavior. Since BiSQagnes cell #12 was the only device exhibiting this characteristic, it is difficult to directly attribute strongly peaked dynamic resistance near I_C to the BiSQUID design. However the very low 3rd junction dose would be expected to induce only minimal damage, which separates the design of Cell #12 from all other BiSQUIDs characterized here. A large dynamic resistance is highly favorable for any SQUID device, consequently we would expect the increased voltage to flux transfer function from BiSQagnes Cell #12 compared to the BiSQagnes Cells #11, 13, and 14.

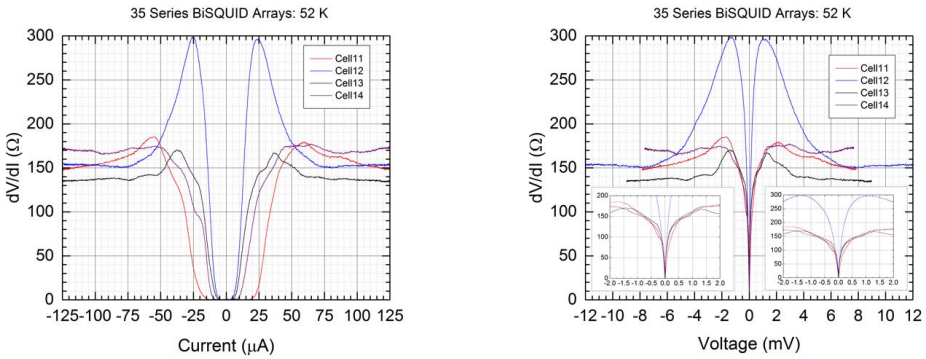

Figure 72: BiSQUID Chip "BiSQagnes": (left) Small signal dynamic resistance as a function of current. (right) Same data as a function of voltage, with insets zoomed into the low bias region.

An additional effect of parameter spread in a series SQUID array is to change the shape of the SQUID current modulation to when a single flux quantum "IVmod curve" is applied (Figure Below). Direct comparison of current modulation in SQcarly Cell #12, #13, and #9-11 at the elevated temperature of 65 K is shown in the Figure below. Note that the voltage offset

has been removed at zero field bias. The critical current of Cell #12 at 65 K is ten times smaller than at 52 K, where complete current modulation of the IV is evident in a single flux quantum. The largest current change (vertical distance) for Cell #12 at 65 K is quite small (2-4 μA), just larger than the thermal currents (2.2 μA). In the range of 0-5 μA Cell 13 is resistive and insensitive to a flux quantum, with the onset of magnetic field sensitivity for currents greater than 8 μA. Thus not all devices in Cell 13 are superconducting at 65 K, however those that are possess an $\overline{I_C} \approx 15\ \mu A$ with a larger $I_C R_N$ product than Cell 12. Lastly, the triple Cell series array (#9,10,11) behaves similarly to Cell #13, in that a portion of the devices within the series are not superconducting at the bias temperature due the lack of a zero voltage state and the delayed onset of magnetic field sensitivity ($I_{bias} > 15\ \mu A$).

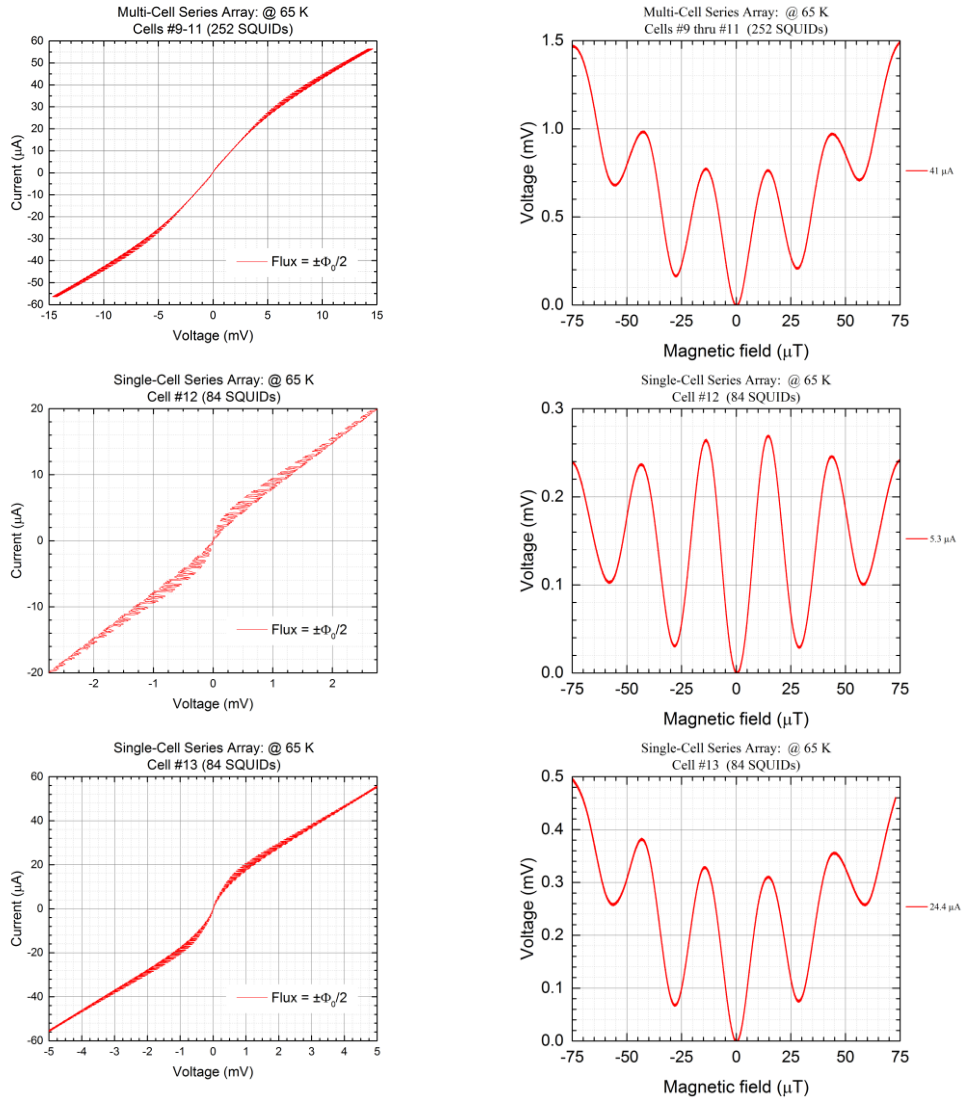

Figure 73: DC SQUID Chip "SQcarly": Magnetically modulated IV "IVmod curve" and optimal SQUID bias VB for: (top) three cells of 84 DC SQUIDs in series for a total of 252 SQUIDs in series. (middle) Cell 12. (bottom) Cell 13. Same chip as the 52 K measurements.

Discussion

If the linearization of the BiSQUID Voltage-Field (VB) characteristic is possible, then the linearity should be a function of the BiSQUID inductance and the ratio of the 3rd junction critical current to junctions 1 and 2. The kinetic energy of currents passing through a zero voltage Josephson junction can be

modeled as an inductive energy $E = {}^{1}/_{2}\, L_J I^2$, thereby defining a Josephson inductance $L_J = \frac{\Phi_0}{2\pi I_C cos\phi}$ where ϕ is phase difference across the junction. The Josephson inductance describes the kinetic energy stored in the carriers flowing through a Josephson junction under an AC current bias in the zero voltage state. The Josephson inductance is current dependent by the first Josephson relation $I = I_C sin\phi$, with increasing inductance at currents near I_C. In a symmetrically constructed BiSQUID only magnetically induced currents will flow through the 3rd junction. Hence the 3rd junction behaves as a flux dependent nonlinear inductance in the opposite polarity of the standard SQUID nonlinearity. The question remains whether the 3rd junction nonlinearity can adequately compensate for the intrinsic SQUID nonlinearity since none of the devices were linearized in this work [79]. Numerical simulations by Kornev have shown that linearization of the VB in low inductance BiSQUIDs occurs when the 3rd junction critical current I_{C3} is slightly larger than the critical current of the other two (identical) junctions $I_{C1,2}$ [80]. Both the magnitude and linearity of the BiSQUID field to voltage transfer function are strongly dependent on the circuit parameters, where transfer function linearity decreases exponentially as I_{C3} is changed from the ideal point as defined by Kornev [80].

No linearity enhancement has been observed for the 7 BiSQUID devices considered in this work, and in the framework of Kornev it is possible that the 3rd junction critical currents were outside of the optimal range. In particular, Kornev's model predicts that the optimal 3rd junction current would be larger than $I_{C1,2}$ (junctions 1 and 2) but smaller than $1.5 * I_{C1,2}$ in the low inductance limit. For 3rd junction currents much larger than $I_{C1,2}$ the BiSQUID

behaves similarly to a DC SQUID i.e. not enough inductance compensation. For 3rd junction currents equal to $I_{c1,2}$ the BiSQUID behaves like two coupled SQUIDs i.e. too much inductance compensation. Qualitatively, the VB characteristics of two series coupled SQUIDs superimpose like two terms in a cosine Fourier series. Using Fourier analysis it is possible to create a "linearized" VB near $\Phi = \frac{\Phi_0}{4} + n * \frac{\Phi_0}{2}$, when the frequency and amplitude of the two SQUIDs are optimized. However, in practice only a narrow range of Fourier coefficients produce a linear working point. Hence the optimal range of BiSQUID circuit parameters producing a linearized VB is probably quite narrow. It is also intuitive that greater nonlinearity will be created when strong compensation exists with the non-optimal circuit parameters. Hence examination of the BiSQUID performance must also be accompanied by circuit parameter spread analysis.

A summary of the all the BiSQUID properties is displayed in the table below. The most stark difference in the magnetic field response of BiSQUIDs compared to DC SQUIDs is the increased effective area of the BiSQUID. The period of the standard SQUID SQcarly is $\approx 50\ \mu T$, identical junction BiSQalpha period $\approx 36\ \mu T$, and BiSQagnes average period $\approx 18.5\ \mu T$. In fact, the BiSQagnes effective area most closely corresponds to the sum of the areas from both loops. The 3rd junction acts as the lowest energy flux jump site for the BiSQUID 1-junction loop, creating a flux shuttling action between the 3 junction and the 1 junction loops [73]. In this work it appears as if the fluxoids between the two BiSQagnes loops are tightly coupled when the connecting 3rd junction I_C is large. What is unclear is why the period of BiSQalpha with small 3rd junction I_C is intermediate between a standard SQUID and BiSQagnes. If the potential

barrier to flux entry was simply proportional to critical current, then small 3rd junction I_C should actually couple the two loops more tightly. One potential clue lies in the higher operating temperature of BiSQalpha (65 K) compared to BiSQagnes (47 K). It is possible that the greater magnetic field penetration of the thin film at 65 K diminishes the interloop coupling. For all our SQUIDs reported, We estimate the effective penetration depth $\Lambda_{eff} = \frac{\lambda_L^2}{thickness} \sim 1.4 - 1.7\ um$ from 50-60 K using the Gorter-Casimir model ($\lambda_L(T) = \frac{\lambda_L(0)}{\sqrt{1-\left(\frac{T}{T_C}\right)^2}}$) assuming $\lambda_L(T=0) = 175\ nm$). Thus even at the temperature of BiSQagnes the 4 micron wide electrodes ($\frac{width}{2} < 2\lambda_L$) are fully penetrated by magnetic fields and the critical current of the electrodes are expected to be strongly field dependent. Nonetheless, all BiSQUIDs measured here are intrinsically more sensitive than the equivalent standard SQUID.

Table 3: Summary of device performance for BiSQUID Chip "BiSQagnes"

Device	Cell 10	Cell 11	Cell 12	Cell 13	Cell 14	Cell 15	Cells 10-15
SQUID I_C (uA)	22.6	22.9	7.9	9.4	14.2	5.1	5.5
Array R_N (Ω)	46	63	101	72	61	80	394
Array I_CR_N (uV)	1040	1443	798	677	866	408	2167
SQUID I_CR_N (uV)	30	41	23	19	25	12	10
Josephson Penetration Depth (um)	4.859	4.827	8.218	7.534	6.13	10.23	9.849
Eff BetaL	1.14	1.14	0.206	0.43	0.68	0.46	0.25
Eff L (pH)	105	79	54	95	99	187	94
Period (uT)	19.1	18.0	19.7	18.9	17.9	17.6	20.4
Aeff (um2)	10.42x10.42 (5+2.7)x14.1	10.74x10.74 (5+2.7)x14.98	10.26x10.26 (5+2.7)x13.67	10.45x10.45 (5+2.7)x14.18	10.75x10.75 (5+2.7)x15.01	10.84x10.84 (5+2.7)x15.26	10.07x10.07 (5+2.7)x13.17
V Peak-to-Peak (uV)	227	249	685	318	198	282	1350
dV/dB (V/T)	36	45	97	55	34	53	200
V P-P /SQUID (uV)	6.49	7.11	19.57	9.09	5.66	7.2	6.43

Since the BiSQUID linearization is apparently so sensitive to the circuit parameters, we must consider the effect of thermal fluctuations on circuit parameters. For DC SQUIDs with model-like resistively shunted junctions, the maximum transfer function occurs at current biases within 50% of the SQUID I_C [20]. Hence any SQUID array that exhibits an optimal working point (maximum transfer function) at a current bias significantly greater than 1.5 I_C most likely indicates the existence of a range of critical currents within the series array. Only BiSQagnes Cell #11 is ideally biased within 50% of I_C, with the remaining cells demanding significantly more current (2-4 times I_C). This result corroborates the parameter spread discussion in the previous section and has been observed in very large arrays [33][84]. A standard SQUID in the thermally dominated limit will also require bias currents larger than I_C for maximum

voltage modulation (Figure Below). The SQUID effective thermal parameter ($\Gamma = \frac{2\pi k_B T}{I_C^{SQUID} \Phi_0}$ unitless) is defined as the ratio of the magnetic energy per flux quantum ($\frac{\Phi_0^2}{2L}$) to the thermal fluctuation energy ($k_B T$). A thermal parameter $\Gamma < 1$ is desired for optimal SQUID operation, otherwise the thermal fluctuations will destabilize the quantum interference effects. In the washboard model, strong thermal fluctuations will shake the washboard causing the ball to continuously roll down the washboard (see chapter 1). The greatest voltage output in both SQUIDs and BiSQUIDs occurred from cells with the smallest critical currents, corroborating the importance of minimizing the modulation parameter $\beta_L = \frac{I_C L^{SQUID}}{\Phi_0}$. Hence a trade-off is observed between small I_C to maximize SQUID voltage ($\beta_L \leq 1$) and I_C large enough to stabilize relative to thermal fluctuations.

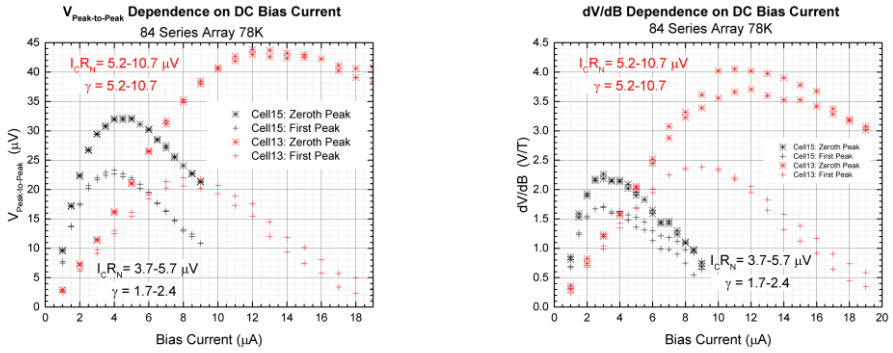

Figure 74: DC SQUID Chip "SQgamma" with $I_C \approx 2\,\mu A$: (left) Peak-to-peak voltage response of 84 series DC SQUIDs as a function of bias current. (right) Maximum slope dV/dB of the SQUID field to voltage characteristic as a function of bias current.

Conclusion

In this chapter two different SQUID array architectures are directly compared: BiSQUIDs and standard 2 junction SQUIDs. BiSQUIDs are a type of shunted SQUID, where a 3rd junction shunts a 2-junction SQUID loop. Shunted

SQUIDs have been previously investigated using a resistive shunt rather than a Josephson junction [85], [86]. A resistive shunt across the SQUID loop can increase the voltage modulation and decrease the flux noise [3]. A BiSQUID with very small 3rd junction critical current effectively becomes a resistively shunted SQUID, and in the limit of very large 3rd junction I_C the BiSQUID becomes a standard 2-junction DC SQUID. BiSQUIDs are inherently at least as sensitive or more sensitive to magnetic fields compared to equivalent DC SQUIDs. BiSQUIDs may be an effective path forward for high field sensitivity SQUIDs, where increased BiSQUID sensitivity is possible without degradation of the current modulation i.e. increased loop area normally decreases SQUID modulation (increased SQUID inductance). In short, for applications where high field sensitivity SQUID devices are highly desirable, BiSQUID architectures may offer an extended parameter space to design SQUID sensors with a large voltage output but control of the bisquid parameters is very important.

The IV characteristics of both BiSQUID and SQUID devices were used to characterize the critical current spread and magnetic modulation parameters. All devices generally exhibited RSJ model-like behavior, with additional curvature in the vicinity of I_C related to critical current parameter spread within the array. Critical current spread was inspected through the fine structure in the vicinity of I_C of the IV characteristic's derivative. The critical current as a function of magnetic field "$I_C(B)$" is fundamentally different in BiSQUIDs compared to standard SQUIDs. A highly regular, sinusoidal current oscillation was observed in standard SQUIDs, whereas BiSQUID devices tend to have sharpened current oscillations containing at least two oscillation frequencies corresponding to the effective area of each BiSQUID loop. The

current modulation depth per flux quantum as a function of bias current "IVmod curve" can be used to determine the magnetic modulation parameter $\beta_L = \frac{I_C^{SQ}{}_L}{\Phi_0}$ using the framework of Tesche and Clarke [20]. Magnetic modulation parameter $\beta_L \leq 1$ describes a standard SQUID device with greater than 50% modulation of the SQUID critical current per flux quantum. Here we demonstrated that both BiSQUIDs and standard SQUID circuits output the greatest voltage modulation when I_C was smallest. Since the inductance was the same for all designs, smaller critical currents correspond to small β_L, confirming $\beta_L \ll 1$ is the correct design limit for large voltage BiSQUIDs.

The BiSQUID Voltage-Field characteristic (VB) is similar to standard SQUIDs for BiSQUIDs with a large 3rd junction I_C compared to junctions 1 and 2. DC SQUIDs and BiSQUIDs with large 3rd junction critical currents behave with highly regular, cosinusoidal????, and single oscillation frequency VB characteristics. The sharpening of the BiSQUID $I_C(B)$ characteristics are not directly mapped onto the VB characteristics. Two different VB oscillation frequencies are observed in BiSQUIDs designed with equal currents in all junctions. Both frequencies closely match to the effective areas of both BiSQUID loops. The BiSQUID voltage response to applied magnetic fields appears to be a highly sensitive function of the 3rd junction I_C and modulation parameter β_L. Since we cannot directly interrogate the properties of the 3rd junction, it is difficult to determine the precise circuit parameters for simulations. Nonetheless critical current parameter sensitivity is observed through both substantial differences in BiSQUID peak-to-peak voltage and the optimal bias current to I_C^{SQUID} ratio.

The performance of BiSQagnes and BiSQalpha strongly suggest a high sensitivity of the BiSQUID VB curvature to the critical current design parameters. None of the BiSQUID devices studied performed with greater linearity than a standard SQUID. We interpret the lack of BiSQUID linearization amongst the 7 BiSQUID Cells in this work as evidence for the need of a narrow working range of acceptable circuit parameters for linearization. In the context of an average 15% critical current spread in circuits containing ion damage junctions [33], the BiSQUID design goal of a 10-20% difference (for low inductance BiSQUIDs) in critical current of the 3rd junction compared to junctions 1 and 2 to achieve linearization is challenging [79]. Linear BiSQUID circuits containing a parameter spread comparable to the design specifications are probably only possible in circuits with a smaller number of series devices. Due to the apparent sensitivity of the BiSQUID performance to the 3rd junction parameters, one path forward to create linear BiSQUIDs is to trim the bridge width of the 3rd junction using a focused ion beam circuit edit technique [86]. Future work on BiSQUIDs constructed from ion damage junctions should be performed in parallel with junction parameter spread studies. Above all, the BiSQUID parameter space is currently not well-understood and many more designs must be tested to determine the optimal range of design parameters.

6. Conclusions and Outlook

Future Work

The standard technique used to fabricate ion damage Josephson junctions is to construct high-aspect ratio, nanoscale "canyons" in micron thick photoresist. Ion masked fabrication is the best option for patterning very large numbers of identical Josephson junctions. The ability to fabricate massively-scalable, large voltage Josephson junctions in YBCO using focused ion beam techniques should enable the development of circuits with many dissimilar Josephson junctions. Large scale SQUID arrays for low noise magnetometers are well suited to ion masked junctions, whereas rapid prototyping of complex circuits such as Josephson digital are better suited to focused ion beam junctions. Both styles of ion damage Josephson junctions may be advanced by improving the junction $I_C R_N$ uniformity and incorporating more accurate device models in future circuit designs.

Next Generation SQUID Array Design

The magnetic field sensitivity of our SQUID designs is currently too low for biomagnetic magnetometer applications. A clinical biomagnetic instrument must be able to detect approximately picoTesla level fields with a high signal to noise ratio in a bandwidth of at least 10 Hz [9]. For applications where an external detection coil must be coupled to the SQUID detector, SQUID arrays are normally less sensitive than single washer SQUIDs due to the need for a network of spatially distributed input coils [87]. Thus there is a need

to develop at least two types of high sensitivity SQUID devices: SQUIDs integrated with external detection coils and direct field coupled SQUIDs. Our current technology is limited to a single layer of YBCO, therefore flux focusing structures and direct inject architectures are the best paths forward to enhance SQUID field sensitivity. For instance, ion damage junctions are easily integrated into existing designs of direct inject magnetometers and gradiometers integrated with slotted washers [88][89]. Direct inject SQUID arrays have not been investigated in a washer geometry, and it is not clear if a direct inject SQUID array will outperform a single direct inject SQUID [83].

Flux focusing structures are another path forward to increase SQUID array sensitivity. We have demonstrated that attaching closed loop structures (such as in the BiSQUID architecture) with narrow wires can both increase the flux focusing into the SQUID hole and increase the threshold magnetic field for magnetic flux trapping. Movement of trapped flux will increase SQUID noise, hence low noise performance is only possible in circuits with minimized numbers of trapped vortices. Flux focusing structures are typically large due to the minimum feature size used in the photolithographic patterning of the wires. However, if the feature size can be significantly decreased, then flux focusing structures can be tightly packed thereby increasing the focusing by minimizing "dead space". One path forward is to use high dose ion irradiation to pattern flux focusing elements with nanoscale features. Nanoscale features can be patterned with focused ion beams such that the ion dose drives the irradiated materials through the superconductor-insulator transition. We have shown that mutual inductance effects are not as large as previously thought, therefore

next generation SQUID arrays should be designed to fill the substrate area in a closepacked geometry incorporating flux focusing structures.

Further improvements in field sensitivity can be gained by increasing the SQUID loop area, if the kinetic inductance of the film can be proportionately decreased to maintain a constant SQUID inductance. Larger SQUID loops generally increase the SQUID inductance requiring a proportionate decrease in SQUID critical current to maintain the SQUID modulation depth i.e. fixed modulation parameter $\beta_L = \frac{LI_C}{\Phi_0}$. SQUID performance is severely degraded when the SQUID critical current is on the order or less than thermal fluctuations. Essentially the SQUID critical current must be not only greater than the thermal fluctuations in the junctions, but also the environmental noise coupled into the SQUID which is necessarily application specific. Thicker films will decrease the kinetic inductance enabling higher critical current designs, however the ion energy must increase significantly in thicker films to maintain junction uniformity. If the ion energy cannot be increased, for instance in focused ion beam sources the energy is often limited to 30 keV, then one solution is to develop a specialized etching process to selectively thin the thick YBCO film in just the junction regions. The DC Argon ion milling process developed in this thesis to pattern the YBCO electrodes severely degrades T_C in the thinned regions (results not shown), presumably due to a combination of heating and Argon implantation. A lower acceleration voltage RF Argon ion milling process will most likely increase the control of both heating and damage effects [90]. Thus future circuit designs should be made out of films thicker than the magnetic penetration depth

(~200 nm) so as to improve the sensitivity, but with thinned materials in the junction regions for maximum junction uniformity and performance.

BiSQUID Design

There is continued interest in developing SQUID architectures with increased linearity of the magnetic field to voltage transfer function. BiSQUIDs have been proposed as one path forward to create linearized SQUID transfer functions, however the architecture appears to be very sensitive to circuit parameters. At this time it is unclear as to whether a BiSQUID can be constructed with both enhanced linearity and large voltage modulation using any current state-of-the-art YBCO technologies. It is clear that future investigations of BiSQUIDs constructed from ion damage junctions should be performed in parallel with junction parameter spread studies. The biggest obstacle encountered in the adaptation of BiSQUID designs to ion damage junctions in YBCO is the lack of both junction device models and BiSQUID circuit simulations of sufficient predictive power. The systematic characterization of the BiSQUID parameter space was ultimately unsuccessful in this work. The BiSQUID design process used the numerical results from [79] as a design guide, and the ratio of the critical currents were used to estimate the required ion dose for fabrication with focused Helium ion beam. Future studies of ion damage BiSQUIDs should incorporate quantitative models to clearly define the parameter space region in which maximum linearity enhancement should occur.

Junction Simulations

We formulated the ion damage junction simulation model in Chapter 2 for a specific purpose: to calculate the required ion dose for a homogeneously damaged junction given a constraint of ion species, ion energy, junction length, and most importantly junction T_c. Junction simulation tools will enable efficient development of circuits like the BiSQUID, which were previously designed by extrapolating ion dose parameters from existing junctions without consideration of junction length. The simulation model presented in this work can also be used to generate complex ion implantation protocols, such as multi-energy implants for increased barrier homogeneity [91] and circuit optimization using focused ion beam circuit edit techniques [92]. The ultimate goal is to develop a microscopic model of the electrical properties of ion damage Josephson junctions. There are several aspects of ion damage Josephson junctions that must be understood before such a model can be further constructed including: the properties of the irradiated barrier during the superconductor-insulator transition, the effect of the unconventional order parameter for arbitrary barrier alignment to the crystal lattice, and length scales of the proximity effect as a function of ion damage. Above all, it is now well understood that the highest voltage and most uniform ion damage Josephson junctions should be made with the shortest barrier lengths and in films much thinner than the ion range.

The ability to create an accurate junction layout for a specific device parameters is key to investigate complex circuits such as digital logic gates. The design space available using ion masked fabrication was too narrow to construct complex circuits. For instance ion damage junctions fabricated with

ion masking techniques were limited to a single irradiation dose for all junctions and a single junction patterning step to avoid junction degradation. Junctions fabricated with ion masks were also limited to barrier lengths greater than ~20nm and were prone to significant variation in the junction length. The difficulty in constructing ion masked junctions makes the technology prone to elevated parameter spread and low yields. With new patterning technologies such as focused helium ion beam junctions, there is sufficient control of the barrier length to control the junction parameters. The advent of focused Helium ion beam Josephson junctions (pioneered by E. Cho and S. A. Cybart [19][47]) opened the door to new capabilities such as multiple ion doses, energies, species, and junction lengths in a single circuit. Using these new fabrication capabilities, it is now possible to rapidly prototype circuits with a much higher degree of complexity. However, the full potential of ion damage Josephson junctions will not be realized until an optimization method incorporating all these fabrication capabilities is available to the designer that can generate a device layout to match circuit specifications. Above all the ion damage Josephson junction is a versatile, easy to fabricate, and mature junction technology well-suited for complex materials systems such as YBCO.

Final Conclusions

In this work we have investigated Superconducting Quantum Interference Devices (SQUID) in arrayed architectures using ion damage Josephson junctions constructed from $YBa_2Cu_3O_7$ thin films. All SQUIDs designs within the arrays were identical to avoid Superconducting Quantum Interference Filter (SQIF) effects. We demonstrated that mutual coupling

effects in tightly packed series-parallel SQUID arrays are much smaller than previously thought. No significant performance degradation was observed for "closepacked" arrays compared to mutually decoupled arrays for a wide range of circuit parameters in devices containing greater than 1000 SQUIDs. Amazingly, we observed a transition in parallel SQUIDs from multislit interference to multislit diffraction behavior as the bias current is increased to the optimal SQUID working point. We attribute the decoherence between parallel SQUIDs at elevated current bias to a redistribution of current such that a unique solution to the flux quantization condition around the parallel segment is lost. Coherent multislit interference in parallel SQUID arrays is only possible with magnetically short Josephson junctions i.e. uniform current density in the junction region. The voltage field characteristics of parallel SQUID arrays were favorably sharpened compared to series arrays. Thus series-parallel SQUID arrays significantly increase the voltage-magnetic field transfer function compared to single SQUIDs.

We have demonstrated that SQUIDs constructed from ion damage Josephson junctions are massively scalable, with a device density higher than what has been and probably is possible with current other-junction technologies: 4.2 million junctions or greater than 10^5 SQUIDs per cm^2 in our largest devices. We demonstrated that the highest voltage and most uniform SQUID devices are constructed from ion damage Josephson junctions with the shortest junction length and in films thinner than the ion range. These devices also operate over a wide temperature range (>10 K), which is unique to high temperature SQUIDs. Ion damage SQUIDs can be "tuned" using three commensurate parameters: ion dose, operating temperature, and applied

magnetic field (Fraunhofer bias). Previously unobtainable noise scaling in compact devices is possible using a high density SQUID array, with direct applications in broadband RF sensors and nanotesla sensitive magnetometers.

We compared series arrays of 3 junction BiSQUIDs to standard 2 junction SQUIDs using novel focused Helium ion beam Josephson junctions. We found that the voltage-field characteristics of BiSQUIDs are quite similar to standard 2 junction SQUIDs. Junction critical current parameter spread degraded BiSQUID performance more than standard SQUIDs. The BiSQUID field sensitivity is enhanced via flux focusing compared to standard SQUIDs. BiSQUID performance is a highly sensitive function of the 3rd junction critical current and the modulation parameter $\beta_L = \frac{LI_C}{\Phi_0}$. More work is needed to explore the BiSQUID parameter space which contains more parameters than standard SQUIDs (3 critical currents, 2 loops), however no linearity enhancement was observed in 3 different BiSQUID designs compared to the standard 2 junction SQUIDs. If linearity enhancement is possible in BiSQUIDs then the design space must be small and detailed circuit simulations are most likely necessary to determine the circuit parameter range to achieve optimal performance.

Overall ion damage Josephson junctions can be used to fabricate high quality, high density SQUID devices in YBCO materials. If the junction parameter spread can be reduced and accurate simulation tools developed, then many doors open to design circuits for a range of applications in the defense, communications, and medical industries.

7. Bibliography

[1] S. M. Sze, *Physics of Semiconductor Devices*. 1981.

[2] S. Polonskyi, V. Semenod, P. Bunyk, A. Kirichenko, Ay. Kidiyarova-Shevchenko, O. Mukhan, P. Shevchenko, D. Schneider, Dy. Zinoviev, and K. Likharev, "NEW RSFQ CIRCUITS," *IEEE Trans. Appl. Supercond.*, vol. 3, 1993.

[3] J. Clarke and A. I. Braginski, *The SQUID Handbook. Vol. 1, Fundamentals and Technology of SQUIDS and SQUID Systems*. 2004.

[4] M. Tinkham, *An Introduction to Superconductivity*, 2nd ed. Dover Publications, 2004.

[5] W. Edwin and B. Gonville, "Thesis: Josephson Junctions and Devices fabricated by Focused Electron Beam Irradiation," 1997.

[6] M. K. Wu, J. R. Ashburn, C. J. Torng, P. H. Hor, R. L. Meng, L. Gao, Z. J. Huang, Y. Q. Wang, and C. W. Chu, "Superconductivity at 93 K in a new mixed-phase Y-Ba-Cu-O compound system at ambient pressure," *Phys. Rev. Lett.*, vol. 58, p. 908, 1987.

[7] B. Utz, R. Semerad, M. Bauer, W. Prusseit, P. Berberich, and H. Kinder, "Deposition of YBCO and NBCO Films on Areas of 9 Inches in Diameter," *IEEE Trans. Appl. Supercond.*, vol. 7, no. 2, 1997.

[8] D. Koelle, R. Kleiner, F. Ludwig, E. Dantsker, and J. Clarke, "High-transition-temperature superconducting quantum interference devices," *Rev. Mod. Phys.*, vol. 71, no. 3, pp. 631–686, 1999.

[9] D. Drung, "High-T c and low-T c dc SQUID electronics," *Supercond. Sci. Technol.*, vol. 16, no. 1603, pp. 1320–1336, 2003.

[10] D. Drung, C. Aßmann, J. Beyer, A. Kirste, M. Peters, F. Ruede, and T. Schurig, "Highly Sensitive and Easy-to-Use SQUID Sensors," *IEEE Trans. Appl. Supercond.*, vol. 17, no. 2, 2007.

[11] W. L. McMillan and M. Rowell, "Lead Phonon Spectrum Calculated from Superconducting Density of States," *Phys Rev Lett*, vol. 14, no. 4, pp. 108–112, 1965.

[12] W. C. Stewart, "Current-voltage characteristics of Josephson junctions," *Appl. Phys. Lett.*, vol. 12, no. 8, pp. 277–280, 1968.

[13] D. E. McCumber, "Effect of ac impedance on dc voltage-current characteristics of superconductor weak-link junctions," *J. Appl. Phys.*, vol. 39, no. 7, pp. 3113–3118, 1968.

[14] S. K. Tolpygo and M. Gurvitch, "Critical currents and Josephson penetration depth in planar thin-film high-T c Josephson junctions," *Appl. Phys. Lett*, vol. 69, no. 25, pp. 3914–3916, 1996.

[15] P. A. Rosenthal, M. R. Beasley, K. Char, M. S. Colclough, and G. Zaharchuk, "Flux focusing effects in planar thin-film grain-boundary Josephson junctions," *Appl. Phys. Lett.*, vol. 59, p. 3482, 1991.

[16] C. S. Owen and D. J. Scalapino, "Vortex Structure and Critical Currents in Josephson Junctions*," *Phys. Rev.*, vol. 164, no. 7, pp. 164–167, 1967.

[17] D. A. Wollman, D. J. Van Harlingen, W. C. Lee, D. M. Ginsberg, and A. J. Leggett, "Experimental determination of the superconducting pairing state in YBCO from the phase coherence of YBCO-Pb dc SQUIDs," *Phys. Rev. Lett.*, vol. 71, no. 13, pp. 2134–2137, 1993.

[18] V. Ambegoakar and B. I. Halperin, "Voltage due to thermal noise in the dc Josephson Effect," *Phys. Rev. Lett.*, vol. 22, no. 25, pp. 1364–1366, 1969.

[19] E. Y. Cho, "Focused Helium Beam Irradiated Josephson Junctions," 2016.

[20] C. D. Tesche and J. Clarke, "dc SQUID: Noise and Optimization*," *J. Low Temp. Phys.*, vol. 294, no. 3, pp. 1–9, 1977.

[21] H. J. M. Ter Brake, F.-I. Buchholz, G. Burnell, T. Claeson, D. Crété, P. Febvre, G. J. Gerritsma, H. Hilgenkamp, R. Humphreys, Z. Ivanov, W. Jutzi, M. I. Khabipov, J. Mannhart, H.-G. Meyer, J. Niemeyer, A. Ravex, H. Rogalla, M. Russo, J. Satchell, M. Siegel, H. Tö Pfer, F. H. Uhlmann, J.-C. Villégier, E. Wikborg, D. Winkler, and A. B. Zorin, "SCENET roadmap for superconductor digital electronics," *Phys. C*, vol. 439, pp. 1–41, 2006.

[22] J. F. Ziegler, *Ion Implantation Science and Technology*. New York: Academic, 1988.

[23] A. E. White, K. T. Short, D. C. Jacobson, J. M. Poate, R. C. Dynes, P. M. Mankiewich, W. J. Skocpol, R. E. Howard, M. Anzlowar, K. W. Baldwin, A. F. J. Levi, J. R. Kwo, T. Hsieh, and M. Hong, "Ion-beam-induced destruction of superconducting phase coherence in YBaCuO," *Phys. Rev. B*, vol. 8, no. 7, p. 3755, 1988.

[24] V. V Kirsanov, N. N. Musin, and H. J. Shamarina, "Displacement threshold energy in high-temperature superconductors. II. Thresholds for O, Ba and Y in YBa2Cu307," *Phys. Lett. A*, vol. 171, pp. 223–233, 1992.

[25] A. Legris, F. Rullier-Albenque, E. Radeva, and P. Lejay, "Effects of electron irradiation on YBCO superconductor," *J. Phys. I Fr.*, vol. 3, no. 7, pp. 1605–1615, 1993.

[26] S. K. Tolpygo, J.-Y. Lin, M. Gurvitch, S. Y. Hou, and J. M. Phillips, "Effect of

oxygen defects on transport properties and Tc of YBCO-displacement energy for plane and chain oxygen and implications for irradiation induced resistivity and Tc suppression," *Phys. Rev. B*, vol. 53, p. 12362, 1996.

[27] B. H. Moeckly, D. K. Lathrop, and R. A. Buhrman, "Electromigration study of oxygen disorder and grain-boundary effects in YBa2Cu3Q7 s thin films," *Phys. Rev. B*, vol. 47, no. 1, 1993.

[28] A. E. White, K. T. Short, R. C. Dynes, A. F. J. Levi, M. Anzlowar, K. W. Baldwin, P. A. Polakos, T. A. Fulton, and L. N. Dunkleberger, "Controllable reduction of critical currents in YBa2Cu3O7−δ films," *Appl. Phys. Lett.*, vol. 53, no. 172, pp. 1010–203, 1988.

[29] R. C. Dynes, A. E. White, J. M. Graybeal, and J. P. Garno, "Breakdown of Eliashberg Theory for Two-Dimensional Superconductivity in the Presence of Disorder," *Phys Rev Lett*, vol. 57, no. 17, p. 2195, 1986.

[30] A. E. White, R. C. Dynes, and J. P. Garno, "Destruction of superconductivity in quench-condensed two-dimensional films," *Rapid Commun.*, vol. 33, no. 1, 1986.

[31] A. E. White, K. T. Short, R. C. Dynes, A. F. J. Levi, M. Anzlowar, K. W. Baldwin, P. A. Polakos, T. A. Fulton, and L. N. Dunkleberger, "Controllable reduction of critical currents in YBa2Cu3O7−δ films," *Appl. Phys. Lett.*, 1988.

[32] S. A. Cybart, P. X. T. Yen, E. Y. Cho, J. U. Huh, V. N. Glyantsev, C. S. Yung, B. Moeckly, J. W. Beeman, and R. C. Dynes, "Comparison of Y–Ba–Cu–O Films Irradiated With Helium and Neon Ions for the Fabrication of Josephson Devices," *IEEE Trans. Appl. Supercond.*, vol. 24, no. 4, 2014.

[33] S. A. Cybart, S. M. Anton, S. M. Wu, J. Clarke, and R. C. Dynes, "Very Large Scale Integration of Nanopatterned YBa 2 Cu 3 O 7-δ Josephson Junctions in a Two-Dimensional Array," *Nano Lett.*, vol. 9, no. 10, pp. 3581–3585, 2009.

[34] W. Lang, H. Richter, M. Marksteiner, K. Siraj, M. A. Bodea, J. D. Pedarnig, C. Grigoropoulos, D. Bäuerle, C. Hasenfuss, L. Palmetshofer, R. Kolarova, and P. Bauer, "Masked ion beam irradiation of high-temperature superconductors: patterning of nano-size regions with high point-defect density," *Int. J. Nanotechnol*, vol. 68, no. 7, 2009.

[35] R. S. Averback and T. Diaz de la Rubia, *Displacement damage in irradiated metals and semiconductors*. 1998.

[36] G. P. Summers, E. A. Burke, D. B. Chrisey, M. Nastasi, and J. R. Tesmer, "Effect of particle-induced displacements on the critical temperature of YBa2Cu3O7," *Appl. Phys. Lett.*, vol. 55, no. 14, pp. 1469–1471, 1989.

[37] S. S. Tinchev, "Modeling of YBa2Cu3O7 weak links produced by oxygenion modification," *J. Appl. Phys*, vol. 78, no. 53, pp. 1095–1155, 1995.

[38] B. D. Weaver, E. M. Jackson, G. P. Summers, and E. A. Burke, "Atomic disorder and the transition temperature of cuprate superconductors," *Phys. Rev. B*, vol. 46, no. 2, pp. 1134–1137, 1992.

[39] K. A. Delin and A. W. Kleinsasser, "Stationary properties of high-critical-temperature proximity effect Josephson junctions," *Supercond. Sci. Technol.*, vol. 9, pp. 227–269, 1996.

[40] L. Antognazza, B. H. Moeckly, and K. Char, "Properties of high-Tc Josephson junctions with YCaBCO barrier layers," *Phys. Rev. B*, vol. 52, no. 6, pp. 4559–4567, 1995.

[41] K. A. Kouznetsov, A. G. Sun, B. Chen, A. S. Katz, S. R. Bahcall, J. Clarke, R. C. Dynes, D. A. Gajewski, S. H. Han, M. B. Maple, J. Giapintzakis, J.-T. Kim, and D. M. Ginsberg, "c-axis Josephson Tunneling between YBa 2 Cu 3 O 72d and Pb: Direct Evidence for Mixed Order Parameter Symmetry in a High-T c Superconductor," *Phys Rev Lett*, vol. 79, no. 16, p. 3050, 1997.

[42] K. Chen, S. A. Cybart, and R. C. Dynes, "Study of closely spaced YBCO Josephson junction pairs," *IEEE Trans. Appl. Supercond.*, vol. 15, pp. 149–152, 2005.

[43] A. S. Katz, "Fabrication, Characterization, and Analysis of Nanofabricated Ion Damage High Temperature Josephson Junctions," 1998.

[44] M. A. Kirk and Y. Yan, "Structure and properties of irradiation defects in YBa2Cu3O(7-x)," *Micron*, vol. 30, no. 5, pp. 507–526, 1999.

[45] M. D. Rintoul and S. Torquato, "Precise determination of the critical threshold and exponents in a three-dimensional continuum percolation model," *J. Phys. A Math. Gen.*, vol. 30, p. L585, 1997.

[46] A. S. Katz, S. I. Woods, and R. C. Dynes, "Transport properties of high-T/sub c/ planar Josephson junctions fabricated by nanolithography and ion implantation," *J. Appl. Phys.*, vol. 87, no. 6, p. 2978, 2000.

[47] S. A. Cybart, E. Y. Cho, T. J. Wong, B. H. Wehlin, M. K. Ma, C. Huynh, and R. C. Dynes, "Nano Josephson superconducting tunnel junctions in YBa2Cu3O7-δ directly patterned with a focused helium ion beam," *Nat. Nano*, vol. 10, no. 7, pp. 598–602, 2015.

[48] P. O. De Gennes, "Boundary EfFects in Superconductors," *Rev. Mod. Phys.*, vol. 129, no. 647, 1963.

[49] E. Blonder, M. Tinkham, and T. M. Klapwijk, "Transition from metallic to

tunneling regimes in superconducting microconstrictions: Excess current, charge imbalance, and supercurrent conversion," *Phys. Rev. B*, vol. 25, no. 7, pp. 4515–4532, 1982.

[50] K. A. Delin and A. W. Kleinsasser, "Stationary properties of high-critical-temperature proximity effect Josephson junctions," *Supercond. Sci. Technol.*, vol. 9, pp. 227–269, 1996.

[51] V. Matijasevic, P. Rosenthal, K. Shinohara, A. F. Marshall, R. H. Hammond, and M. R. Beasley, "Reactive coevaporation of YBaCuO superconducting films," *J. Mater. Res.*, vol. 6, no. 4, pp. 682–698, 1991.

[52] R. G. Humphreys and J. A. Edwards, "Thin film grain boundary junctions in a perpendicular magnetic field," *Phys. C*, vol. 210, pp. 42–54, 1993.

[53] K. Chen, S. A. Cybart, and R. C. Dynes, "Planar thin film YBa 2 Cu 3 O 7 Josephson junction pairs and arrays via nanolithography and ion damage," *Appl. Phys. Lett.*, vol. 85, p. 2863, 2004.

[54] J. W. Ekin, T. M. Larson, N. F. Bergren, A. J. Nelson, A. B. Swartzlander, L. L. Kazmerski, A. J. Panson, and B. A. Blankenship, "High Tc superconductor/noble-metal contacts with surface resistivities in the 10−10 Ω cm2 range," *Appl. Phys. Lett.*, 1988.

[55] M. Gurvitch, J. M. Valles, A. M. Cucolo, R. C. Dynes, J. P. Garno, L. F. Schneemeyer, and J. V Waszczak, "Reproducible Tunneling Data on Chemically Etched Single Crystals of YBa2Cu307," vol. 63, no. 9, 1989.

[56] S. A. Cybart, "Planar Josephson junctions and arrays by electron beam lithography and ion damage," 2005.

[57] V. K. Kornev, A. V Sharafiev, I. I. Soloviev, N. V Kolotinskiy, V. A. Scripka, and O. A. Mukhanov, "Superconducting Quantum Arrays," *IEEE Trans. Appl. Supercond.*, vol. 24, no. 4, 2014.

[58] S. Berggren, G. Prokopenko, P. Longhini, A. Palacios, O. A. Mukhanov, A. L. De Escobar, B. J. Taylor, M. C. De Andrade, M. Nisenoff, L. Fellow, R. L. Fagaly, T. Wong, E. Cho, E. Wong, and V. In, "Development of 2-D Bi-SQUID Arrays With High Linearity," vol. 23, no. 3, pp. 1400208–1400215, 2013.

[59] M. E. Huber, P. A. Neil, R. G. Benson, D. A. Burns, A. M. Corey, C. S. Flynn, Y. Kitaygorodskaya, O. Massihzadeh, and J. M. Martinis, "DC SQUID Series Array Amplifiers with 120 MHz Bandwidth," *IEEE Trans. Appl. Supercond.*, vol. 11, no. 1, pp. 1251–1256, 2001.

[60] D. Drung, C. Hinnrichs, and H.-J. Barthelmess, "Low-noise ultra-high-speed dc SQUID readout electronics," *Supercond. Sci. Technol.*, vol. 19, pp. S235–S241, 2006.

[61] J. Oppenländer, C. Häussler, and N. Schopohl, "Non-Phi0-periodic macroscopic quantum interference in one-dimensional parallel Josephson junction arrays with unconventional grating structure," *Phys. Rev. B*, vol. 63, no. 2, p. 024511, 2000.

[62] B. Chesca, D. John, and C. J. Mellor, "Flux-coherent series SQUID array magnetometers operating above 77 K with superior white flux noise than single-SQUIDs at 4.2 K," *Appl. Phys. Lett*, vol. 107, no. 71, p. 162602, 2015.

[63] J. Zimmerman and a. Silver, "Macroscopic Quantum Interference Effects through Superconducting Point Contacts," *Phys. Rev.*, vol. 141, no. 1964, pp. 367–375, 1966.

[64] A. T. A. M. de Waele, W. H. Kraan, and R. de B. Ouboter, "A Superconducting Interference Grating," *Physica*, vol. 40, pp. 302–308, 1968.

[65] W. T. Tsang and T. Van Duzer, "Dc analysis of parallel arrays of two and three Josephson junctions," *J. Appl. Phys.*, vol. 46, no. 10, pp. 4573–4580, 1975.

[66] R. L. Peterson and C. A. Hamilton, "Analysis of threshold curves for superconducting interferometers," *J. Appl. Phys.*, vol. 50, no. 12, pp. 8135–8142, 1979.

[67] J. Pearl, "Current distribution in superconducting films carrying quantized fluxoids," *Appl. Phys. Lett.*, vol. 5, no. 4, pp. 65–66, 1964.

[68] J. B. Majer, J. R. Butcher, and J. E. Mooij, "Simple phase bias for superconducting circuits Simple phase bias for superconducting circuits," *Appl. Phys. Lett*, vol. 80, p. 3638, 2002.

[69] V. K. Kornev, I. I. Soloviev, N. V Klenov, and O. A. Mukhanov, "High Linearity SQIF-Like Josephson-Junction Structures," *IEEE Trans. Appl. Supercond.*, vol. 19, no. 3, 2009.

[70] D. E. McCumber and B. I. Halperin, "Time scale of intrinsic resistive fluctuations in thin superconducting wires," *Phys. Rev. B*, vol. 1, no. 3, pp. 1054–1070, 1970.

[71] F. Sharifi, A. V. Herzog, and R. C. Dynes, "Crossover from two to one dimension in in situ grown wires of Pb," *Phys. Rev. Lett.*, vol. 71, p. 428, 1993.

[72] G. Stan, S. B. Field, and J. M. Martinis, "Critical Field for Complete Vortex Expulsion from Narrow Superconducting Strips," *Phys Rev Lett*, vol. 92, no. 9, p. 097003, 2004.

[73] T. A. Fulton, R. C. Dynes, and P. W. Anderson, "The Flux Shuttle-A

Josephson Junction Shift Register Employing Single Flux Quanta," *Proc. IEEE*, vol. 61, no. 1, 1973.

[74] E. H. Brandt and J. R. Clem, "Superconducting thin rings with finite penetration depth," *Phys. Rev*, vol. 69, p. 184509, 2004.

[75] S. A. Cybart, T. N. Dalichoauch, S. M. Wu, S. M. Anton, J. A. Drisko, J. M. Parker, B. D. Harteneck, and Dynes, "Comparision of measurements and simulations of series-parallel incommensurate area superconucting quantum interference device arrays fabricated from YBCO ion damage josephson junctions," *Appl. Phys. Lett*, vol. 112, p. 063911, 2012.

[76] S. K. Tolpygo and M. Gurvitch, "Critical Currents , Proximity Effect , and Josephson Penetration Depth in Planar HTS Josephson Junctions," *IEEE Trans Magn*, vol. 7, no. 2, pp. 3208–3212, 1997.

[77] S. A. Cybart, S. M. Wu, S. M. Anton, I. Siddiqi, J. Clarke, and R. C. Dynes, "Series array of incommensurate superconducting quantum interference devices from YBCO ion damage Josephson junctions," *Appl. Phys. Lett.*, vol. 93, no. 18, p. 182502, 2008.

[78] D. Koelle, A. H. Miklich, E. Dantsker, F. Ludwig, D. T. Nemeth, J. Clarke, W. Ruby, and K. Char, "High performance dc SQUID magnetometers with single layer YBa2Cu3O7−x flux transformers," *Appl. Phys. Lett.*, vol. 63, p. 3630, 1993.

[79] V. K. Kornev, I. I. Soloviev, N. V Klenov, and O. a Mukhanov, "Bi-SQUID: a novel linearization method for dc SQUID voltage response," *Supercond. Sci. Technol.*, vol. 22, no. 11, pp. 1–6, 2009.

[80] V. Kornev, I. Soloviev, N. Klenov, and O. Mukhanov, "Progress in high-linearity multi-element Josephson structures," *Phys. C*, vol. 470, pp. 886–889, 2010.

[81] *Purchased from Theva Dunnschichttechnik GmbH, Rote-Kreuz-Str. 8, D-85737 Ismaning, Germany.* .

[82] P. W. Anderson and A. H. Dayem, "Radio-frequency effect in superconducting thin film bridges," *Phys. Rev. Lett.*, vol. 13, p. 195, 1964.

[83] E. Y. Cho, M. K. Ma, C. Huynh, K. Pratt, D. N. Paulson, V. N. Glyantsev, R. C. Dynes, and S. A. Cybart, "YBCO SQUID with metallic to insulating barriers written with a focused helium ion beam," *Appl. Phys. Lett*, vol. 106, p. 252601, 2015.

[84] S. A. Cybart, E. Y. Cho, T. J. Wong, V. N. Glyantsev, J. U. Huh, C. S. Yung, B. H. Moeckly, J. W. Beeman, E. Ulin-Avila, S. M. Wu, and R. C. Dynes, "Large voltage modulation in magnetic field sensors from two-dimensional arrays of YBCO nano Josephson Junctions," *Appl. Phys. Lett.*, vol. 104, no. 6, p. 062601, 2014.

[85] K. Enpuku, K. Sueoka, K. Yoshida, and F. Irie, "Effect of damping resistance on voltage versus flux relation of a dc SQUID with large inductance and critical current," *J. Appl. Phys.*, vol. 57, p. 334439, 1985.

[86] D. J. Kang, W. E. Booij, M. G. Blamire, and E. J. Tarte, "Performance of high-T c superconducting quantum interference devices with resistively shunted inductances," *Appl. Phys. Lett.*, vol. 73, p. 3929, 1998.

[87] J. Beyer and D. Drung, "A SQUID series array dc current sensor," *Supercond. Sci. Technol.*, vol. 21, p. 095012, 2008.

[88] E. Dantsker, S. Tanaka, and J. Clarke, "High-T[sub c] super conducting quantum interference devices with slots or holes: Low 1/f noise in ambient magnetic fields," *Appl. Phys. Lett.*, vol. 70, no. 15, p. 2037, Apr. 1997.

[89] S. Lee, W. R. Myers, H. L. Grossman, H.-M. Cho, Y. R. Chemla, and J. Clarke, "Magnetic gradiometer based on a high-transition temperature superconducting quantum interference device for improved sensitivity of a biosensor," *Appl. Phys. Lett*, vol. 81, p. 3094, 2002.

[90] B. H. Moeckly and K. Char, "Properties of interface-engineered high T c Josephson junctions," *Appl. Phys. Lett.*, vol. 71, p. 2526, 1997.

[91] J. D. Plummer, M. Deal, and P. D. Griffin, *Silicon VLSI Technology: Fundamentals, Practice, and Modeling*. 2000.

[92] M. J. Martínez-Pérez, J. Sesé, R. Córdoba, F. Luis, D. Drung, and T. Schurig, "Circuit edit of superconducting microcircuits," *Supercond. Sci. Technol.*, vol. 22, p. 125020, 2009.